Numerical simulations of turbulence and magnetic instabilities in liquid metal experiments

Dissertation

zur Erlangung des Doktorgrades Dr. rer. nat.

der Fakultät für Naturwissenschaften

der Universität Ulm

vorgelegt von

ANGELO LIMONE

aus CASERTA (ITALIEN)

2013

Dekan:	Prof. Dr. Joachim Ankerhold
Erstgutachter:	apl. Prof. Dr. Frank Jenko
Zweitgutachter:	Prof. Dr. Peter Reineker
Tag der Promotion: 24. Okt 2013	

Summary

Astrophysical observations show that planets, stars, galaxies, and galaxy clusters have magnetic fields of various strength and spatial scales. Yet the origin of those magnetic fields and how they affect the development of forming structures such as protostars, protoplanetary disks, and protogalaxies is still not clear. Indeed, magnetic fields tend to decay because of magnetic diffusion, but the observations show that many magnetic field structures are much older than the typical diffusion time scale of the host astrophysical object. Therefore another mechanism must take place in order to avoid the decay of the magnetic field. In geo- and astrophysical environments the "dynamo" instability is often invoked in order to explain the creation (or the stability) of the observed large-scale cosmic magnetic fields, and in this case the effect is known as *geophysical* or *astrophysical dynamo mechanism*. This mechanism consists in the transformation of the kinetic energy of a fluid into magnetic energy. When the geometry of the system obeys some particular constraints, this mechanism can lead to a runaway effect, where the magnetic field is unstable until some saturation mechanism takes over. The origin of astrophysical magnetic fields is not the only unanswered question in this field of research: The interaction of preexistent magnetic fields with forming structures is still object of investigation. Indeed, under certain circumstances, the sole presence of a magnetic field (regardless of its strength) can strongly affect the behavior of particular astrophysical structures (i.e., rotating disks of conducting fluid), by making those systems dynamically unstable to the so-called *magnetorotational instability*.

In order to understand and isolate these two instabilities, laboratory experiments using liquid metals as working fluid have been designed and realized during the last decades. This task has turned out to be difficult since an unexpected behavior of the experiments occurred. In laboratory dynamos, for instance, the presence of turbulence can hinder the process, whereas in laboratory experiments aiming to study the magnetorotational instability, other concurrent and unforeseen instabilities can make the detection of this effect very difficult.

In this dissertation, a numerical approach is taken in order to address these problems in flows that are important for laboratory, and hence astrophysical, purposes. The equations of incompressible magnetohydrodynamics

are solved numerically by using mainly two codes, each one with different features. The core of the thesis resides in the post-processing analysis of the simulated data, where a powerful statistical analysis has been used in order to extract information which would be difficult to characterize with conventional spectral methods.

Contents

1 Introduction **7**
- 1.1 The interplay between magnetic fields and flows in astrophysical objects . . . 7
- 1.2 Liquid metal experiments . . . 10
- 1.3 Contents of this dissertation . . . 12

2 Theoretical fundamentals **13**
- 2.1 Governing equations: Hydrodynamics . . . 14
  - 2.1.1 Lagrangian and Eulerian frames of reference in fluid dynamics . . . 14
  - 2.1.2 The continuity equation . . . 15
  - 2.1.3 The momentum equation . . . 16
- 2.2 The induction equation . . . 19
- 2.3 Putting all together: the system of governing equations . . . 20
- 2.4 Waves, instabilities, and turbulence . . . 21
  - 2.4.1 Magnetorotational Instability . . . 21
  - 2.4.2 The weak spring picture . . . 22
  - 2.4.3 Dynamo theory . . . 25
  - 2.4.4 Kolmogorov's theory of small scale turbulence . . . 31

3 Experiments **37**
- 3.1 The Princeton Magnetorotational Instability experiment . . . 37
  - 3.1.1 Hydrodynamics of the experiment . . . 38
  - 3.1.2 The effect of the superimposed magnetic field . . . 42
- 3.2 The Madison Dynamo Experiment . . . 46
  - 3.2.1 First comparisons between simulations and experiments 48
- 3.3 Summary . . . 49

4 Numerical approach **51**
- 4.1 The `SFEMaNS` code . . . 52
  - 4.1.1 Solving the MHD system in heterogeneous domains . 52
  - 4.1.2 Nondimensionalization of the equations . . . 53
  - 4.1.3 Boundary conditions on the magnetic field . . . 54

4.2 The DYNAMO code . . . 56
4.2.1 Formulation of the problem in spherical geometry . . 57
4.2.2 Characteristic velocity and time-scales . . . 59
4.3 Summary . . . 59

5 Modeling the Magnetorotational Instability experiment 61
5.1 SFEMaNS: Geometry and mesh . . . 62
5.2 Benchmark of SFEMaNS and code validation . . . 63
5.3 Axisymmetric runs . . . 65
5.3.1 Inflow *vs* outflow mid-plane jets . . . 70
5.3.2 Scaling of the MRI Amplitude with Re . . . 74
5.4 Conclusions and outlook . . . 77

6 Quantifying turbulence in the dynamo experiment 80
6.1 Intermittency . . . 81
6.2 Quantifying intermittency . . . 82
6.3 Numerical setup . . . 85
6.4 Results . . . 86
6.5 Summary and conclusions . . . 93

7 Facilitating dynamo action via turbulence control 96
7.0.1 Suppression of large-scale eddies in the MDE . . . 97
7.0.2 Suppression of the turbulent resistivity . . . 98
7.1 Role of the baffle in numerical simulations . . . 99
7.1.1 Implementation of the equatorial baffle in the spatial domain . . . 100
7.1.2 Implementation of the equatorial baffle in the spectral domain . . . 103
7.2 Summary and interpretation of the results . . . 109

8 Shedding light on the dynamo mechanism: The role of turbulence 112
8.1 Introduction . . . 112
8.2 SVD analysis . . . 113
8.2.1 Statistical aspects of SVD . . . 115
8.2.2 Further important properties of the SVD analysis and application to the DYNAMO data . . . 117
8.3 SVD analysis of the virtual water experiment . . . 121
8.3.1 First SVD mode . . . 121
8.3.2 Second SVD mode . . . 122
8.3.3 Singular values . . . 125
8.3.4 Temporal evolution . . . 126
8.3.5 Comparison with previous results . . . 130
8.3.6 Role of time-stationary $u_2(\mathbf{r})$ in the dynamo process . 131

8.4 An interpretation of the $Rm_c(Re)$ curve 132
8.5 Strategies for turbulence control for dynamo purposes 133
8.5.1 Role of an equatorial baffle 134
8.5.2 Role of a disc-shaped equatorial baffle between the impellers 135
8.5.3 Results 136
8.6 Interpretation of the results 136
8.7 Summary 137

9 Conclusions **139**
9.1 Interplay between turbulence and the dynamo effect in the MDE 139
9.2 Basic turbulent properties in bounded geometries 141
9.3 Magnetorotational Instability 142

Appendices **144**

A Nondimensionalization of the MHD equations **145**
A.1 Induction equation 145
A.2 Navier-Stokes equation 146

B Miscellaneous mathematical results used throughout this thesis **148**
B.1 Equation of motion of the displacement d$\mathbf{x}$ embedded in the fluid 148
B.2 An important property of the pseudoscalar α 149
B.3 Lagrange multipliers 149
B.4 Singular Value Decomposition theorem 151
B.5 Origin of the Stewartson layer: The Taylor-Proudman Theorem 152

C Tabular overview of the simulated relative exponents **154**

D Time intermittency: Calculated exponents **157**

Bibliography **157**

Acknowledgements **165**

Chapter 1

Introduction

"In astrophysics, the larger is our ignorance, the stronger is the magnetic field."

Lodewijk Woltjer, Nordwijk Symposium, 1966

1.1 The interplay between magnetic fields and flows in astrophysical objects

Magnetic fields permeate the Universe. Observations show that planets, stars and galaxies have magnetic fields of various strength and spatial scales. Consequently, it is not a surprise that scientific research has been trying to understand the origin of those magnetic fields and how they affect the development of forming structures (e.g., protostars, protoplanetary disks, and protogalaxies). The argument that the collapsing matter increases the amplitude of a preexistent magnetic field (because of an effect known as "conservation of the magnetic flux in ideal conditions") only partially explains the observations. Indeed, magnetic fields tend to decay because of magnetic diffusion, yet we observe that many magnetic field structures are much older than the typical diffusion time scale of the magnetized structure. Therefore another explanation is needed. The origin of astrophysical magnetic fields is not the only unanswered question in this field of research: The interaction of preexistent magnetic fields with forming structures is still object of investigations. Indeed, under certain circumstances, the presence of a magnetic field (regardless of its strength) can strongly affect the behavior of particular astrophysical structures (i.e., rotating disks of conducting fluid), by making those systems dynamically unstable. In the following, the two topics discussed above will be analyzed: The generation of magnetic fields in conducting fluids and the runaway effect that magnetic fields can foster in

rotating conducting fluids. The first effect is known as "dynamo" mechanism (or effect, or instability, or action), the second one as "magnetorotational instability" (MRI).

The **dynamo effect** is considered the most reasonable candidate to explain this ubiquitous presence of strong, non-decaying, and spatially well-behaved magnetic fields in most astrophysical fluid objects (e.g., planetary cores, stars, galaxies, and galaxy clusters). The name of the effect comes from those devices – known as *dynamos* – that are able to convert kinetic energy into electromagnetic energy. The first 19th-century current-generating machines consisted of a set of rotating coils in the field of permanent steel magnets. In 1866, the German industrialist and engineer Werner Siemens proposed to install electromagnets instead of using permanent magnets. In this way, the generated current itself could be twisted around the electromagnets in such a way that the magnetic field produced by the electromagnets would be amplified, and this – in turn – would amplify the generated current. The growth of the magnetic field eventually saturates for energetic reasons (the torque needed to run the machine becomes higher and higher and energy is conserved), but in the initial linear phase the growth is exponential, hence creating an unstable runaway effect. More precisely, this kind of à la Siemens devices are commonly known as *dynamo-electric* machines (in order to distinguish them from the *magneto-electric* devices that exploits permanent magnets). The mechanism of these dynamo machines depends of course on a suitable arrangement of multiply connected regions (usually wires) of high electrical conductivity within an insulating space and where solid materials are commonly used. In geo- and astrophysical environments, a magnetic instability is often invoked in order to explain the creation (or the stability) of the observed large-scale cosmic magnetic fields, and in this case the effect is known as *geophysical* or *astrophysical dynamo mechanism*. In these contexts, though, the scenario is quite different from the technical one: Astrophysical objects where the dynamo instability occurs are usually fluid, with a uniform and finite conductivity. Last, but not least, the topology of the astrophysical dynamos is simply connected (no planetary wires or electromagnets have been observed until now).

In 1919, Larmor [1] first proposed that the dynamo process might be able to explain the origin of magnetic fields in sunspots, but doubts were raised about the plausibility of this explanation. Mathematicians and geophysicists have been focusing on the conditions under which dynamo action occurs, but they usually ended up with proving anti-dynamo theorems, i.e., theorems that state under which conditions dynamos *do not* work. The first (and most famous) theorem has been proved by Cowling [2], who showed that axisymmetric or two-dimensional magnetic fields cannot be dynamo-generated. This raised even more doubts about whether the dynamo mechanism could occur in the core of the Earth, since the Earth's magnetic field is nearly axisymmetric. In 1958, Backus [3] and Herzenberg [4] were able

to show that non-axisymmetric fields could be generated by the dynamo mechanism.

The second topic we mentioned above is the so-called **magnetorotational instability** (MRI). This instability occurs in certain astrophysical plasmas and can be formally addressed – as for dynamo theory – in the framework of *magnetohydrodynamics* (MHD). This effect is considered the major candidate to explain the age-old problem (see below) of the unknown mechanism responsible for the transport of angular momentum from the inner regions toward the outer ones of rotating disks. Since such systems (differentially rotating fluids immersed in magnetic fields) are not rare at all in the observed universe, it becomes clear that this instability plays a very important role. Examples of such systems are: thin disks of gas around forming stars or in binary star systems, or – at larger scales – disks of interstellar medium rotating in the centre of galaxies. Those systems, known as *accretion disks*, can become extremely luminous sometimes: a gaseous disk surrounding a very massive black hole can give origin to quasars.

In a rotating disk, indeed, if matter falls inwards, it must lose angular momentum. On the other hand the total angular momentum of the disc must be conserved, therefore the mass far from the center of the disk must gain angular momentum somehow: An outward transport mechanism of the angular momentum must take place for matter to accrete. When first models of accretion disks appeared (late '40s, see [5]), an angular momentum transport mechanism had to be invoked – although not known in detail – in order to match the astrophysical observations. Since accretion disks are almost inviscid, ordinary molecular viscosity cannot explain the high efficient transport mechanism. Vigorous hydrodynamical turbulence – that can in fact give rise to an enhanced outward angular momentum transport – represents another possible explanation, yet its origin in those systems is still unclear. Hot disks of electrically conducting plasma can indeed become turbulent because of the linear magnetorotational instability [6]. On the other hand, cool disks (e.g., the planet-forming disks of protostars) may be too poorly ionized for the magnetorotational instability to occur, hence they are unmagnetized and linearly stable. Nevertheless, nonlinear hydrodynamic instability can occur also in linearly stable flows if their fluid Reynolds number is large, where the fluid Reynolds number is the ratio of inertia to viscous forces in the flow. Protoplanetary disks have in fact very high Reynolds numbers, but their Keplerian motion makes them hydrodynamically stable. The latter considerations (which can be found – e.g. – in [6]) have motivated the construction of laboratory experiments, and one of them [6] demonstrates that *non*-magnetic quasi-Keplerian flows at Reynolds numbers up to $\sim 10^6$ are *steady*. When this result is scaled to accretion disks, rates of angular momentum transport lie far below astrophysical requirements, so purely hydrodynamic turbulence is probably a poor candidate for explaining the high efficiency of outward transport of angular momentum.

The magnetorotational instability hence has become more and more popular as an explanation for the source of the turbulence in accretion disks: It makes the fluid unstable, it is a source of outward transport of angular momentum, it likely causes turbulence even in cool disks. In fact, the motion of conducting fluids (gases or liquids containing mobile charge carriers) can be influenced by magnetic fields: pressure, gravity, Coriolis, or other bulk forces are important as well as the Lorentz force. Moreover, if a conducting fluid is differentially rotating around a fixed point with an angular velocity decreasing with radial distance, the influence of the Lorentz force can be particularly destabilizing. Astonishingly, this effect works *regardless of the magnitude of the magnetic field*. The instability can be summarized in the following way: Those fluid parcels that – for any reason – undergo a small displacement from their original circular orbit, experience a force whose magnitude is *proportional* to the displacement, making the system unstable. This runaway effect is known as MRI.

The MRI was originally studied by Velikhov [7] and Chandrasekhar [8]. Although some other works followed [9–11], the MRI revival started from a work of Balbus and Hawley [12], who rediscovered and reformulated it in a more enlightening way. As already mentioned, the MRI importance in the astrophysical community is very well acknowledged, and the instability is extensively studied via numerics, theory, and – recently – also experiments. Those experiments have usually a size of the order of the meter and use – as a working fluid – liquid metals (such as liquid sodium or liquid gallium). In the following section we will briefly introduce two of such liquid-metal experiments, one concerning the dynamo mechanism, the other one concerning the magnetorotational instability.

1.2 Liquid metal experiments

Liquid metals are media that are commonly used at laboratory scales in order to study problems of astrophysical interest, since they share two important features with the media found in many astrophysical systems: They are fluid *and* conducting. Needless to say that, at the laboratory scales, it is impossible to reach the same physical parameters as the astrophysical objects that have inspired the design of those devices, but experiments are important to isolate and study on the Earth the physical principles behind the complex astrophysical phenomena under investigation. Similarly, it is still not possible – with modern computational resources – to have simulations running with the same physical parameters as the experiments. Nevertheless, by means of numerical simulations, a lot of interesting aspects can be analyzed and – as this dissertation hopefully shows – a lot can be learnt.

The best way of formally describing the dynamics of those conducting

fluids (i.e., fluids that can easily interact with magnetic fields) is by making use of magnetohydrodynamics, as mentioned above. It can be shown that this formalism can be derived from first principles, i.e., by approximating the exact kinetic equations (i.e., the equations describing the medium as a set of pointlike particles). The approximated version of the system of equations has a more restricted range of validity, since part of the information on the dynamics is lost in the approximation process. In particular, when the kinetic equations are reduced to the MHD equations, the most important approximations are: the closure of the infinite chain of equations describing the momenta of the governing kinetic equation, the use of a simplified version of Ohm's law, and the omission of relativistic effects (i.e., effects of finite light speed are ignored). By doing so, MHD is appropriate to describe fluid systems with low frequency dynamics (compared to light waves), where a static Ampere's law can be used (displacement currents are unimportant), where pressure forces are smaller than electric forces, where electrical currents as relative drifts are smaller than the fluid velocity, and where a single total pressure and a single velocity can be used to describe a globally neutral flow (there is no distinction between the dynamics of the different charge carrier species; moreover, the fluid carries approximately no charge). Liquid metals usually fall into this category of fluids and can be successfully described by MHD.

Two liquid metal laboratory experiments, relevant for astrophysical purposes, have been studied via numerical simulations: the Madison Dynamo Experiment (University of Madison-Wisconsin) and the Magnetorotational Instability Experiment (Princeton Plasma Physics Laboratory). The first experiment has been designed and built in order to study the generation of magnetic fields via dynamo action. By modeling the experiment, simulations can predict – for instance – how to modify the device in order to amplify the dynamo effect; moreover, simulations can have access to data in each point of the device (whereas – for technological reasons – this is not alway possible in laboratories). Furthermore, since hydrodynamic turbulence turned out to play a relevant role in this experiment (acting as a negative effect for the generation of the magnetic field in the device), many efforts – described in this thesis – have been made in order to understand the main features of the motion of the fluid in the device. The second experiment aims to study at laboratory scales the MRI. The main target of this second part of this PhD project has been the modeling of the experiment using a code written to study general problems with axisymmetric geometry in MHD. The feasibility of using this code has been carried out by benchmarking it with another code and with recent experimental results.

1.3 Contents of this dissertation

The outline of this dissertation is as follows: In Chapter 2 a brief general background is given, emphasizing three main aspects that are relevant for this dissertation: dynamo theory, the MRI, and turbulence. Chapter 3 deals with the liquid-metal apparatuses that have been working so far on the two instabilities, whereas in Chapter 4 the codes used to model and simulate the two systems have been described in detail. Chapter 5 describes the part of the project dedicated to the MRI simulations. In Chapter 6, first analyses of turbulence in the Madison Dynamo Experiment are shown, with particular emphasis on the study of the type of turbulence occurring in the experimental setup. Chapter 7 deals with our first attempts to reduce the influence of turbulence on the dynamo process, before we started using the Singular Value Decomposition technique, as described in Chapter 8. Conclusions and outlook of this work are outlined in Chapter 9.

Chapter 2

Theoretical fundamentals

> "An expert is one who knows more and more about less and less"
>
> William J. Mayo

The aim of this chapter is to provide the reader with the theoretical background that is needed to understand the main topics of this thesis. For further readings about dynamo theory, the tetxbook [13] is a comprehensive introduction to the generation of magnetic fields in conducting media. Concerning the Magnetorotational Instability, a complete overview can be found in [14]. Concerning general electromagnetism and the induction equation, we follow classical textbooks as [15] or [16]. For the derivation of the hydrodynamical equations, we follow textbooks like [17–21]. The material presented in this chapter is a combination of descriptions that can be found in the above-mentioned references.

As already stated in the introduction to this dissertation, the work we carried out is threefold, since three main topics have been explored in geometries that are relevant for experimental purposes: dynamo theory, the Magnetorotational Instability and turbulence in (magneto)hydrodynamics. The theoretical backgrounds of those three topics overlap, since magnetohydrodynamics (MHD) represents the common factor of these topics. MHD is the branch of plasma physics that studies the dynamics of conducting fluids (such as plasma, liquid metals, even sea water), therefore it represents the natural environment that has to be used in order to model the liquid sodium and liquid gallium experiments (i.e., the Madison Dynamo and the Magnetorotational Instability experiments, respectively) this dissertation deals with. The system of MHD equations is a combination of the Navier-Stokes equations for the hydrodynamic part (where the Lorenz force plays a role as a source of momentum) and the Maxwell equations for the description of the electromagnetic phenomena. All these equations are

indissolubly bound and should be solved simultaneously, a task that usually requires the help of numerical techniques. It is important to point out that MHD cannot model kinetic phenomena, i.e., it treats conducting media as continuous ones, hence neglecting the effect do to the fact that particles are discrete and that are – under certain circumstances – non-thermal [22]. Nevertheless, the MHD system can be rigorously derived from the kinetic equations (as very didactically shown in [16]) and can be seen as an approximation of the kinetic approach when collisions among particles occur very frequently and when the macroscopic velocities are way smaller than the speed of light.

Contents

2.1 Governing equations: Hydrodynamics 14
2.1.1 Lagrangian and Eulerian frames of reference in fluid dynamics 14
2.1.2 The continuity equation 15
2.1.3 The momentum equation 16
2.2 The induction equation 19
2.3 Putting all together: the system of governing equations 20
2.4 Waves, instabilities, and turbulence 21
2.4.1 Magnetorotational Instability 21
2.4.2 The weak spring picture 22
2.4.3 Dynamo theory 25
2.4.4 Kolmogorov's theory of small scale turbulence . . . 31

2.1 Governing equations: Hydrodynamics

In this section, we will review the derivation of the equations governing the dynamics of fluids. We will start by describing the two frames of reference traditionally used to describe fluid dynamics and then derive the physical equations.

2.1.1 Lagrangian and Eulerian frames of reference in fluid dynamics

In the Eulerian specification of the flow field, the flow quantities are described as a function of position $\mathbf{r}$ and time t. E.g., the velocity field of the flow is described by a vector field $\mathbf{u}(\mathbf{r}, t)$, where the position $\mathbf{r}$ is a variable independent of t.

In the Lagrangian specification of the fluid motion, individual fluid parcels are followed through time. Each fluid parcel is labelled with a time-independent

vector $\mathbf{X}$, which represents the position of the parcel at $t = 0$. Each fluid parcel will have, at time t, position $\mathbf{x}(\mathbf{X}, t)$. In other words, the function $\mathbf{x}(\mathbf{X}, t)$ describes the trajectory (or "pathline") of the parcel at position $\mathbf{X}$ at $t = 0$. The two description are linked by the equation

$$\mathbf{u}(\mathbf{r}, t)\Big|_{\mathbf{r}=\mathbf{x}(\mathbf{X},\mathbf{t})} = \frac{\partial}{\partial t}\mathbf{x}(\mathbf{X}, t), \tag{2.1}$$

since both sides describe the velocity the parcel labeled will have at time t. Within a chosen coordinate system, $\mathbf{X}$ and $\mathbf{r}$ are called – respectively – the Lagrangian coordinates and the Eulerian coordinates of the flow.

2.1.2 The continuity equation

The continuity equation expresses conservation of mass in mathematical form. Within a geometrical volume V, fixed in space and time, the rate of change of mass is equal to the mass flux crossing the surface ∂V of the volume V, since no source or sink of mass is present in the volume. Mathematically:

$$\frac{\mathrm{d}}{\mathrm{d}t}\int_V \rho \mathrm{d}V + \int_{\partial V} \rho \mathbf{u} \cdot \mathbf{n} \mathrm{d}S, \tag{2.2}$$

where v is the velocity of the fluid, ρ its density, $\mathbf{n}$ the unit vector normal to the surface and pointing outwards. The surface integral can be replaced by a volume integral via the Gauss theorem, and we have

$$\int_V \left[\frac{\partial \rho}{\partial t} + \nabla \cdot (\rho \mathbf{u})\right] \mathrm{d}V = 0. \tag{2.3}$$

This integral equation holds for any arbitrary volume, therefore the integrand must locally vanish, yielding to the so-called continuity equation:

$$\frac{\partial \rho}{\partial t} + \nabla \cdot (\rho \mathbf{u}) = 0. \tag{2.4}$$

This equation is readily written also in the Lagrangian frame of reference, i.e.,

$$\frac{1}{\rho}\frac{D\rho}{Dt} + \mathcal{D} = 0, \tag{2.5}$$

where the operator $D/Dt = \mathrm{d}/\mathrm{d}t + \mathbf{u} \cdot \nabla$ is the Lagrangian (or material or substantial) derivative, which describes the rate of change of a quantity along the trajectory of the flow, and the term $\mathcal{D} = \nabla \cdot \mathbf{u}$ is called *dilatation*. In incompressible conditions (flows of constant density) we have – both for steady and unsteady flows – that

$$\nabla \cdot \mathbf{u} = 0. \tag{2.6}$$

This condition is enforced in both the codes used throughout this thesis.

2.1.3 The momentum equation

According to Newton's second law of dynamics, the temporal rate of change of linear momentum of a mass is equal to the sum of the forces $\mathbf{F}_k$ acting on the mass. In our case, the mass is represented by a fluid parcel, treated as a closed system (denoted by "cs" in the following), i.e., no fluid flows across its boundaries. In this case, Newton's law becomes

$$\frac{\mathrm{d}}{\mathrm{d}t}\int \rho\mathbf{u}\mathrm{d}V_{cs} = \sum_k \mathbf{F}_k. \tag{2.7}$$

If the control volume V is fixed in space and time with flow allowed to cross its boundaries, the following equation holds

$$\frac{\mathrm{d}}{\mathrm{d}t}\int \rho\mathbf{u}\mathrm{d}V_{cs} = \int_V \frac{\partial}{\partial t}(\rho\mathbf{u})\mathrm{d}V + \int_{\partial V} \rho\mathbf{u}(\mathbf{u}\cdot\mathbf{n})\mathrm{d}S. \tag{2.8}$$

This equation accounts for possible changes of the linear momentum per unit mass $\rho\mathbf{u}$ due to internal change (first term on the right hand side) or due to transport of momentum across the boundaries of V (second term). Using again Gauss theorem, we find

$$\frac{\mathrm{d}}{\mathrm{d}t}\int \rho\mathbf{u}\mathrm{d}V_{cs} = \int_V \left(\frac{\partial}{\partial t}(\rho\mathbf{u}) + \nabla\cdot(\rho\mathbf{u}\mathbf{u})\right)\mathrm{d}V, \tag{2.9}$$

which becomes, using the continuity equation,

$$\frac{\mathrm{d}}{\mathrm{d}t}\int \rho\mathbf{u}\mathrm{d}V_{cs} = \int_V \rho\frac{D\mathbf{u}}{Dt}\mathrm{d}V. \tag{2.10}$$

Surface forces (acting on the boundaries) and body forces (acting on the bulk of the fluid) contribute to the sum of the forces $\sum_k \mathbf{F}_k$. The nature of the surface forces depends on whether we consider viscous or inviscid flows. In the ideal case when viscosity can be neglected, the only surface force is the force due to the pressure p, acting orthogonally to the surface of the parcel; hence we have

$$\sum_k \mathbf{F}_k = \int_V \rho\mathbf{f}\mathrm{d}V - \int_{\partial V} p\mathbf{n}\mathrm{d}S, \tag{2.11}$$

where $\mathbf{f}$ is a generic volume force per unit mass. Using Gauss' theorem,

$$\sum_k \mathbf{F}_k = \int_V (\rho\mathbf{f} - \nabla p)\mathrm{d}V, \tag{2.12}$$

and we finally retrieve the so-called *Euler's equation*, which holds in inviscid conditions:

$$\rho \frac{D\mathbf{u}}{Dt} = \rho \mathbf{f} - \nabla p. \tag{2.13}$$

For viscous fluids, in Eq. (2.12) one should consider that the surface stress can produce a net stress in *any* direction. A tensor should then be introduced, whose ij-th component is denoted by σ_{ij}. The average of the normal stress is set equal to the negative of the pressure, whereas the remaining terms describe the effects of the viscous nature of the flow. Putting all together, contributions of the viscous stress forces and the pressure are described by the viscous or *deviatoric* stress tensor τ, whose ij-th component reads $\tau_{ij} = p\delta_{ij} + \sigma_{ij}$. We hence have

$$\rho \frac{D\mathbf{u}}{Dt} = \rho \mathbf{f} - \nabla p + \nabla \cdot \boldsymbol{\tau}. \tag{2.14}$$

This last equation turns out to be usable if one can relate the viscous stresses to the rate of strain, namely the velocity gradients. In order to write those relationships, assumptions on the fluid under consideration are required. It can be experimentally verified by shearing a fluid layer between parallel plates that a large number of fluids satisfies the relation

$$\tilde{\tau} = \mu \frac{\partial u}{\partial y} \tag{2.15}$$

where $\tilde{\tau}$ is the shear stress exerted on a fluid parcel and the velocity gradient is perpendicular to the direction of the shear [23]. The constant of proportionality μ is the dynamic viscosity and fluids that satisfy equation (2.15) are called Newtonian fluids. In three dimensions, the viscous stress tensor for a Newtonian fluid becomes, analogously,

$$\tau_{ij} = \mu \left(\frac{\partial u_i}{\partial x_j} + \frac{\partial u_j}{\partial x_i} - \frac{2}{3}\delta_{ij} \frac{\partial u_k}{\partial x_k} \right) + \delta_{ij} \tilde{\mu} \frac{\partial u_k}{\partial x_k}, \tag{2.16}$$

where $\tilde{\mu}$ is the so-called second coefficient of viscosity. If the viscosity coefficients are constant, by taking the divergence of the stress tensor, the equation of motion for the fluid parcel becomes

$$\rho \left(\frac{\partial \mathbf{u}}{\partial t} + (\mathbf{u} \cdot \nabla)\mathbf{u} \right) = -\nabla p + \mu \nabla^2 \mathbf{u} + \left(\tilde{\mu} + \frac{1}{3}\mu \right) \nabla(\nabla \cdot \mathbf{u}) + \rho \mathbf{f}, \tag{2.17}$$

namely the so-called *Navier-Stokes* equation. The third term vanishes if the flow can be considered to be incompressible (since $D\rho/Dt = 0$). Liquid metals, such the ones used in the experiments modeled and described in this thesis, can be considered incompressible with a high order of accuracy. The

term proportional to $\mathbf{f}$ describes the body forces, as already stated. For the purposes of modeling laboratory systems where a conducting flow is stirred and immersed in a background magnetic fields $\mathbf{B}$, Lorentz force plays an important role. Its expression, per unit volume, is given by

$$\mathbf{f}_L = \mathbf{j} \times \mathbf{B}, \tag{2.18}$$

where $\mathbf{j}$ is the current density, which is related to the magnetic field via Ampere's law. Neglecting the displacement current, Eq. (2.18) becomes

$$\mathbf{f}_L = \frac{1}{\mu_0}(\nabla \times \mathbf{B}) \times \mathbf{B}. \tag{2.19}$$

Therefore, the conservation of momentum in an electrically conducting incompressible fluid streaming at non-relativistic velocities is expressed by the so-called *extended Navier-Stokes equation*, which can be written as

$$\frac{\partial \mathbf{u}}{\partial t} + (\mathbf{u} \cdot \nabla)\mathbf{u} = -\nabla P + \nu \nabla^2 \mathbf{u} + \mathbf{j} \times \mathbf{B}, \tag{2.20}$$

where the $P = p/\rho$ is the reduced pressure and $\nu = \mu/\rho$ is the kinematic viscosity.

In the incompressible case and neglecting body forces, the pressure field can be obtained from a known velocity field by taking the divergence of the Navier-Stokes equation. In this way, a Poisson equation is obtained, namely

$$\nabla^2 p = -\rho \frac{\partial^2 u_i u_j}{\partial x_j \partial x_i}. \tag{2.21}$$

On the other hand, the pressure gradient force can be eliminated from the Navier-Stokes equation by taking the curl of the equation itself, hence obtaining the so-called *vorticity transport equation*, i.e.,

$$\frac{\partial \boldsymbol{\omega}}{\partial t} = \nabla \times (\mathbf{u} \times \boldsymbol{\omega}) + \nu \nabla^2 \boldsymbol{\omega} \tag{2.22}$$

where $\boldsymbol{\omega} = \nabla \times \mathbf{u}$ is the *vorticity field*. If incompressibility holds, last equation can be transformed into

$$\frac{\partial \boldsymbol{\omega}}{\partial t} + (\mathbf{u} \cdot \nabla)\boldsymbol{\omega} = (\boldsymbol{\omega} \cdot \nabla)\mathbf{u} + \nu \nabla^2 \boldsymbol{\omega}. \tag{2.23}$$

The vorticity equation 2.23 states that vorticity is advected by the velocity flow (as the left hand side shows), it is stretched and tilted by velocity gradients and diffused away by viscosity. This equation can be solved if the pressure is not needed explicitly, since in the incompressible case $\boldsymbol{\omega}$ retains the whole information on the velocity field. The `DYNAMO` code – as described in Chapter 4 – uses this method.

2.2 The induction equation

Electric and magnetic fields are governed by Maxwell's equations [15]. In SI units these equations read

$$\nabla \cdot \mathbf{B} = 0, \tag{2.24}$$

$$\nabla \cdot \mathbf{E} = \rho_c/\epsilon_0, \tag{2.25}$$

$$\nabla \times \mathbf{B} = \mu_0 \left(\mathbf{j} + \epsilon_0 \frac{\partial \mathbf{E}}{\partial t} \right), \tag{2.26}$$

$$\nabla \times \mathbf{E} = -\frac{\partial \mathbf{B}}{\partial t}, \tag{2.27}$$

where ρ_c is the electric charge density, ϵ_0 the permittivity of free space, and μ_0 the permeability of free space. The second term on the right hand side of equation (2.26) is the displacement current. It ensures the invariance of the equations under the Lorentz transformation and is the a fundamental term since it gives to the solution of the equations wavelike properties. In the context of dynamo theory any fluid motion is usually assumed to be slower by orders of magnitude than the speed of light. In other words, sources are steady or quasi-steady (slowly varying), and the displacement current can be neglected, leading to the so-called pre-Maxwell set of equations.

The system is not closed if we do not indicate a relation between the current density and the fields. Ohm's law relates these quantities. In a frame at rest relative to a homogeneous and isotropic electrically conducting fluid, the relation is

$$\mathbf{j}' = \sigma \mathbf{E}', \tag{2.28}$$

where σ is a the scalar electric conductivity (a tensor, for inhomogeneous and anisotropic materials). The electric field is not invariant and is subject to the transformation law $\mathbf{E}' = \mathbf{E} + \mathbf{u} \times \mathbf{B}$. Therefore, in the laboratory frame relatively to which the electrically conducting fluid is streaming at the velocity $\mathbf{u}$ Ohm's law takes the form

$$\mathbf{j} = \sigma(\mathbf{E} + \mathbf{u} \times \mathbf{B}). \tag{2.29}$$

Dividing Eq. (2.29) by σ, taking the curl, and eliminating the electric field via Eq. (2.27), we obtain

$$\nabla \times \left(\frac{\mathbf{j}}{\sigma} \right) = -\frac{\partial \mathbf{B}}{\partial t} + \nabla \times (\mathbf{u} \times \mathbf{B}). \tag{2.30}$$

The current density can in turn be eliminated by inserting the pre-Maxwell form of Eq. (2.26). If the conductivity is constant over space, we have

$$\frac{\partial \mathbf{B}}{\partial t} = \nabla \times (\mathbf{u} \times \mathbf{B}) + \eta \nabla^2 \mathbf{B}, \tag{2.31}$$

i.e., the so-called *magnetic induction equation*. This equation plays a fundamental role in dynamo theory, since it is the main governing equation for the generation of magnetic fields in electrically conducting media. The first term on the right hand side represents the generation of magnetic field due to electrical currents that are induced when an electrical conductor moves relative to a magnetic field. The second term describes dissipation of magnetic field due to Joule heating that electrical currents are subject to when they flow in a conductor with non-zero resistivity. Since the magnetic field is divergence-free, Eq. (4.6) can be recast in the following way

$$\frac{\partial \mathbf{B}}{\partial t} + (\mathbf{u} \cdot \nabla)\mathbf{B} = (\mathbf{B} \cdot \nabla)\mathbf{u} + \eta \nabla^2 \mathbf{B}. \tag{2.32}$$

In the left hand side we recognize the material derivative $D\mathbf{B}/Dt$, i.e., the rate of change of the magnetic field along the flow. This last equation shows that this temporal change depends on the stretching of the magnetic field due to the velocity field and on Joule dissipation.

2.3 Putting all together: the system of governing equations

The fundamental equations that govern the dynamics of liquid metals in typical experimental apparatuses are the incompressible extended Navier-Stokes equations coupled to the induction equation. The system reads

$$\rho \frac{\partial \mathbf{u}}{\partial t} + (\rho \mathbf{u} \cdot \nabla)\mathbf{u} = -\nabla p + \rho \nu \nabla^2 \mathbf{u} + \mathbf{j} \times \mathbf{B}, \tag{2.33}$$

$$\frac{\partial \mathbf{B}}{\partial t} = \nabla \times \Big(\mathbf{u} \times \mathbf{B} - \frac{1}{\mu_0 \sigma} \nabla \times \mathbf{B} \Big), \tag{2.34}$$

where ρ is the density of the fluid, $\mathbf{u}$ its velocity, ν its kinematic viscosity, σ its conductivity, $\mathbf{B}$ the magnetic field, and

$$\mathbf{j} = \frac{1}{\mu_0} \nabla \times \mathbf{B} \tag{2.35}$$

the current (the displacement current is negligible for quasi-stationary sources). The constraints on the incompressibility of the flow reads $\nabla \cdot \mathbf{u} = 0$. In writing down the induction equation, we have assumed that Ohm's law takes the form [15]

$$\mathbf{j} = \sigma(\mathbf{E} + \mathbf{u} \times \mathbf{B}), \tag{2.36}$$

with **j** and the electric field **E** are measured in a local rest frame. Combining Ohm's law, Faraday's law and Ampere's law (2.35), the induction equation (2.34) follows. The constraint $\nabla \cdot \mathbf{B} = 0$ (no magnetic monopoles) is assured by Eq. (2.34) if it is imposed as an initial condition.

In order to grasp the physical meaning of the phenomena studied for this thesis, we briefly describe the exact Lagrangian solution to the induction equation in the ideal case when the resistivity $\eta = 1/(\mu_0 \rho)$ is negligible [24] and the fluid is compressible. Although this solution (the so-called "frozen in" picture) holds only in the ideal case, becoming wrong in real fluids where diffusion cannot be neglected and magnetic reconnection takes place, it turns out to be pedagogical. As already stated, a compressible fluid obeys the continuity equation

$$\frac{\partial \rho}{\partial t} + \nabla \cdot (\rho \mathbf{u}) = \frac{\mathrm{d}\rho}{\mathrm{d}t} + \rho \nabla \cdot \mathbf{u} = 0, \tag{2.37}$$

where the Lagrangian derivative is

$$\frac{\mathrm{d}}{\mathrm{d}t} = \Big(\frac{\partial}{\partial t} + \mathbf{u} \cdot \nabla \Big). \tag{2.38}$$

By expanding the induction equation (2.34) and then combining it with the continuity equation (2.37) in order to eliminate the term proportional to $\nabla \cdot \mathbf{u}$, we find

$$\frac{\mathrm{d}}{\mathrm{d}t} \left(\frac{\mathbf{B}}{\rho} \right) = \left(\frac{\mathbf{B}}{\rho} \cdot \nabla \right) \mathbf{u}. \tag{2.39}$$

This evolution equation happens to be the same one obeyed by an infinitesimal element $\mathrm{d}\mathbf{x}(t)$ embedded in the fluid (i.e., connecting two close real "particles" of the fluid or two close fluid "parcels"), which is

$$\frac{\mathrm{d}}{\mathrm{d}t} \mathrm{d}\mathbf{x} = \mathrm{d}\mathbf{x} \cdot \nabla \mathbf{u}, \tag{2.40}$$

as an elementary geometrical construction shows (see Appendix B). We will make explicit use of this result in the following sections where a description of the dynamo effect and the MRI has been carried out. Moreover, in next Section, we will give a general overview of turbulence and its role in the dynamo systems.

2.4 Waves, instabilities, and turbulence

2.4.1 Magnetorotational Instability

The Magnetorotational Instability (MRI) is considered the main candidate to explain the unexpected fast transport of angular momentum toward outer

radii in accretion disks around stars and black holes. This instability has been originally studied by Velikhov [7] and Chandrasekhar [8] and then rediscovered by Balbus and Hawley [12], who showed that Keplerian disks, for which the Rayleigh criterion predicts axisymmetric hydrodynamical stability, can be destabilized is a weak magnetic field is present. In general, the MRI occurs when a weak magnetic field is applied to a rotating electrically conducting fluid whose angular velocity Ω decreases with the distance from the rotation axis, i.e., $\partial\Omega(R)/\partial R < 0$. Linear stability analysis shows that the most unstable mode is axisymmetric and associated with a strong radial outflow of angular momentum, which provides a simple explanation to the problem of the angular momentum transport. Non-linear evolution of the MRI is of primary importance, since saturation of the instability eventually yields a magnetohydrodynamical turbulent state, enhancing the angular momentum transport [25]. Let us consider, in cylindrical geometry (R, z, ϕ), Eqs. (2.33), (2.34) and (2.37). Let the electrically conducting fluid have the shape of a rotating disk (with differential rotation $\Omega(r)$) and let it be in the presence of a large scale magnetic field with components $(0, B_z, B_\phi)$[1]. By perturbing quantities such as $\mathbf{u}$, $\mathbf{B}$, the pressure P, and the density ρ with perturbations whose spatiotemporal form is $\exp i(kz - \omega t)$, a dispersion relation can be extracted (i.e., a formula that gives the frequency ω of a perturbation with wave number $\mathbf{k}$). In the absence of rotation ($\Omega(R) = 0$), this dispersion relation has three solutions, i.e., it foresees three kind of modes: the so-called Alfvén waves, the fast and the slow magnetosonic waves. The first ones are compressionless disturbances that propagate along the magnetic field lines. The second (third) ones propagates with a faster (slower) velocity. On the other hand, when the rotation of the disk is not neglected, the dispersion relation shows that the slow mode becomes *unstable* (the square of its frequency becomes negative leading to a growing/decaying amplitude of the wave-like perturbation). In the following section, the dispersion relation will be derived in a simplified – albeit didactic – scenario, known as "weak-spring picture".

2.4.2 The weak spring picture

The Magnetorotational Instability can be didactically described by the so-called "weak-spring picture". Let us consider a rotating conducting fluid under conditions of ideal MHD and let us perturb the physical quantities of interest. Then, a fluid parcel will be displaced from its circular orbit by an amount ξ (with $\xi(R, z) = (\xi_R, \xi_\phi, 0) \exp ikz$), and the "frozen-in" induction equation becomes

[1]The component B_R does not play an important role in the analysis instability, it would just cause a linear time dependence in B_ϕ. Since the weak-field axisymmetric instability carries on independently of B_ϕ, it will not be considered for the sake of simplicity

$$\delta \mathbf{B} = ikB\xi, \tag{2.41}$$

with $\delta B_Z = 0$. The magnetic tension force ($\equiv (\frac{\mathbf{B}}{\mu_0 \rho} \cdot \nabla)\mathbf{B}$) becomes, under the effect of the perturbing disturbances,

$$\frac{ikB}{\mu_0 \rho}\delta \mathbf{B} = -(\mathbf{k} \cdot \mathbf{u}_A)^2 \xi, \tag{2.42}$$

where $mathbfu_A$ is the Alfvén velocity. The equations of motion of the displacement ξ become

$$\ddot{\xi}_R - 2\Omega\dot{\xi}_\phi = -\left(\frac{\mathrm{d}\Omega^2}{\mathrm{d}\ln R} + (\mathbf{k} \cdot \mathbf{u}_A)^2\right)\xi_R, \tag{2.43}$$

and

$$\ddot{\xi}_\phi + 2\Omega\dot{\xi}_R - (\mathbf{k} \cdot \mathbf{u}_A)^2 \xi_\phi. \tag{2.44}$$

These equations describe the same dynamics of two orbiting masses connected by a spring whose spring constant is $(\mathbf{k} \cdot \mathbf{u}_A)^2$. This coincidence is particularly enlightening. Let us consider those two mass points, initially circulating on the same orbit, that are displaced to two new close orbits. Mass m_i orbits now at inner radius R_i, whereas mass m_o at outer radius R_o. In a Keplerian disk, particles at inner orbits rotate more rapidly, so mass m_i would increase its angular velocity, the contrary applies to m_o. In this scenario, the string connecting the two masses starts stretching and the tension would decelerate m_i and accelerate m_o. In other words, mass m_i lost angular momentum in this process and it is hence forces to occupy an even lower orbit, while mass m_o acquires more angular momentum an occupies a higher one. It is clear from this picture, that this mechanism explains the transport of angular momentum from the inner radii to the outer radii. At this point, the separation between the two masses is larger and the spring tension gets higher and a runaway effect takes place.

For this instability to occur, the spring must be weak. If the spring constant is too high, the oscillation frequency of the spring would be too high compared to the orbital time and the runaway effect would not work. This last consideration can be understood by looking at the right-hand side of Eq. (2.43). If the magnetic field amplitude is high enough, such that

$$(\mathbf{k} \cdot \mathbf{u}_A) \geq -\frac{\mathrm{d}\Omega^2}{\mathrm{d}\ln R}, \tag{2.45}$$

then the restoring force is too high and the system is stable. In other words, MRI will not occur unless both the rotation period and the Alfvén crossing time are shorter than the timescale for magnetic diffusion. The dimensionless quantity that measures the ratio of the resistive diffusion timescale τ_σ to

the Alfvén wave crossing timescale τ_A is called Lundquist number, usually indicated with S. Indicating with L the characteristic length scale of the system and with B_0 the background field, we have that

$$\tau_\sigma = \mu_0 \sigma L^2 = \frac{L^2}{\eta}\,, \qquad \tau_A = \frac{u_A}{L} = \frac{B_0}{L\sqrt{\mu_0 \rho}} \tag{2.46}$$

Thus, in SI units, the Lundquist number $S = T_D/T_A$ reads

$$S = \frac{B_0 L}{\eta\sqrt{\mu_0 \rho}}. \tag{2.47}$$

The Lundquist number becomes very large for highly conducting plasmas; for laboratory plasmas S is typically on the order of 10^2–10^8 (whereas in the simulations described in the next Chapters, S is less than 10, hence it is low, indicating a resistive flow). The condition described above (i.e., that the MRI will not occur unless both the rotation period and the Alfvén crossing time are shorter than the timescale for magnetic diffusion) is translated into the conditions $Rm > 1$ and

$$S \equiv \frac{BL}{\eta\sqrt{\mu_0 \rho}} > 1. \tag{2.48}$$

It can happen, however, that the geometry of the system allows disturbances whose wavenumber k is small enough such that they do not fulfill the stability criterion (2.45), and in this case all the perturbations with a higher wavelength would grow exponentially in the linear regime. In other words, in this ideal case, the magnetic field is never too small to be dynamically ignored. This last eventuality happens, for instance, if one considers infinite systems. On the other hand, if

$$\frac{\mathrm{d}\Omega^2}{\mathrm{d}\ln R} > 0, \tag{2.49}$$

the stability is assured, regardless of the wavelength of the disturbances. It is worth noticing that, due to the gravitational potential and, hence, the typical functional form of $\Omega(R)$ in astrophysical disks, this condition is usually not satisfied. In the most realistic case where the disk has a finite vertical height, it goes without saying that there would be a restriction on the maximum wavelength permitted by the disturbances, which cannot exceed the vertical thickness of the disk. From Eqs. (2.43) and (2.44), assuming for ξ a temporal functional form of $\exp(-i\omega t)$, the following dispersion relation can be easily obtained,

$$\omega^4 - \omega^2[\kappa^2 + 2(\mathbf{k}\cdot\mathbf{u}_A)^2] + (\mathbf{k}\cdot\mathbf{u}_A)^2\left((\mathbf{k}\cdot\mathbf{u}_A)^2 + \frac{\mathrm{d}\Omega^2}{\mathrm{d}\ln R}\right) = 0, \qquad (2.50)$$

where $\kappa^2 = \frac{1}{R^3}\frac{R^4\Omega^2}{\mathrm{d}R}$ is usually known as *epicyclic frequency*. This equation foresees a maximum *unstable* mode, whose growth rate is

$$|\omega_{max}| = \frac{1}{2}\left|\frac{\mathrm{d}\Omega}{\mathrm{d}\ln R}\right|. \qquad (2.51)$$

This unstable mode develops if its wavenumber satisfies the relation

$$(\mathbf{k}\cdot\mathbf{u}_A)^2_{max} = -\left(\frac{1}{4} + \frac{\kappa^2}{16\Omega^2}\right)\frac{\mathrm{d}\Omega^2}{\mathrm{d}\ln R}. \qquad (2.52)$$

For instance, in a system rotating with a Keplerian profile, we would have

$$|\omega_{max}| = \frac{3}{4}\Omega, \qquad (2.53)$$

and

$$(\mathbf{k}\cdot\mathbf{u}_A)^2_{max} = \frac{\sqrt{15}}{4}\Omega. \qquad (2.54)$$

Until now, we have briefly reviewed a simplified mechanism that underlies the magnetorotational instability. Magnetohydrodynamics is the most suitable theoretical framework for the modeling of such an instability. Analogously, dynamo theory is based on magnetohydrodynamics. As for the magnetorotational instability, the coupling of the magnetic field with the fluid motion creates an unstable situation, leading to the growth of the magnetic field if particular conditions are satisfied. In next Section, a general overview of dynamo theory will be given.

2.4.3 Dynamo theory

The dynamo effect is the main candidate for explaining the origin of the magnetic field in astrophysical environments, such as planets, stars, galaxies. The idea is the following: Since the continuum, conducting fluid (e.g., a plasma, a mixture of liquid metals, the interstellar medium) is in motion, a magnetic field already present would have a time-varying flux across a certain surface, hence inducing currents in the fluid. If the configuration (the geometry of the motion, the topology of the magnetic field, etc.) is right, then these induced currents reinforce the original source currents that created the initial magnetic field. In other words, this process converts the kinetic energy of the fluid into magnetic energy. Finding the favorable condi-

tions to dynamo action is one of the goal of dynamo theory, both theoretical and experimental. In his seminal textbook "Magnetic Field Generation in Electrically Conducting Fluids", Moffatt [13] gives a formal definition of a dynamo: the velocity field of an isolated, magnetized, resistive fluid acts as a dynamo if

$$\lim_{t\to\infty} E_B(t) \neq 0, \tag{2.55}$$

where E_B is defined as

$$E_B(t) = \frac{1}{\mu_0}\int_{V_\infty} |\mathbf{B}(\mathbf{x},t)|^2. \tag{2.56}$$

Classical examples of dynamos are: the Sun and the Earth. These two systems have a magnetic field that does not decay in time in spite of the fact that the magnetic diffusion time is way shorter than their age. In 1919, Larmor published a paper with the self-explanatory title "How could a rotating body such as the Sun become a magnet?" [1]. On the other hand, the magnetic field of the Earth was not considered a dynamo because it was still believed that the magnetic field of our planet was caused by permanent magnetization of its interior. Nowadays, the temperature of the Earth's interior is known to be above the critical Curie temperature at which ferromagnetic materials lose their permanent magnetization. Recent experimental investigations have determined the temperature near the Earth's centre to be 6230 ± 500 K [26], i.e., 1000 degrees hotter than in a previous experiment run 20 years ago [27]. Furthermore, seismological observations tell us that the Earth's interior (at least a large fraction of it) is in liquid state, so a dynamo mechanism is a good candidate to justify the non-decaying behavior of the magnetic field of the Earth.

Astrophysical or the laboratory systems where dynamo action takes place are generally turbulent, making the mathematical treatment of the effect difficult. Nevertheless, dynamo action in turbulent media can be described very elegantly by the so-called Mean Field Theory (MFT). This theory was formulated by Steenbeck, Krause, and Rädler [28], who took into account the effect of turbulence on MHD systems, treating the problem in a relatively simple analytical way. The starting point of MFT is the splitting of the velocity and magnetic fields into *mean* fields and *fluctuating* fields. This is motivated by the usual picture that in a turbulent field it is often possible to distinguish a large-scale (almost stationary and smooth) mean field and small-scale turbulent fluctuations whose amplitude is much smaller than the amplitude of the mean fields:

$$\mathbf{B} = \overline{\mathbf{B}} + \mathbf{B}', \qquad \mathbf{u} = \overline{\mathbf{u}} + \mathbf{u}', \tag{2.57}$$

where the overbar denotes an appropriate averaging process (e.g. time av-

erage or ensemble average). It is assumed that, given a generic fluctuating field $\mathcal{F}$, the splitting is such that $\overline{\overline{\mathcal{F}}} = \overline{\mathcal{F}}$ and $\overline{\mathcal{F}'} = 0$. It is worth noticing that the hypothesis which leads to Equations (2.57) is not trivial: the scale separation between the small-scale turbulence and the system-scale fields is not always satisfied, especially in systems where large scales carry the most turbulent energy[2] If this scale separation hypothesis is valid, the averaging procedure can be applied to the induction equation (2.34), and after some simple manipulations we find the equations that govern the evolution of the mean magnetic field and its fluctuating component, i.e.,

$$\frac{\partial \overline{\mathbf{B}}}{\partial t} = \nabla \times \left(\overline{\mathbf{u}} \times \overline{\mathbf{B}} + \overline{\mathbf{u}' \times \mathbf{B}'} - \eta \nabla \times \overline{\mathbf{B}} \right), \tag{2.58}$$

$$\frac{\partial \mathbf{B}'}{\partial t} = \nabla \times \left(\mathbf{u}' \times \overline{\mathbf{B}} + \overline{\mathbf{u}} \times \mathbf{B}' + \mathbf{G} - \eta \nabla \times \mathbf{B}' \right), \tag{2.59}$$

where

$$\mathbf{G} = \mathbf{u}' \times \mathbf{B}' - \overline{\mathbf{u}' \times \mathbf{B}'}. \tag{2.60}$$

In the derivation of these two equations, it has been taken into account that terms like $\mathbf{u}' \times \overline{\mathbf{B}}$ have zero average, while the second order term $\overline{\mathbf{u}' \times \mathbf{B}'}$ is, in principle, non-zero due to possible correlations between the fluctuating fields. By comparing Eqs. (2.58) and (2.59), we see that the mean field obeys an induction-like equation, but with an additional source term, i.e.,

$$\mathcal{E} = \overline{\mathbf{u}' \times \mathbf{B}'}, \tag{2.61}$$

called *turbulent electromotive force* (emf).

Kinematic dynamo theory and the α effect

Eq. (2.59) suggests that the fluctuating, turbulent component of the magnetic field is generated by induction due to the coupling of the fluctuating, turbulent component of the velocity, i.e., $\mathbf{u}'$, and the local mean magnetic field $\overline{\mathbf{B}}$. If the magnetic field is weak, the action of the Lorentz force on the fluid is negligible (see Eq. (2.33)). In this regime, i.e., if $\mathbf{u}'$ does not depend on $\mathbf{B}$,Eq. (2.59) becomes linear in $\overline{\mathbf{B}}$, hence it makes sense to infer that the emf $\mathcal{E}$ is a linear functional of $\overline{\mathbf{B}}$. This conjecture is the key assumption in MFT and in this regime dynamo theory is referred to as *kinematic dynamo theory*. The above-mentioned linear expansion reads

$$\overline{\mathbf{u}' \times \mathbf{B}'}_i = \alpha_{ij} \overline{B}_j + \beta_{ijk} \frac{\partial \overline{B_j}}{\partial x_k} + ... \tag{2.62}$$

[2]One of the motivations of the work described in this Ph.D. thesis was the investigation of whether large scale turbulence or rather small scale turbulence had the most detrimental effect in the Madison Dynamo Experiment, hence whether the system really fulfills the MFT hypotheses. This problem will be described in Chapter 8.

where the pseudo-tensors α_{ij} and β_{ijk} in general depend on both components of the flow, $\mathbf{u}'$ and $\overline{\mathbf{u}}$, and are determined by the statistical properties of the turbulence. The α term plays a fundamental role in kinematic dynamo theory. In order to understand its effect, let us consider a simplified scenario, where the mean velocity and the magnetic diffusivity are negligible, and where turbulence is isotropic, i.e.,

$$\alpha_{ij}\overline{B}_j = \alpha\overline{B}_i. \tag{2.63}$$

The induction equation becomes

$$\frac{\partial\overline{\mathbf{B}}}{\partial t} = \nabla \times (\alpha\overline{\mathbf{B}}). \tag{2.64}$$

Solution to this equation based on force-free configurations ($\nabla \times \mathbf{B} \propto \mathbf{B}$) grow exponentially in time, remaining force-free. In Appendix B it is shown which property of the fluid goes into determining α.

The dynamo problem can be simplified by considering the reduced approach, called *kinematic dynamo problem*. In this case, growing solutions of the magnetic field are calculated, but without considering the back reaction of the magnetic field on the flow due to the Lorentz force. This problem turns out to be linear in $\mathbf{B}$, since in the magnetic induction equation the velocity field $\mathbf{u}$ does not depend on $\mathbf{B}$, since it evolves independently. Stability analysis is used, by searching solution in the form

$$\mathbf{B} = \mathbf{B}_0(\mathbf{x})\mathrm{e}^{pt}, \tag{2.65}$$

where $|\mathbf{B}_0| \to 0$ as $|\mathbf{x}| \to \infty$. In general, there is an infinite set of eigenmodes $\mathbf{B}_0$ satisfying the induction equation, each eigenmode with an associated complex eigenvalue $p = \gamma' + \mathbf{i}\omega$, where γ' is the growth rate of the magnetic mode, and ω its frequency. If there are one (or more) modes with a nonzero growth rate, the flow triggers a dynamo. If ω is nonzero, the magnetic field propagates in the form of a dynamo wave. In the following, the variable γ will denote the growth rate of the magnetic energy (which is more easily obtained from the data of our numerical simulations), where $\gamma = 2\gamma'$. If the flow is periodic, the induction equation is a linear equation with periodic coefficients, whose solutions have the form of periodic functions multiplied by an exponential time dependence (Floquet solutions).

In dynamo theory, a fundamental quantity is the magnetic Reynolds number Rm (see Appendix A). This dimensionless number quantifies the importance of induction effects when compared to dissipation effects and it is defined – analogously to the fluid Reynolds number – as LU/η, where η is the magnetic diffusivity. For a given flow geometry that does not violate any anti-dynamo theorem (see below), the value of Rm discriminates whether dynamo action takes place or not. It can be shown that the mag-

netic Reynolds number needs to be larger than π in any case [29], a condition that is easily satisfied in laboratory dynamos. In natural or experimental dynamos, the kinematic growth of an initially infinitesimal magnetic field saturates when the Lorentz force becomes non negligible, hence affecting the flow in such a way that it no longer supports field growth (e.g., by reducing the magnitude of the velocity). In the following subsection, we will describe the role that the β term has in Eq. (2.62). We will show that this term acts against dynamo action, hence being one of the negative effects turbulence can have on the dynamo process.

β effect

In expanding the emf as a function of the mean magnetic field, a term proportional to the first derivative of $\overline{\mathbf{B}}$ has been considered as well, i.e., $\beta_{ijk}\partial\overline{B}_j/\partial x_k$. In the simplest situation, in which the turbulent velocity field is isotropic, β_{ijk} is in consequence also isotropic, and so

$$\beta_{ijk} = \beta\epsilon_{ijk}, \tag{2.66}$$

where β is a pure scalar. The expression of the emf hence takes hence the form

$$\mathcal{E} = \alpha\overline{\mathbf{B}} - \beta\nabla\times\overline{\mathbf{B}}.$$

These assumptions lead to a new version of the mean-field Ohm's law. In order to easily recognize the effect of the introduction of β, we assume that the medium has no mean motion; the mean field Ohm's law hence becomes

$$\bar{\mathbf{j}} = \sigma(\overline{\mathbf{E}} + \alpha\overline{\mathbf{B}} - \beta\nabla\times\overline{\mathbf{B}}), \tag{2.67}$$

and since $\nabla\times\overline{\mathbf{B}} = \mu_0\bar{\mathbf{j}}$, Equation (2.67) becomes

$$\bar{\mathbf{j}} = \sigma_T(\overline{\mathbf{E}} + \alpha\overline{\mathbf{B}}),$$

where the *turbulent conductivity* is defined as

$$\sigma_T = \frac{\sigma}{1+\mu_0\sigma\beta}.$$

It is possible to show that, under certain circumstances and in the high conductivity limit (for the details of the calculation, see [30]), one obtains the estimate

$$\beta \sim \frac{1}{3}U^2\tau_{cor},$$

where U is the root-mean-square velocity of the fluctuating field (i.e., $\sqrt{\overline{\mathbf{u}'^2}}$) and τ_{cor} is the correlation time of the fluctuation of the velocity field. This calculation shows also that the turbulent conductivity is smaller that the

molecular one (vice versa, for the turbulent resistivity η_T we have that $\eta_T = \eta(1 + \frac{1}{3}\mu_0 U^2 \tau_{cor}/\eta)$). As previously mentioned, a strong assumption has been made on the properties of the large scale fields in order to find the previous estimate of β. This assumption – whose consequences will be discussed below – says that the characteristic time and length scales of the fluctuations are small compared with those of the mean fields. This hypothesis limits, in principle, the range of validity of the previous result for β, especially within the framework of studies of the impact of large scale fluctuations on the dynamo action. In conclusion, MFT predicts that – under certain circumstances – the effective magnetic Reynolds number is reduced by a factor of σ_T/σ (as can be seen from the definition of Rm), creating a detrimental effect on the growth of the dynamo instability. A close examination of the detrimental effect of turbulence on dynamo action and the role of the β effect in the Madison Dynamo Experiment are ones of the main goal of the investigation described in this thesis.

Anti-dynamo theorems

Dynamo action cannot occur under particular circumstances, and this eventualities are proved by the so-called *anti-dynamo theorems*. We will not provide the proof of these theorems (which can be found in [29]) but we will just enunciate them here.

Theorem 1. *It is impossible to sustain a two-dimensional magnetic field by dynamo action. In Cartesian coordinates, a field independent of z that vanishes at infinity must ultimately decay.*

Theorem 2. *A planar velocity field $\mathbf{u} = (u_x(\mathbf{x}, t), u_y(\mathbf{x}, t), 0)$ cannot sustain dynamo action [31].*

Theorem 3: Cowling Theorem. *An axisymmetric magnetic field that vanishes at infinity cannot be maintained by dynamo action [2].*

Theorem 4. *A purely toroidal flow, i.e., a flow lacking radial motion in spherical coordinates, is not a dynamo [32].*

Cowling's theorem states that axisymmetric magnetic fields cannot be generated by flows that are symmetric about the same axis. Dynamo based on axisymmetric flows must hence generate a non-axisymmetric magnetic field, as the Dudley and James *s2t2* flow, thoroughly studied in this thesis. As can be noticed by this set of theorems, it is important that the degree of symmetry of the system is not too high in order that the dynamo instability can occur.

Anty-dynamo configurations are not the only obstacles to the dynamo process. Although the fluid topology and motion are dynamo-favorable, it can happen that turbulent motions of the fluid act against dynamo action.

The β effect (see above) is one of this negative mechanisms: The real magnetic Reynolds number is lower than the one calculated using the standard magnetic diffusivity of the material. Mechanisms of this kind can constitute a problem in designing a dynamo experiment, where the role of turbulence is not completely known *a priori* and simulations at high fluid Reynolds numbers are expensive. One of the goals of this work was to better understand whether and how those negative effects coming from turbulence have played a role in the Madison Dynamo Experiment. For this reason, next Subsection will deal with a general overview of turbulence, particularly focusing on one of the most important quantitative descriptions of turbulence: Kolmogorov theory.

2.4.4 Kolmogorov's theory of small scale turbulence

There is no rigorous mathematical definition of a turbulent flow. A turbulent motion of a fluid can be qualitatively described as an irregular and chaotic motion of the fluid, in opposition to a laminar state of the motion, which is deterministic and ordered. A crucial quantity in turbulence is the fluid Reynolds number Re, i.e., the ratio of inertia to viscous forces occurring in the fluid. This number can be equivalently defined as LU/ν, where L is the characteristic length of the system, U the amplitude of the characteristic velocity and ν the viscosity. It is an experimental fact that Re marks the transition from a laminar state to a turbulent state: High Re configurations are associated with high turbulent motions.

The reason why turbulence plays a fundamental role in liquid metal dynamo experiments is the following. The magnetic Prandtl number Pm (i.e., the ratio of the kinematic viscosity to the magnetic diffusivity, or Rm/Re) associated with liquid sodium (the most common liquid used in such experiments) is of the order of 10^{-5}. Since the goal of the experiments is to sustain a dynamo, the threshold of the dynamo instability should be overcome, i.e., the magnetic Reynolds number should be larger than a critical value Rm_c. In turn, Rm_c is typically of the order of 10^2, hence $Re = Rm/Pm$ is of the order of 10^7 for liquid sodium. Such a huge number testifies that is impossible to avoid the development of turbulence in the flow. Hence, characterizing the intermittent properties is a crucial ingredient in the understanding of dynamo action and eventually take measures in the laboratory that can facilitate the onset of the dynamo instability.

When turbulence comes into play, it is a good idea – in order to develop some physical intuition – to start from what can be now considered a milestone: the theory developed by Kolmogorov in 1941. The reason of the importance of this study is that this analysis provides some of the few theoretical results in this difficult field. A fundamental feature of this theory is *universality*: The analysis is very general and is based on the hypothesis of homogeneity, isotropy and scale invariance of the turbulence. From these

hypotheses, universal laws can be found that – according to this theory – should apply for every kind of flow (wake, jet, grid turbulence, boundary layer, etc.) and independent of the manner in which the turbulence is generated and maintained [33].

In 1941, A. N. Kolmogorov introduced a fluid turbulent theory in two seminal papers (see [34, 35]). The basis assumptions of this theory are: (i) when $Re \to \infty$, the energy dissipation rate ϵ remains constant; (ii) the energy flows from large scales (where the turbulence is produced via some large-scale forcing term) to small scales and this energy transfer mechanism is *scale independent*; when $Re \to \infty$, scale invariance is restored at least in statistical sense. Let us return to the second assumption. This description of the energy transfer mechanism from large to small scales is commonly called *energy cascade* in Fourier space. This concept is based on the picture of Lewis F. Richardson [36], who described turbulence as a hierarchy of interacting scales, where large scale vortices (created by some external forcing) decay due to nonlinear effects into smaller and smaller vortices and are finally dissipated by viscosity (Figure 2.1).

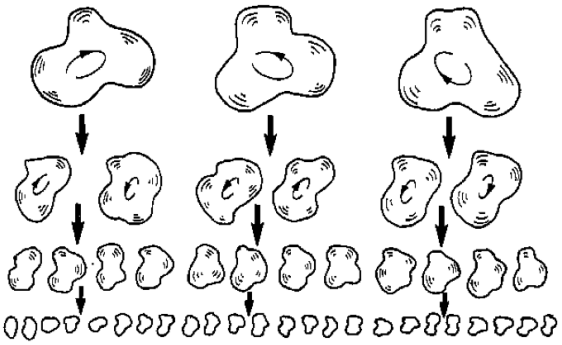

Figure 2.1: Richardson's picture of vortices disruption and energy transfer from large to small scales. Picture adapted form reference [33].

For $Re \gg 1$, an *inertial* range of spatial scales exists in which energy is transferred conservatively without being subjected to dissipation effects. This inertial range lays between the integral scale of motion L (i.e., the scale at which the energy is injected into the system) and the dissipation scale η (see next sections). In a quasi-stationary state, the rates at which energy is injected into the system, transferred towards smaller scales, and dissipated are (on average) identical. Under the assumption that the wavenumber k and the energy dissipation rate per unit mass ϵ are the only relevant dimensional quantities in the inertial range, the energy spectrum $E(k)$ of a turbulent flow field can be derived by using simple dimensional analysis, leading to

$$E(k) \propto \epsilon^{2/3} k^{-5/3}.$$

The spectrum has the form of a power law which reflects the assumed self-similarity of the scale-dependent distribution of energy in the inertial range. Below the dissipation scale η, viscous dissipation dominates by converting kinetic energy of the eddies into molecular heat.

Another important result, which is strictly connected to Equation (2.4.4), regards the so called third-order longitudinal structure function of the flow, defined as

$$\langle (\delta v_L)^3 \rangle \equiv \left\langle \left| \Big(\mathbf{u}(\mathbf{x}+\mathbf{r}) - \mathbf{u}(\mathbf{x}) \Big) \cdot \frac{\mathbf{r}}{r} \right|^3 \right\rangle, \tag{2.68}$$

where $\mathbf{u}$ represents the velocity field, $\mathbf{x}+\mathbf{r}$ and $\mathbf{x}$ are the positions of the two considered points (therefore $\mathbf{r}$ represents their *separation*), and $\langle \cdot \rangle$ denotes some suitable averaging process (ensemble average, time average, etc). Kolmogorov predicts that

$$\langle (\delta v_L)^3 \rangle = -\frac{4}{5} r \epsilon \tag{2.69}$$

in the inertial range, i.e., at scales where self-similarity is not broken by boundary conditions or forcing mechanism (large scales) or molecular dissipation (small scales). This result is known as the *4/5 law*. This is one of the few exact analytical results in 3D fluid turbulence.

The first argument against the validity of the self-similarity hypothesis of turbulence (therefore concerning the presence of intermittency) was given by Landau. He stated that the quantity ϵ, crucial in Kolmogorov's analysis, could be a random function of position and time. In other words, the value of ϵ is not constant in time but rather it is the energy dissipation at the considered temporal instant and it is not uniform in space, i.e., it is the averaged value over the small region of size r in which the functions $S_p(\mathbf{x}, \mathbf{r}) \equiv \left\langle \left| \Big(\mathbf{u}(\mathbf{x}+\mathbf{r}) - \mathbf{u}(\mathbf{x}) \Big) \cdot \frac{\mathbf{r}}{r} \right|^p \right\rangle$ – as in Eq. (2.68) – are evaluated (see discussion in [33]). This assumptions lead to different result and Kolmogorov's predictions become inaccurate: the functions $S_p(\mathbf{x}, \mathbf{r})$, also known as *structure functions* of the velocity field – show a different scaling behavior. Although Landau accepted that the functional dependence of a structure function on r and ϵ can be universal, the quantity ϵ can however depend on the type of flow considered, especially on the large-scale motion of the particular flow. This idea is supported by the observation (G.I. Taylor in 1917 and Landau in 1941) that the spatial distribution of the vorticity $\omega = \nabla \times \mathbf{u}$ (thus, of the dissipation rate, since the two quantities are correlated) can be very spotty, leading to the phenomenon known as *intermittency*, i.e., a strong spatial inhomogeneity of the energy transfer mechanism from large to small scale eddies (see Figure 2.2 and compare it with the non-intermittent case in Figure 2.1). In other words, intermittency is caused by the vortex stretching and thinning mechanism, which leads in turn to the formation of

coherent structures of vortex filaments of high vorticity and low dissipation.

Intermittency in turbulent systems is often detected and characterized by studying the statistical properties of the *velocity increments* $\mathbf{u}(\mathbf{x}+\mathbf{r},t)-\mathbf{u}(\mathbf{x},t)$ (as in Eq. (2.68)) or of the two-point correlation function $\langle \mathbf{u}(\mathbf{x}+\mathbf{r},t)\mathbf{u}(\mathbf{x},t)\rangle$ and then studying the scaling properties of those functions and their possible departure from the predictions coming from the self-similarity hypothesis of the energy cascade mechanism.

Indeed, at high Reynolds numbers, it can be shown – for instance – that the function $\langle(\delta v_L)^p\rangle$, $p \in \mathbb{N}$ (see Eq. 2.68), have an r^{ζ_p} scaling [37, 38], and the results of experiments and numerical simulations show that the scaling exponents $\zeta(p)$ of the p^{th}-order structure function deviate from the scale-invariant exponent predicted by Kolmogorov. This departure is commonly referred to as *anomalous scaling*, and it is a consequence of the presence of intermittency.

In other words, the analysis of the $\zeta(p)$ exponents can reveal how much the spatial distribution of the energy dissipation is clumpy. The reason of this last statement can be qualitatively grasped by the following picture. If the decay of the vortices occurs in such a way that the vortices are teased out into finer vortices, the vorticity field becomes spotty, as well as the *enstrophy* scalar field, where the enstrophy is just defined as the squared modulus of the vorticity. Since it can be shown that the energy dissipation is proportional to the enstrophy (the proportionality factor being the viscosity of the medium), then the spatial distribution of the energy dissipation ϵ will have the same degree of spottiness, and ϵ will be concentrated only into regions where high the vorticity is high (e.g., thin vortex tubes and surfaces). Since it can be shown [33] that the exponents of the velocity increment functions are correlated with the degree of spottiness of the small-scale structure of the fluid, it is then easy to understand that those functions are a reasonable choice for measuring spatially intermittent turbulent behaviors.

In MHD, the role of turbulence becomes even more complicated, since the magnetic field is a source of local symmetry breaking and a source of momentum (via the Lorentz force) which is – in turn – coupled with the velocity field. One of the first attempts to formulate a homogeneous and isotropic turbulence theory à la Kolmogorov has been proposed by by Kraichnan [39] and Iroshnikov [40], who used arguments similar to Kolmogorov's ones but considered the correction to the energy transfer due to the presence of a mean magnetic field. With this analogous analysis, they predicted the following scaling law for the so-called Elsässer fields $\mathbf{u} \pm \frac{\mathbf{B}}{\sqrt{\mu\rho}}$:

$$\zeta(p) = \frac{p}{4}. \tag{2.70}$$

Many experiments and numerical studies have confirmed that these predictions (both for fluid and MHD systems) should be slightly modified because

of the effect of a *strong* intermittent behavior of the energy dissipation (see [41–49]), giving rise to formulations of models for the $\zeta(p)$ function (see [50–53]). The most important work that completes and and extends all these results is the classical Goldreich-Sridhar theory [54, 55], where the important role of anisotropy has been extensively studied. Pedagogical introductions to MHD turbulence can be found, e.g., in [56] and [57].

So far, we briefly reviewed the theoretical background which concerns the theory of homogeneous and isotropic turbulence. However, the reality is more complicated. Real turbulent flows have nontrivial boundary conditions and forcing mechanisms, so they have always a degree of inhomogeneity and anisotropy. For these flows, analyzing the data can be very challenging because the choice of the location where the measurements are taken can be crucial, while – in the case of the homogeneous and isotropic system – single point measurements (velocity increments, turbulence intensity, time traces, fluctuation spectra) can quantitatively provide enough information about the turbulence. In order to overcome the issues that inhomogeneous and anisotropic systems introduce, different strategies have been used by the scientific community in experiments or simulations. Simulations of inhomogeneous and anisotropic turbulence have usually the possibility to explore the whole information about the system, and so they have usually focused on global, averaged quantities (energy, helicity, enstrophy) over the whole volume (a detailed discussion can be found in [58]). Another source of anisotropy is the introduction of a large scale superimposed magnetic

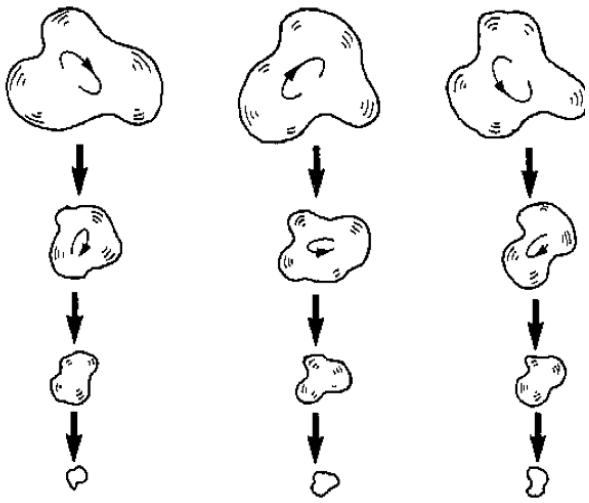

Figure 2.2: Richardson's picture of vortices disruption and energy transfer from large to small scales with strong spatially inhomogeneities: The cascade is not space filling any more (compare Figure 2.1) and the system shows intermittent behaviors. Picture adapted form reference [33].

field which is able to influence the flow (i.e., for flows with a non-negligible conductivity, like liquid metals or plasmas): the magnetic field breaks the isotropy even further and the MHD formalism should be taken into account (when the system fulfill the right conditions in order to be described by MHD).

On of the systems we studied numerically for this dissertation, namely the Madison Dynamo Experiment, is neither homogeneous nor isotropic: It is bounded, the forcing mechanism is localized and has an axis of symmetry, a dipole magnetic field can be superimposed. In order to quantify the turbulent character of this system, we make use of the structure functions and their scaling laws, trying to find out whether the sources of anisotropy and inhomogeneity have a non-negligible impact on the results. A long term goal, for instance, could be whether our result can help to more easily understand in future how (much) intermittency can affect the dynamo mechanism. We emphasize that this kind of investigation is very different from what numerical investigations usually study, since they usually make use of periodic boxes simulations and non-localized forcing mechanisms (typically the forcing term acts in the spectral space at large scales). The realism of the numerical system and the forcing mechanism is the strength of this work.

Chapter 3

Experiments

The aim of this chapter is to provide the reader with a description of the two liquid metal experiments we numerically modeled for this dissertation. As already mentioned in Chapter 2, the two experiments are: the Princeton Plasma Physics Laboratory Magnetorotational Instability experiment, a cylindrical apparatus filled with liquid gallium and forced by rotating walls intended to create the Magnetorotational instability at laboratory scales, and the Madison Dynamo Experiment, a spherical vessel filled with liquid sodium and stirred by two counter-rotating propellors, designed in order to observe dynamo action in a simple geometry and without using high permeability materials.

Contents

3.1 The Princeton Magnetorotational Instability experiment 37
3.1.1 Hydrodynamics of the experiment 38
3.1.2 The effect of the superimposed magnetic field . . . 42
3.2 The Madison Dynamo Experiment 46
3.2.1 First comparisons between simulations and experiments 48
3.3 Summary 49

3.1 The Princeton Magnetorotational Instability experiment

As pointed out in [59], although the existence and importance of the MRI are now well accepted by most astrophysicists, clear experimental demonstrations of this instability are still missing. The technical challenge in designing a liquid metal MRI apparatus can be realized by calculating the fluid and magnetic Reynolds numbers available in laboratories: $Re \sim 10^7$

and $Rm \sim 20$. This last number is small and it can turn out to be not high enough in order to trigger the instability, which occurs if the rotation period and the Alfvén crossing time are shorter than the timescale of magnetic diffusion [59]. As explained in section 2.4.2, this last statement is translated into the conditions $Rm \gtrapprox 1$ and $S \sim 4$, where S is the Lundquist number. The Princeton Plasma Physics Laboratory (PPPL) apparatus has been designed in order to achieve the MRI in laboratory. It uses liquid gallium in a cavity between two concentric and rotating cylinders, in order to create a Taylor-Couette flow (see section 3.1.1). Internal velocity measurements are performed with Ultrasound Doppler Velocimetry.

3.1.1 Hydrodynamics of the experiment

The Taylor-Couette apparatus of the Princeton Plasma Physics Laboratory consists of a rotating fluid of height $h = 27.86$ cm is confined between two concentric cylinders of radii $R_1 = 7.06$ cm and $R_2 = 20.30$ cm, each one rotating – respectively – with angular velocities Ω_1 and Ω_2 [6]. Unlike conventional Taylor-Couette experiments, this apparatus is characterized by an important feature: The possibility of partially controlling secondary circulation that appears in the fluid, caused by the finite size of the cylinder (since – theoretically – a perfect Taylor-Couette flow can take place only in infinitely long cylinders). This control is realized by dividing each endcap into two independently driven rings, where opposing rings at top and bottom are driven at the same adjustable angular velocities Ω_3 (inner rings) and Ω_4 (outer rings). Secondary circulation is usually minimized by building apparatuses with larger aspect ratios $\Gamma = h/(R_2 - R_1)$, but experimental investigations [60, 61] at relatively high values of Γ showed that end effects are still significant if the endcaps co-rotated with one of the cylinders. If Ω_3 and Ω_4 are carefully chosen, secondary circulation is reduced and ideal Couette profiles are well approximated. A schematic view of the apparatus is shown in Fig. 3.2.

The Taylor-Couette flow

The Taylor-Couette flow [62, 63] describes the flow of a fluid between two concentric and differentially rotating cylinders. The resulting flow shows a very rich dynamics, depending on the parameter range where it is run. Up to 26 different stable flow can be produced for a constant Reynolds number [64]. In particular, this flow is studied in the so-called *narrow gap* limit, i.e., when the aspect ratio of the cylinders is relatively high (or even infinite). In this regime, the steady state laminar solution to the hydrodynamical problem [62] is

$$\Omega(r) = A + \frac{B}{r^2}, \tag{3.1}$$

where $A = (\Omega_2 r_2^2 - \Omega_1 R_1^2)/(R_2^2 - R_1^2)$, $B = R_1^2 R_2^2(\Omega_1 - \Omega_2 R_1^2)/(R_2^2 - R_1^2)$, and the subscripts 1 and 2 refer to the inner and outer cylinders, respectively.

The Princeton MRI experiment cannot be considered to be in the narrow gap regime, since an aspect ratio of 2.11 is far from being close to infinity. The boundary conditions, i.e., effects of the end caps play an important role [65,66] and these secondary flows due to the finite size of the experiment have been recently studied, and several possible solutions in order to minimize those boundary effects have been proposed [66–68].

The hydrodynamical stability of this flow has been studied in 1916 by Rayleigh [69], who discovered an inviscid stability criterion for the Taylor-Couette problem, which plays an important role for the stability of astrophysical systems whose configuration is similar to a Taylor-Couette problem. *Rayleigh's stability criterion* states that an inviscid Couette flow is stable if the specific angular momentum $r^2\Omega$ decreases outwards, i.e.,

$$\frac{\partial (r^2\Omega)^2}{\partial r} > 0. \tag{3.2}$$

Taylor extended this result by considering also the viscous regime (see [17] for a didactical introduction to the problem). According to this criterion, the narrow gap Taylor-Couette profile is stable if $(\Omega_1 R_1^2)^2 < (\Omega_2 R_2^2)^2$, i.e., $AB > 0$ [59].

If the flow is electrically conducting and immersed in a magnetic field, the scenario changes drastically, and the stability criterion has to be replaced by the condition already discussed in section 2.4.2.

The Ekman circulation

As stated above, secondary motions of the flow are important in systems with realistic aspect ratios, since they can influence the bulk flow. The most important effect of the end caps in Taylor-Couette flows is the so called *Ekman circulation*. Depending on the rotation rate of the cylinders, this circulation can result in a boundary layer poloidally inflowing or outflowing in the bulk volume. In order to understand this mechanism, let us consider an infinite cylinder. For translational symmetry reasons, the steady state solution would have the same angular velocity profile $\Omega(r)$ independently of the vertical coordinate z (Taylor-Proudman theorem, see Appendix B), and the profile would assure that the pressure gradient compensates exactly the centrifugal force in order to keep the flow stationary (and this would in turn result in the Taylor-Couette flow profile).

In a finite cylinder, the no-slip boundary conditions on the end caps change the scenario, since an infinitesimally thin fluid layer next to the solid impermeable physical boundary stays attached to the boundary because of attractive forces between the wall's and the fluid's molecules [19], hence the boundaries approximately follow a rigid body rotation within the boundary

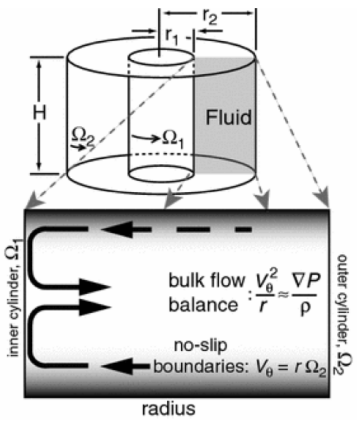

Figure 3.1: *Left*: A cartoon showing the Ekman cell in the Princeton geometry. The source of the poloidal circulation is a consequence of the rigid body rotation near the boundaries and the imbalance of the pressure gradient. Picture taken from [70], with kind permission from Springer Science and Business Media.

layer, e.g. $u_\theta = r\Omega_{wall}$, which results in a different angular velocity profile. In other words, the effective pressure close to the boundaries cannot be balanced by centrifugal forces and, in consequence, this uncompensated pressure gradient induces a poloidal flow that recirculates into the bulk volume and changes it. This motion is the Ekman circulation. This poloidal flow follows the cylinder walls and eventually converge at the mid-plane where it forms a radial outward or inward jet. This creates a large scale poloidal flow cell which is called *Ekman cell* (see Figure 3.1). This Ekman circulation distorts the analytical Couette profile, transporting angular momentum efficiently throughout the whole bulk volume, hence reducing the free energy available to the Magnetorotational instability. Moreover, at high Reynolds numbers (> 400), it introduces hydrodynamic fluctuations that complicates the identification of MRI modes [66]. From these considerations, it becomes clear that the Ekman circulation must be suppressed or at least minimized in order to trigger and identify the MRI more easily.

Stewartson layers

Stewartson [71] studied theoretically the flow of a fluid contained in a rapidly rotating cylinder whose endcaps were differentially rotating with respect to the cylinder (as in the Princeton experiment). As the Taylor-Proudman theorem suggests (see Appendix B), motions within the bulk fluid that are slow with respect to timescale associated with Ω become independent of z, result that also Stewartson found in this configuration: the velocity discontinuity of the boundary due to the splitting of the endcaps propagated vertically into the bulk flow, creating the so-called Stewartson layer. At large differential rotation the Stewartson layer becomes unstable to non-exisymmetric Kelvin-Helmoltz-like instabilities [72], as shown numerically also in [25]. The formation of Stewartson layers is considered to be detrimental for the onset

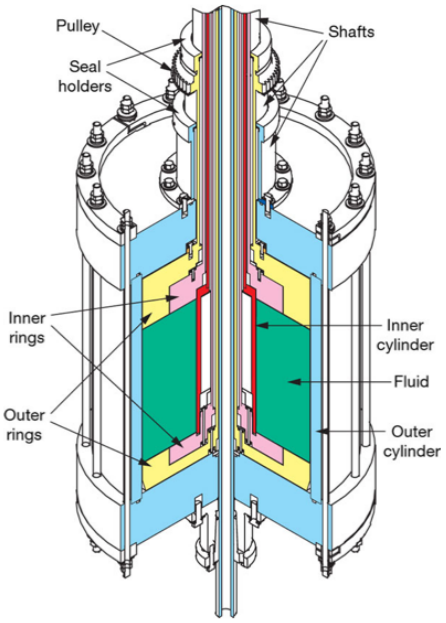

Figure 3.2: *Left*: A cartoon representing the experimental set-up of the Princeton MRI experiment. The conducting fluid region (green in the picture) is filled with liquid gallium. Picture taken from [6], reprinted by permission from Macmillan Publishers Ltd.

of the Magnetorotational Instability, as shown in [73], since this propagating discontinuity would influence the azimuthal velocity profiles in such a way that the MRI is suppressed, becoming – moreover – more difficult to be experimentally observed.

Minimization of the Ekman circulation

In order to reduce the Ekman circulation, more than one method have been proposed and analyzed in past studies [66–68]. In the light of those results, a Taylor-Couette device with two intermediate independently driven endcaps has been designed [70], and it is illustrated in Figures 3.2 and 3.3.

With this approach the condition that the boundary layer rigidly rotates is broken: instead of having $u_\theta = \Omega_{wall} r$ for $R_1 < r < R_2$, the no-slip boundary condition would impose that $u_\theta = \Omega_3 r$ if $R_1 < r < R_{split}$ and $u_\theta = \Omega_4 r$ when $R_{split} < r < R_2$, where R_{split} is the radial location of the split in the end caps. This approach does not guarantee that the Ekman circulation is suppressed, but choosing two independent endcaps is a good compromise between engineering difficulties and control on the flow profile [59].

It has been experimentally shown that this splitting of the end caps is effective, since a flow profile similar to the analytical Taylor-Couette solution can be measured, namely reducing the Ekman circulation [70].

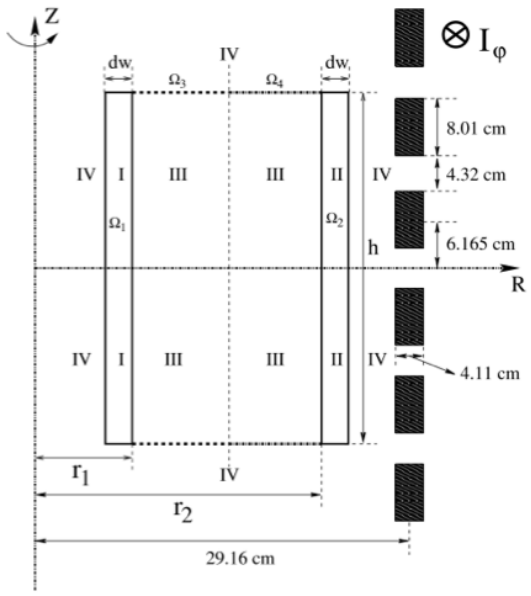

Figure 3.3: *Left*: Another schematic view of the MRI Experiment, showing in detail the geometry. The radius of the inner cylinder R_1 is 7.1 cm, that of the outer cylinder R_2 is 20.3 cm. The height h of the cylinder is 27.9 cm, hence the aspect ratio of the cavity of the experiment is $h/(R_2-R_1) = 2.11$. The rotation speeds of the cylinders are indicated with Ω_1 and Ω_2, respectively, whereas the rotation speeds of the endcaps are denoted – respectively – as Ω_3 and Ω_4 for the inner and outer endcap.

3.1.2 The effect of the superimposed magnetic field

As already explained in Chapter 2, the background magnetic field has to have the right amplitude in order to trigger the MRI instability: too strong or too weak fields lead the system in the stable regime, as Figure 3.4 shows. The results displayed in this picture show the stability and instability regions of the relevant parameter space (magnetic Reynolds number *Rm vs* Lundquist number S) of the MRI experiment, which can operate only in the portion of the parameter space in the dashed line box. The black curve shows the marginal stability curve above which the MRI takes place when only axisymmetric modes are taken into account. if non-axisymmetric simulations are performed, the marginal stability curve changes (red curve in the picture). The results displayed in Fig. 3.4 have been obtained using the code `Heracles` [74].

Self-similarity of the azimuthal velocity profiles

Previous simulations [25] of the effect of the MRI modes to the velocity fields suggest the MRI will cause a change in the azimuthal velocity of 2%. The experiment is supposed to reveal the presence of the MRI by measuring this distortion of the flow. This task is however far from being easy, since a change of 2% is rather small and can be at the limit of what is currently measurable with the Ultrasound Doppler Velocimetry diagnostic. Moreover, this small MRI amplitude is difficult to be disentangled from other instabilities. In other words, since the MRI modes saturate at a rather amplitude, slow drifts in the flow whose amplitude is comparable to the

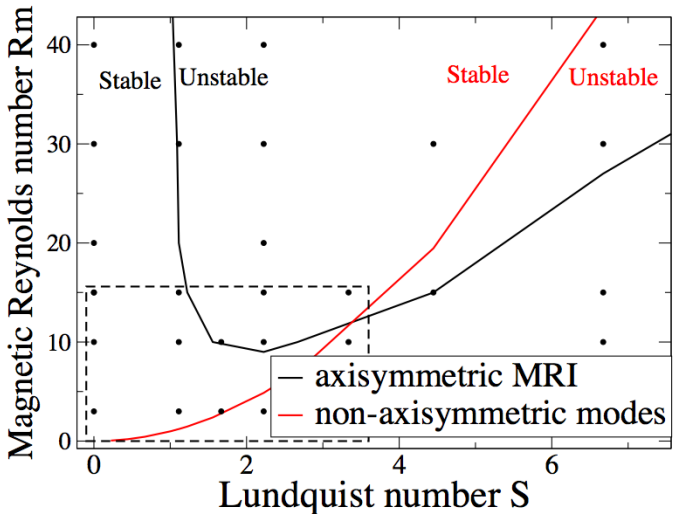

Figure 3.4: Stability and instability regions of the relevant parameter space (magnetic Reynolds number Rm *vs* Lundquist number S) of the MRI experiment. The black curve shows the marginal stability curve above which the MRI takes place. The red curve is the marginal stability curve of non-axisymmetric modes generated by Kelvin-Helmoltz instability of the Stewartson layer. The two curves have been obtained by interpolating results from – respectively – 2D and 3D simulations. The dashed square box represents the portion of the parameter space that is accessible to the experiment. Picture reprinted with permission from [90], Copyright 2012, AIP Publishing LLC.

expected effect of MRI make the identification of the MRI difficult. As described in [75] , a new way to spot the presence of the MRI has been proposed. As Fig. 5.4, the azimuthal velocity drops constantly for a given amplitude of B, and this drop is independent of the rotation rates of the walls. If the same data are plotted after rescaling the coordinate axes, an interesting self-similar behavior emerges. Fig. 3.6 shows this rescaling: The azimuthal velocity is rescaled by v_1 (the linear velocity of the inner cylinder, $\Omega_1 R_1$) and the magnetic field is transformed into its associated Alfvén velocity and then rescaled by v_1. By doing that, the data tend to collapse onto a single curve. The hypothesis is that a strong MRI mode is strong enough to modify this behavior and the departure from this collapse could be a robust MRI signature. In order to prove this hypothesis, it is crucial to study and understand the behavior of the system with and without the MRI, i.e., if (and how) the systems change this self-similar behavior of the curves u_θ/u_1 *vs* u_A/u_1. In the legends of these two pictures, "MRI-Z" refers to the setting $\{\Omega_2, \Omega_3, \Omega_4\} = \{0.55 \cdot \Omega_1, 0.1325 \cdot \Omega_1, 0.1325 \cdot \Omega_1\}$ used in the experiment to produce the plotted data whereas the percentages refer to the values $(\Omega_1/\Omega_{max}) \times 100$, where Ω_{max} is the maximum inner cylinder design speed, i.e., 4000 rpm. In the experiment, Re is increased by changing the speeds of the whole set of Ω_i proportionally.

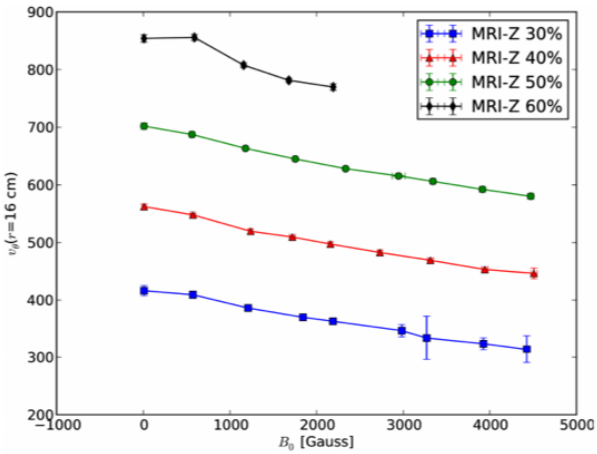

Figure 3.5: Azimuthal velocity drops constantly for a given amplitude of B, independent of Ω. In this (and the following picture), "MRI-Z" refers to the setting $\{\Omega_2, \Omega_3, \Omega_4\} = \{0.55 \cdot \Omega_1, 0.1325 \cdot \Omega_1, 0.1325 \cdot \Omega_1\}$; the percentages to the values $(\Omega_1/\Omega_{max}) \times 100$, where Ω_{max} is the maximum inner cylinder design speed, i.e., 4000 rpm. Picture from the PhD thesis [75].

Open questions, need of simulations, future plans

According to the location of the linear instability region in the parameter space, the experiment has reached the MRI, since the rotation rate of the cylinders and the field strength are sufficiently high. Nevertheless, other MHD instabilities are seen, but not yet the MRI, probably because the non-linear saturated MRI amplitude is small, as already explained in the previous section. Since an investigation of the effect of the magnetic field on the flow in the absence of the MRI is needed, simulations can turn out to be the right laboratory to perform this task. In particular, it would be important to perform simulations with fixed Pm (since in the experiment the working medium is always liquid gallium), varying Re (and Rm correspondingly) and B. The first natural questions are: Can numerical simulations predict the collapse of the data showed in Figs. 3.5-3.6? Moreover, can they provide a detailed description of the effect of the MRI? How does that effect differ from flow modification by the magnetic field *in the absence* of the MRI? Finally, simulations can investigate, in the future, which kind of modifications of the apparatus can lead to a higher saturated value of the MRI. In order to increase the MRI amplitude and make it more distinct from the residual Ekman circulation, some modifications of the experiment have been proposed, such as different settings of the rotation speeds, or a $\mathbf{j} \times \mathbf{B}$ body force to supplement viscous reinforcement of the sheared rotation profile since it may drive the mean flow more efficiently than viscous torques, and could result in a larger saturated amplitude of the MRI eigenmode, potentially leading to a larger u_r that may be measurable [75].

The PPPL MRI experiment is promisingly going to reveal details of

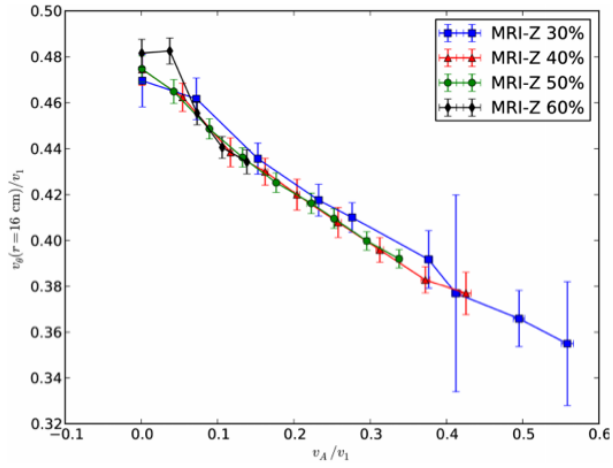

Figure 3.6: Normalized velocity v_θ/v_1 constant for normalized applied field v_A/v_1, where v_A is the Alfvén speed associated to the magnetic field B. See also caption of Fig. 3.5. Picture from the PhD thesis [75].

this powerful instability, yet it will not answer questions dealing with the generation of the pre-existent magnetic field which triggers the instability: We remind that for the MRI to occur, a background axial magnetic field must be present. Concerning the generation of magnetic fields in conducting fluids, dynamo theory comes into play. In the following, we describe one of the first attempts to recreate this generation process in a simple-connected geometry. Moreover, differently from other experiments, the geometry of the system is spherical with an axisymmetric drive mechanism, and this particular configuration is of more fundamental interest in astrophysics than previously explored ones.

3.2 The Madison Dynamo Experiment

The Madison Dynamo Experiment (MDE) consists of a spherical vessel (radius of 0.533 m) of stainless steel containing liquid sodium, investigating processes related to naturally occurring dynamos and addressing a fundamental tenet of turbulent dynamo theory. The flow is stirred by two counter-rotating impellers of 30.5 cm diameter that enter the sphere through each pole (a cutaway view of the experiment can be found – for instance – in [76]), having a topology similar to the Von Kármán Sodium experiment [77–79]. The impellers thrust fluid outwards to the poles. In each hemisphere, the mean flow streams along the walls to the equatorial plane, where it rolls back in towards the center of the sphere (Fig. 3.8), creating a so-called *s2t2* flow, as studied by Dudley and James in [80]. In addition to this poloidal circulation, the two flow cells counter-rotate in toroidal direction, as imposed by the sense of rotation of the propellers. Driving is provided by two 75 kW motors. The radial component of the magnetic field is measured by an array of temperature-compensated Hall probes mounted to the sphere's surface. Magnetic fields within the sphere are measured by linear arrays of Hall probes inserted into the sodium within stainless steel sheaths. Finally, two external electromagnets, in a Helmoltz configuration coaxial with the impellers, apply a nearly uniform magnetic field throughout the sphere, and this magnetic field is used to help the onset of the instability. The Madison dynamo experiment is directly inspired by the work of Dudley & James, who performed numerical kinematic dynamo studies and found this particular two-cell flow geometry to be among the most efficient simple spherical dynamos. They showed that this flow minimizes the threshold Rm_c of the dynamo instability.

The experiment achieves a magnetic Reynolds number of $Rm \sim 100$ which implies a Reynolds number of $Re = \mathcal{O}(10^7)$ due to the fixed small magnetic Prandtl number $Pm = Rm/Re = \mathcal{O}(10^{-5})$ of liquid sodium. The current experimental setup, however, does not reach the dynamo threshold due to detrimental effects of turbulence, its critical magnetic Reynolds

number Rm_c being larger than ~ 100 by some unknown factor.

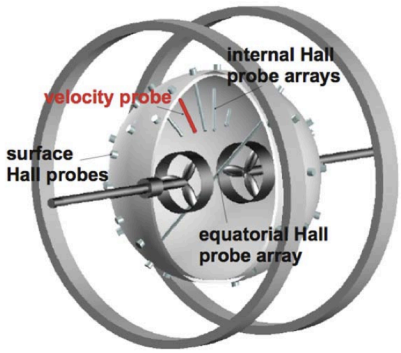

Figure 3.7: A cutaway view of the MDE. The impellers, external field coils, surface, and internal Hall probes are shown. Figure courtesy of K. Rahbarnia.

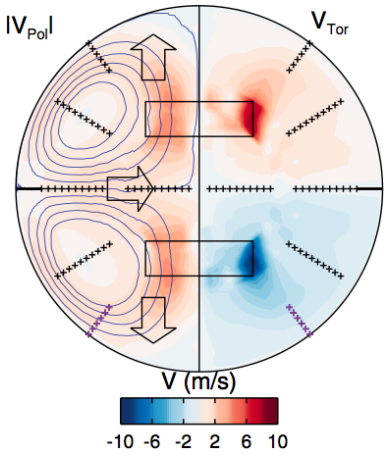

Figure 3.8: An example of the mean flow of the MDE (cross section, yz-plane) computed using FLUENT®. The hollow black boxes represent the impellers. The internal probe array is indicated by the black and purple crosses. "Reprinted figure with permission from [81].

The MDE has not achieved self-excitation of dynamo action. The reason why dynamo does not take place probably lies in the fact that turbulence has a detrimental effect on the dynamo process and this influence were underestimated during the design process of the device, since preliminary calculations were restricted to linear studies of stationary axisymmetric flows, yielding a critical magnetic Reynolds number of $Rm_c \simeq 50$ [82]. The MDE has nevertheless measured and quantified interesting features, summarized in the following. The omega effect (i.e., the conversion of poloidal to toroidal field due to differential rotation) has been observed experimentally [83]. Moreover, an induced magnetic dipole moment parallel to the axis of symmetry was measured. This dipole, according to Cowling's antidynamo theorem, could not be generated by the axisymmetric mean flow and its presence is very likely due to the effect of a turbulent electromotive force (see next subsection, [76, 84]. The magnetic field generated by these fluctuation driven currents was found to be oriented opposite to the dominant poloidal and toroidal magnetic fields in the experiment. Therefore, the effect was termed turbulent diamagnetism [85]. Furthermore, an intermittently growing transverse magnetic field was measured [86]. Further details on the experimental results, the numerical simulations and its modelization can be found in three PhD theses [87–89].

3.2.1 First comparisons between simulations and experiments

In this Section, we briefly describe the comparisons between the simulations and the Madison experiment.

Spectra

Figures 3.9 and 3.10 show a comparison between experimental and simulated spectra, in order to emphasize the potentialities of the `DYNAMO` code in predicting experimental data. The spectra in these figures are frequency spectra obtained by Fourier transforming the time traces of the velocity and the magnetic field components at a specific point. In the case in point, we are dealing with measurements taken at $r = 0.4$ m, $\theta = 121°$, $\phi = 0$. The applied dipole has a magnitude of 53 Gauss, and the magnetic Reynolds number – according to the definition used for the MDE – is about 160. The simulated data are taken at the same coordinates from run 6 ($Rm = 40$). It is worth noticing that – for practical purposes – the Reynolds numbers (both fluid and magnetic) mentioned by the experimentalists are defined using the speed of the tip of the impeller blades as an estimation of the typical velocity amplitude U. The resulting Reynolds numbers are expected to be larger than the ones obtained with the convention we are using, i.e., taking the root-mean-square velocity as U. It should not surprise, hence, that the Reynolds numbers do not correspond exactly in the comparison. Run 6 has an applied field whose dimensionless amplitude is $B_{ext} = \sqrt{\frac{3}{4\pi}}\mathcal{C}$, where $\mathcal{C} = 0.07$. In order to convert the dimensionless amplitude in physical meaning units, one can use the procedure explained in Appendix A. Taking into account the root-mean-square velocity U of run 6, the value of $\mathcal{C}$, and the velocity of the impeller tips needed to have a magnetic Reynolds number of about 20, the estimation of B_{ext} turns out to be about 20 G. We report that the experimental data were obtained by making use of both the equatorial baffle and of "rotational" baffles (out of the equatorial plane). The latter were recently introduced in order to control the ratio of the poloidal to the toroidal component of the velocity field.

This spectra comparison show that, although the simulated system and the experimental one have still different fluid Reynolds number, the statistics of the fluctuations of the magnetic field in particular are similar, result that is also confirmed when the turbulent emf is measured, as explained in the next paragraph.

Direct observation of the turbulent emf

A recent experimental results dealing with the effect of turbulence on the MDE has been published in [84]. For the first time, a direct measurement of the transport of a vector magnetic field by turbulence has been achieved.

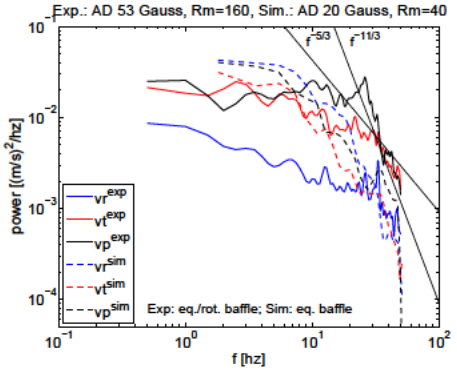

Figure 3.9: Comparison between the experimental and simulated velocity spectrum. Figure courtesy of K. Rahbarnia (personal communication).

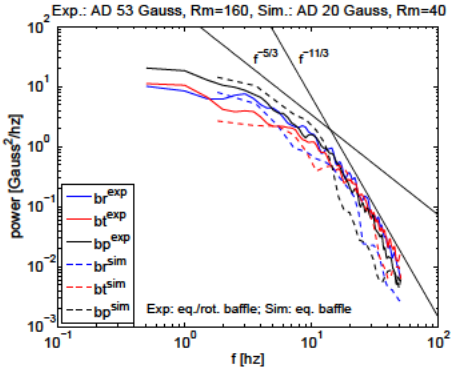

Figure 3.10: Comparison between the experimental and simulated velocity spectrum. Figure courtesy of K. Rahbarnia (personal communication).

In a direct analogy with direct measurements of the turbulent Reynolds stress (turbulent viscosity) that governs momentum transport, a non-zero turbulent electromotive force (i.e., the force generated by the coherent interaction between fluctuations of $\mathbf{u}$ and $\mathbf{B}$, see definition, Eq. (2.61)) has been directly measured by simultaneously registering the three components of velocity and magnetic fields, and computed the correlations that lead to mean-field current generation. Furthermore, this turbulent EMF tends to oppose and cancel out the local current, acting to increase the effective resistivity of the medium, which is equivalent to the effect produced by an enhanced eddy diffusivity for magnetic flux. The same experimental results can be found by the simulations we carried out, considering that the fluid Reynolds number of the simulations (Re $\simeq$ 2000) is several orders of magnitude lower compared to the MDE's one (Re $\sim 10^7$). In other words, measurement and numerical simulation clearly show an anti-alignment of the turbulent emf with the local current, i.e., the turbulent emf is dominated by the β effect term in the kinematic regime considered (see Eq. (2.4.3) and Figure 3.11).

3.3 Summary

In this Chapter, we briefly described the most important features of the two liquid-metal experiments with which our work deals. The Princeton Plasma Physics Laboratory experiment was designed for creating a quasi-Keplerian rotation in a liquid Gallium (whose Prandtl number is $\sim 10^{-6}$) cylindrical device, stirred by a viscous boundary force. Aim of this experiment is the first demonstration of the magnetorotational instability in such a configura-

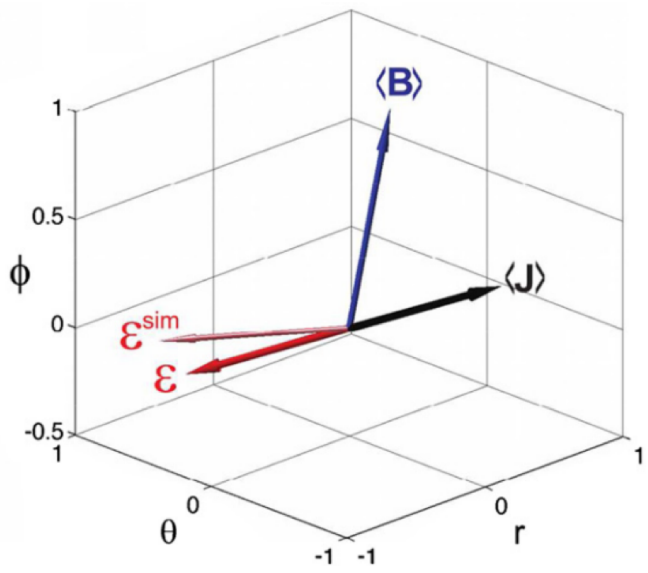

Figure 3.11: Three-dimensional view of the unit vectors $\mathcal{E}$ (red), **J** (black), **B** (blue), and the results of a fully turbulent numerical simulation $\mathcal{E}_{sim}$. The emf vector tends to cancel out the mean current density, making the magnetic field generation more difficult. Reprinted figure with permission from [84].

tion. The second experiment, the Madison Dynamo, consists of a spherical vessel in which liquid sodium (Prandtl number $\sim 10^{-5}$) is stirred by two counterrotating impellers. Goal of the device is the generation of a magnetic field (or the amplification of the pre-existing background applied one) by exciting the so-called dynamo instability. Both experiments have not yet reached the target. In the MRI experiment it is hard to prove that the instability is occurring with the current set-up, since the MRI causes changes in the fluid motion whose amplitude is comparable with the experimental uncertainties. Moreover, other (magneto)hydrodynamical instabilities with the same effect on the fluid appear and make the MRI less distinguishable. In the dynamo experiment, it turned out that it is hard to overcome the instability threshold because of the detrimental effects of turbulence on the dynamo process, which were underestimated during the design process, since time-dependent MHD simulations of the turbulent flow had not been performed at that time.

All these difficulties urge the use of numerical simulations, and the following Chapters will deal with the numerical modeling of the two experiments and the results of this investigation.

Chapter 4

Numerical approach

> "Any given program, when running, is obsolete".
>
> Edward A. Murphy

As pointed out in the previous Chapter, time-dependent numerical simulations of the two instabilities may constitute a valuable tool in support of the experimental efforts. For this purpose, two MHD codes have been used in order to tackle the difficulties encountered in the experiments (described in Chapter 3). `SFEMaNS` has been developed in order to solve the MHD equations in axisymmetric geometry. Since it can handle magnetic field boundary conditions and heterogeneous domains in a realistic way, it has been chosen for modeling the Princeton MRI experiment. Concerning the Madison Dynamo Experiment, another code has been used in this work, the `DYNAMO` code, which has been exactly tailored to the Madison set-up. It has to be mentioned that another code has been used in support of `SFEMaNS`, namely the `Heracles` code, a finite volume code already used for modeling the Princeton experiment. This code exploits a high order Godunov scheme and can support adaptive mesh refinement, and it has been originally developed for problems in astrophysical magnetohydrodynamics and radiative transport. In this Chapter, however, we will focus our attention on the first two codes, since they constitute the two tools used by the author of this dissertation. An introduction to `Heracles` can be found in [74] and a description of how it has been used to model the Princeton MRI experiment can be found in [90, 91].

Contents

4.1 The `SFEMaNS` code 52

4.1.1 Solving the MHD system in heterogeneous domains 52

4.1.2 Nondimensionalization of the equations 53

4.1.3 Boundary conditions on the magnetic field 54

4.2 The DYNAMO code 56
4.2.1 Formulation of the problem in spherical geometry 57
4.2.2 Characteristic velocity and time-scales 59
4.3 Summary 59

4.1 The SFEMaNS code

SFEMaNS (**S**pectral/**F**inite **E**lement code for **M**axwell **a**nd **N**avier-**S**tokes equation) is an F90 code developed since 2002 by J.-L. Guermond, C. Nore, J. Léorat, R. Laguerre, A. Ribeiro and F. Ludden. It solves the MHD equations (or only the Navier-Stokes or the Maxwell equations) in systems with cylindrical geometry, exploiting a Fourier decomposition via FFTW in the azimuthal direction and a Lagrange Finite Element solver in the meridional plane. There are two levels of parallelization: (i) The Fourier decomposition is calculated in parallel and (ii) the meridional plane undergoes a domain decomposition via METIS (Serial Graph Partitioning and Fill-reducing Matrix Ordering, [92]). The strength of this code lies in the fact that the MHD system can be solved in heterogeneous domains (e.g., jumps in the permeability of the materials are allowed) and that realistic boundary conditions on the magnetic field can be imposed. Moreover, the code enable to use local mesh refinements that can be useful in resolving strong gradients, especially close to the boundaries, where discontinuities in the viscous forcing take place. Technical details about the implementation, the notation, the time integration, the computation of nonlinear terms and the weak formulation that cannot be found in this chapter are well thoroughly described in [93].

4.1.1 Solving the MHD system in heterogeneous domains

In the following, Ω_c will indicate the region of space where the conductivity is non zero, whereas Ω_v the non-conducting one. Ω_{cf} is further partitioned into a fluid region ω_{cf} and a solid region Ω_{cs}; the interface between the conducting region and the non-conducting region is denoted by $\Sigma = \partial\Omega_c \bigcap \partial\Omega_v$. SFEMaNS solves the Navier-Stokes equations in the fluid region Ω_{cf} and/or the Maxwell equations in $\Omega = \Omega_c \bigcup \Omega_v$, i.e.,

$$\begin{cases} \left(\frac{\partial}{\partial t} + \mathbf{u}\cdot\nabla\right)\mathbf{u} - \nu^{-1}\nabla^2\mathbf{u} + \frac{1}{\rho}\nabla p = \frac{1}{\rho}(\nabla\times\mathbf{H})\times\mu\mathbf{H} + \mathbf{f} & \text{in } \Omega_{cf}, \\ \nabla\cdot\mathbf{u} = 0 & \text{in } \Omega_{cf}, \\ \mathbf{u}|_{\partial\Omega_{cf}} = \mathbf{d}, \end{cases} \tag{4.1}$$

where $\mathbf{d}$ represents the boundary conditions on the velocity field, and

$$\begin{cases} \mu \frac{\partial}{\partial t}\mathbf{H} = -\nabla \times \mathbf{E} & \text{in } \Omega, \\ \nabla \times \mathbf{H} = \begin{cases} \sigma(\mathbf{E} + \tilde{\mathbf{v}} \times \mu\mathbf{H}) + \mathbf{j}_s & \text{in } \Omega_c, \\ 0 & \text{in } \Omega_v, \end{cases} & \\ \nabla \cdot \mathbf{E} = 0 & \text{in } \Omega_v, \\ \mathbf{E} \times \mathbf{n}|_{\partial\Omega} = \mathbf{a} & \\ \int_{\Gamma_v^i} \mathbf{E} \cdot \mathbf{n} = 0 & 1 \leq i \leq J, \end{cases} \tag{4.2}$$

where Γ_v^i represents each of the connected components of $\partial\Omega_v$ that contains $\partial\Omega \bigcap \partial\Omega_v$; $\mathbf{j}_s$ is the source current; $\mathbf{n}$ is the outward normal of $\partial\Omega$; $\tilde{\mathbf{v}}$ is an extension of $\mathbf{u}$ on Ω_c, i.e., $\tilde{\mathbf{v}}$ is equal to $\mathbf{u}$ on Ω_{cf} and is prescribed in Ω_{cs}. As usual in heterogenous domains, the magnetic field $\mathbf{H}$ is used instead of $\mathbf{B}$ for reason of simplicity in the boundary conditions, and the permeability μ does not commute with any derivative (such as $\nabla\times$). By introducing the scalar potential ϕ : $\mathbf{H} = \nabla\phi$ in Ω_v (if this is simply connected), the transmission conditions are

$$\begin{cases} \mathbf{H}^c \times \mathbf{n}^c + \nabla\phi \times \mathbf{n}^v = 0 & \text{on } \Sigma \\ \mu^c \mathbf{H}^c \cdot \mathbf{n}^c + \mu^v \nabla\phi \cdot \mathbf{n}^v = 0 & \text{on } \Sigma, \end{cases} \tag{4.3}$$

where the superscript c represents quantities referring to the conducting region. Therefore, `SFEMaNS` solves the problem in its *weak formulation*, using – in the meridional plane – iso-parametric triangular $\mathbb{P}_2$ finite elements for the velocity field and the scalar potential, triangular $\mathbb{P}_1$ finite elements for the pressure, either triangular $\mathbb{P}_1$ or iso-parametric $\mathbb{P}_2$ finite elements for the magnetic field.

4.1.2 Nondimensionalization of the equations

The governing equations are then de-dimensionalized (see Appendix A). The fundamental assumption is that the characteristic velocity $U \ll c$, where c is the speed of light. The reference time scale is the eddy-turnover time $\tau = L/U$, where L is the characteristic length of the conducting region Ω_{cf}. The fluid density ρ is constant and the reference pressure scale is set equal to ρU^2. The reference magnetic permeability and electric conductivity are – respectively – μ_0 and σ_0. The magnetic field reference scale is chosen in such a way that the Alfvén speed associated to it is equal to one, i.e., $\mathcal{H} = U\sqrt{\rho/\mu_0}$. The reference scale for the electric field $\mathcal{E}$ is set to be $\mathcal{E} = \mu_0 \mathcal{H} U$, the source current $\mathbf{j}^s$ and the data $\mathbf{u}_0$, $\mathbf{d}$, $\mathbf{H}_0$, $\mathbf{a}$ are de-dimensionalized by using – respectively – $\mathcal{H}/L$, U, U, $\mathcal{H}$ and $\mathcal{H}$. With this rescaling of the physical variable, the system – in its dimensionless form – becomes

$$\begin{cases} \left(\frac{\partial}{\partial t} + \mathbf{u}\cdot\nabla\right)\mathbf{u} - Re^{-1}\nabla^2\mathbf{u} + \nabla p = (\nabla\times\mathbf{H})\times\mu\mathbf{H} + \mathbf{f} & \text{in } \Omega_{cf}, \\ \nabla\cdot\mathbf{u} = 0 & \text{in } \Omega_{cf}, \\ \mathbf{u}|_{\partial\Omega_{cf}} = \mathbf{d}, \end{cases} \tag{4.4}$$

where $\mathbf{d}$ represents the boundary conditions on the velocity field, and

$$\begin{cases} \mu\frac{\partial}{\partial t}\mathbf{H} = -\nabla\times\mathbf{E} & \text{in } \Omega, \\ \nabla\times\mathbf{H} = \begin{cases} Rm\sigma(\mathbf{E} + \tilde{\mathbf{v}}\times\mu\mathbf{H}) + \mathbf{j}_s & \text{in } \Omega_c, \\ 0 & \text{in } \Omega_v, \end{cases} & \\ \nabla\cdot\mathbf{E} = 0 & \text{in } \Omega_v, \\ \mathbf{E}\times\mathbf{n}|_{\partial\Omega} = \mathbf{a} & \\ \int_{\Gamma_v^i}\mathbf{E}\cdot\mathbf{n} = 0 & 1 \le i \le J, \end{cases} \tag{4.5}$$

where in this case the symbols σ and μ represent – respectively – the *relative* conductivity and permeability.

4.1.3 Boundary conditions on the magnetic field

In order to impose realistic boundary conditions on the conducting region Ω_c, `SFEMaNS` adopts the following solution: The vacuum region around the conducting region is taken into account and the boundary conditions on the conducting region become transmission (or continuity) conditions between the magnetic field in Ω_c and the gradient of the scalar potential in Ω_v. Usually, finite volume codes that limit their calculations only in the conducting region impose boundary conditions on the magnetic field that are in principle less realistic. For instance, the so-called *pseudo-vacuum* boundary conditions are usually applied, where the magnetic field is forced to be perpendicular to the boundary surface. With the solution adopted in `SFEMaNS`, a relatively small part of the computation is used for the vacuum region, but this pays off in terms of accuracy. Moreover, solving the Maxwell equation also in Ω_v gives to the user the possibility to give predictions on the magnetic field in a region that is more accessible – for practical reasons – to the experimentalists, who cannot measure up to now the magnetic field inside the cylinder.

The vacuum region where the Maxwell equations are solved is – of course – spatially limited and this unavoidable truncation represents a source of inaccuracy, although negligible if the size of Ω_v is big enough (i.e., if points on $\partial\Omega_v$ are far enough from Ω_c, such that the boundary conditions on ϕ do not have a strong effect on $\partial\Omega_c$). Typically, the vacuum region is bounded

by a sphere or cylinder with a radius 10 times larger than the reference length scale (i.e., the size of the conducting region). It has been verified [93] that truncating the vacuum domain in this way is sufficient to guarantee less than one per cent accuracy due to truncation.

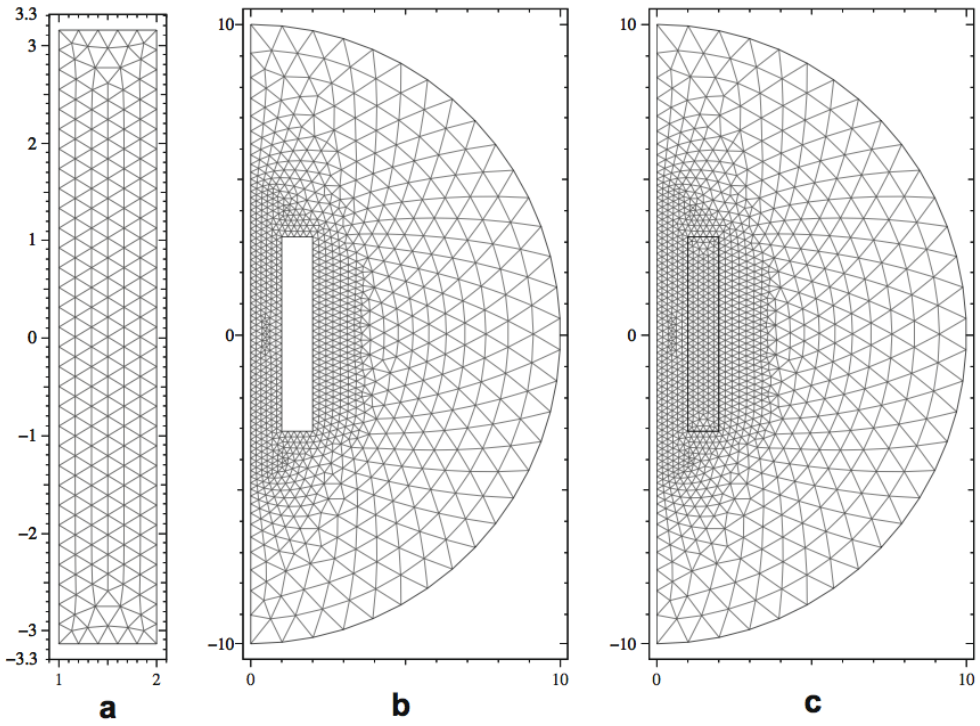

Figure 4.1: An example of how SFEMaNS handles the boundary condition on the magnetic field, as described in Section 4.1.3: (a) mesh of the conducting region Ω_c, where the MHD system is solved; (b) mesh of the vacuum region, where the Maxwell system is solved with boundary condition on the scalar potential imposed on the exterior circular boundary; (c) the combination of the two meshes. Transmission/continuity conditions between the magnetic field in the conducting region and the gradient of the scalar potential are imposed on the interface between the two meshes. Reprinted from [93], with permission from Elsevier.

After reviewing the most important features of SFEMaNS (further reading can be found in the references cited above), in the following Section we will give an overview of the most important characteristics of the DYNAMO code. Although SFEMaNS could be able to simulate the Madison Dynamo Experiment (since the forcing mechanism is axisymmetric), the DYNAMO code was chosen because it was written exactly to mimic the Madison device. Moreover, past numerical investigations of this experiment have been already carried out with the DYNAMO code (see [87, 94–97]).

4.2 The DYNAMO code

The DYNAMO code [98] solves – in spherical geometry – the nonlinear equations of incompressible MHD, i.e., the *magnetic induction equation* coupled with the Navier-Stokes equation, by computing three-dimensional time-dependent solutions for the velocity and magnetic fields. The simulated system has been designed to model the MDE, having the same geometrical and dynamical features. In particular, the code focuses on the so-called *s2t2* type of flow (see [80] for a definition), although it could in principle study different forcing mechanisms (i.e., different flows). The code exploits a pseudo-spectral method based on spherical harmonics decomposition, and had originally been developed by R. A. Bayliss and C. B. Forest at the University of Wisconsin-Madison [98,99], and afterwards extended and parallelized via MPI by K. Reuter [94]. The parallelization was performed by dividing the sphere in spherical shells. Further details on the physical model, the stirring force, the numerical setup and the parallelization of the code can be found in [94]. The magnetic induction equation, in its nondimensional form, reads

$$\frac{\partial \mathbf{B}}{\partial t} = Rm \nabla \times (\mathbf{u} \times \mathbf{B}) + \nabla^2 \mathbf{B}, \tag{4.6}$$

where $Rm = \mu_0 \sigma R U$ is the magnetic Reynolds number, R the characteristic length associated with the system (the radius of the sphere), U the characteristic velocity and σ the conductivity of the medium. In order to correctly de-dimensionalize this equation, time is scaled to the resistive diffusion time $\tau_\sigma = \mu_0 \sigma L^2$. As stated above, in the case $Rm \gg 1$, the advection term dominates and a dynamo mechanism takes place if the geometry of the flow $\mathbf{u}$ can support it.

One of the previous key results obtained by the DYNAMO code was the discovery of a hydrodynamic instability in the weakly turbulent regime, i.e., the exponential growth of modes with $m = 2$ symmetry located in the shear layer region between the forced regions and the walls of the sphere [95]. In the nonlinear saturation regime, these modes manifest themselves as hydrodynamic waves propagating in the zonal direction, oppositely directed in each hemisphere. Increasing the Reynolds number above the wave-dominated regime causes new bifurcations, finally leading to inhomogeneous anisotropic turbulence. Kinematic dynamo simulations using the time averaged flow or different snapshots of the velocity field did not exhibit dynamo action, whereas growing magnetic fields were found when considering the time-dependent flow. This result is linked to the presence of perpetual *non-normal growth* due to the mathematical property of the magnetic induction equation's linear operator, being time dependent and non self-adjoint [100]. Finally, the stability curve $Rm_c(Re)$ of this system, i.e., the dependence of the dynamo threshold on the fluid Reynolds number, was also determined [96].

4.2.1 Formulation of the problem in spherical geometry

The spherical symmetry naturally suggests the use of spherical coordinates. Moreover, in order to eliminate the pressure term, the curl of the nondimensional Navier-Stokes equation – i.e., the vorticity equation – is solved by the code. The nondimensional vorticity transport equation reads,

$$\frac{\partial \boldsymbol{\omega}}{\partial \tau} = Rm \nabla \times \mathbf{G} + Pm \nabla^2 \boldsymbol{\omega}, , \tag{4.7}$$

where

$$\mathbf{G} = \mathbf{u} \times \boldsymbol{\omega} + (\nabla \times \mathbf{B}) \times \mathbf{B} + \mathbf{f}, \tag{4.8}$$

and $\mathbf{f}$ is the counterrotating force. In the following, the Bullard-Gellman decomposition (also called *poloidal-toroidal* or *Mie* decomposition) will be extensively used, since it is particularly advantageous in spherical geometry. The incompressible velocity field $\mathbf{u}(\mathbf{x}, \tau)$ is divergence-free, hence it can be written as

$$\mathbf{u}(\mathbf{x}, \tau) = \nabla \times \nabla \times [s(\mathbf{x}, \tau)\mathbf{x}] + \nabla \times [t(\mathbf{x}, \tau)\mathbf{x}], \tag{4.9}$$

where the scalars $s(\mathbf{r}) = s(r, \theta, \phi)$ and $t(\mathbf{r}) = t(r, \theta, \phi)$ are called – respectively – the poloidal and toroidal stream functions. These functions can be – in turn – expanded in terms of spherical harmonics, i.e.,

$$s(r, \theta, \phi) = \sum_{l=0}^{\infty} \sum_{m=0}^{l} s(r)_l^m \mathcal{Y}_l^m(\theta, \phi), \tag{4.10}$$

$$t(r, \theta, \phi) = \sum_{l=0}^{\infty} \sum_{m=0}^{l} t(r)_l^m \mathcal{Y}_l^m(\theta, \phi), \tag{4.11}$$

where $\mathcal{Y}_l^m$ is the spherical harmonics with "angular momentum" and azimuthal wavenumbers l and m. The azimuthal wavenumber is limited to $m \geq 0$ since all vector fields are real-valued. Using the triangular truncation, the total number of relevant spectral modes is given by

$$(l_{max} + 1)(l_{max} + 2)/2 - 1, \tag{4.12}$$

where l_{max} is the maximum "angular momentum wavenumber". The monopole mode $l = 0$ is not required due to the divergence free constraints. To account for dealiasing, the upper third of the spectrum is truncated by choosing $\frac{2}{3}N_\theta - 1 \geq l_{max}$ and $N_\phi = 2N_{theta}$, where N_θ and N_ϕ are the number of latitudinal and longitudinal points used in the real space representations of the vector fields [87, 94].

By making use of this decomposition, the vorticity becomes

$$\boldsymbol{\omega} = \nabla \times \nabla \times [t(\mathbf{x}, \tau)\mathbf{x}] + \nabla \times [(-\nabla^2 s(\mathbf{x}, \tau))\mathbf{x}]. \tag{4.13}$$

By applying the operators $(\mathbf{x}\cdot)$ and $(\mathbf{x}\cdot\nabla\times)$ on the vorticity equation, a separation into two equations which govern the temporal evolution of the poloidal and toroidal stream functions is found (since the position vector $\mathbf{x}$ and the toroidal component of the field are orthogonal. Expanding the stream functions in terms of spherical harmonics as already anticipated, the following evolution equations for the radial profiles $s_l^m(r,\tau)$ and $t_l^m(r,\tau)$ are obtained,

$$\frac{\partial}{\partial\tau}\mathcal{D}_l s_l^m(r,\tau) - Pm\mathcal{D}_l^2 s_l^m(r,\tau) = -\frac{Rm}{l(l+1)}[\mathbf{x}\cdot\nabla\times\nabla\times\mathbf{G}]_l^m, \tag{4.14}$$

$$\frac{\partial}{\partial\tau}t_l^m(r,\tau) - Pm\mathcal{D}_l t_l^m(r,\tau) = \frac{Rm}{l(l+1)}[\mathbf{x}\cdot\nabla\times\mathbf{G}]_l^m, \tag{4.15}$$

where

$$\mathcal{D}_l = \frac{\partial^2}{\partial r^2} + \frac{2}{r}\frac{\partial}{\partial r} - \frac{l(l+1)}{r^2} \tag{4.16}$$

is the Laplacian operator written in spherical coordinates and where the eigenvalue relation

$$\left(\frac{1}{\sin\theta}\frac{\partial}{\partial\theta}\sin\theta\frac{\partial}{\partial\theta} + \frac{1}{\sin^2\theta}\frac{\partial^2}{\partial\phi^2}\right)\mathcal{Y}_l^m(\theta,\phi) = -l(l+1)\mathcal{Y}_l^m(\theta,\phi) \tag{4.17}$$

has been used. The square brackets around the right hand side terms represent the respective radial profiles of the $l-m$ coefficient of the toroidal or poloidal scalar potentials of the vector quantities inside the brackets. Smilarly, the magnetic induction equation can be subjected to the same decomposition, and equations for the poloidal and toroidal magnetic stream functions $S(\mathbf{x},\tau)$ and $T(\mathbf{x},\tau)$ are found. These resulting equations are the same as (4.14) and (4.15), but there the $\mathbf{u}\times\mathbf{B}$ term plays the role the $\mathbf{G}$ has in (4.14) and (4.15).

By using the Bullard-Gellman and the spherical harmonics decomposition, spectrally decoupled equations are found. The convolutions in the square brackets on the right hand sides couple different modes with each other and have to be evaluated separately. A pseudo-spectral method is used to compute these convolutions, i.e., the curls are evaluated in spectral space and the vector products in real space, paying off in terms of simplicity, speed and accuracy [101]. The reason why pseudo-spectral methods are faster than full-spectral methods comes from the fact that they avoid the complications of the full-spectral methods which rely on term-by-term integrations of spectral components. On the other hand, the pseudo-spectral method has the disadvantage of introducing discretization error through aliasing. This error is addressed by padding and truncating the spectrumpad.

In order to evolve the MHD equations forward in time, an operator-splitting approach is used: The pseudo-spectral convolution terms are integrated using an explicit predictor-corrector scheme, whereas a semi-implicit Crank-Nicolson method is used to integrate the diffusion terms, therefore avoiding intractably small time steps. The Crank-Nicolson method implicitly averages the diffusive terms and computes a temporal derivative accurate to second order. The fluid advection term has a hyperbolic character due to the propagation of inertial waves, making it advantageous to use an explicit advancement for nonlinear terms. An explicit second-order Adams-Bashforth predictor-corrector scheme is used to advance the pseudo-spectral nonlinear terms. Other details about the boundary conditions, the forcing function $\mathbf{f}$, the parallelization, the code optimization can be extensively found in [87, 99].

4.2.2 Characteristic velocity and time-scales

The characteristic velocity U of each simulation is, used in the definition of the Reynolds numbers Rm and $Re = Rm/Pm$, is determined *a posteriori* from the results of each numerical simulation. Following an established convention, the velocity normalization is defined by $U = \overline{\sqrt{\langle \mathbf{u}^2 \rangle}}$, where the angle brackets denote averaging in space and the overline denotes averaging in time which is performed during the quasi-stationary phase of the flow after all initial transient phase. A unit sphere is assumed, i.e., the characteristic length $L = 1$ which is justified by the fact that a poloidal circulation cell of the *s2t2* flow extends nearly over one full radius. The characteristic timescale of the flow is defined by the turnover time of the largest eddies $\tau_v = L/U$ which is also the relevant timescale for magnetic induction resulting from the large-scale flow. The magnetic diffusion time $\tau_\sigma = Rm\tau_v = \mu_0 \sigma L^2$ is the timescale relevant to resistive decay of a magnetic field.

4.3 Summary

In this Chapter, we have described the most important features that characterize the `SFEMaNS` and the `DYNAMO` code, namely the codes used to simulate – respectively – the MRI and the dynamo experiments. The first code solves the incompressible MHD equations in axisymmetric systems, exploiting a Fourier decomposition via FFTW in the azimuthal direction and a Lagrange Finite Element solver in the meridional plane. The code has two levels of parallelization. Beside `SFEMaNS`, a finite volume code – called `Heracles` – has been used in order to benchmark the `SFEMaNS` results and support this investigation. Concerning dynamo theory, a pseudo-spectral code has been used. This code solves the nonlinear equations of incompressible MHD in spherical geometry and it is particularly suitable for modeling the Madison

Dynamo experiment, as previous investigations have already shown. In the next Chapters, we will describe the core of this dissertation, namely the results obtained by means of this numerical tools.

Chapter 5

Modeling the Magnetorotational Instability experiment

The experimental confirmation of the presence of the MRI is still missing and several laboratory experiments – such as the Princeton MRI experiment – are investigating this effect. The Princeton MRI Experiment has been designed in order to catch the MRI instability in the lab. This apparatus has been providing data whose physical interpretation is still under debate, since the current setup has experienced difficulties in disentangling the MRI effect from other instabilities (hydro- or magnetohydro-). Numerical simulations are supposed to provide a better understanding of the experimental behaviors, providing signatures and suggesting measurements to take in the laboratory in order to distinguish the experimental runs where the MRI mode is non-negligible from the ones where it is. In this Chapter, we report MHD simulations carried out in order to model this device, and in order to answer open questions concerning the experimental detectability of the MRI. For the simulations, a two code approach has been carried out by using `Heracles` (a finite volume code) and `SFEMaNS` (a spectral and finite element code), the latter being used by the author of this dissertation (see description in Chapter 4). After a period where the codes will be benchmarked against themselves and the experiments, they could then describe which physical processes lead to the experimental results, in particular focusing on the recent claim that the magnetized flow obeys a self-similar law that can be modified by a strong MRI amplitude [75]. If this last statement will be confirmed, a novel method would be provided that tells whether the MRI is occurring or not. To perform this task, we adopted a new approach that closely resembles the experimental methodology and improves the comparability of the simulated data to the experiment. We investigate a scaling relation of the azimuthal velocity that has recently been found in the ex-

periment and that could be a possible indicator for the MRI. We show that for our simulations the experimentally observed scaling relation is nearly obtained for simulations with small MRI amplitudes. Furthermore, we find a strong correlation between the strength of the MRI and the deviation from this scaling, both in terms of magnitude and shape. These results suggest that this scaling relation is indeed an indicator for the MRI. The comparison of these results with experimental data indicates that the MRI amplitude in the experiment is too small to cause a measurable deviation from the reported scaling of the azimuthal velocity. This estimation is supported by the extrapolation of the MRI amplitude to the real Reynolds numbers of the experiment.

The main objective of the MRI subproject – from a numerical point of view – was to prove that the `SFEMaNS` was able to successfully model the experiment, providing a first series of results. In this Chapter, we will discuss the steps we took in order to perform this task.

Contents

5.1 `SFEMaNS`: Geometry and mesh 62
5.2 Benchmark of `SFEMaNS` and code validation . . . 63
5.3 Axisymmetric runs 65
5.3.1 Inflow *vs* outflow mid-plane jets 70
5.3.2 Scaling of the MRI Amplitude with Re 74
5.4 Conclusions and outlook 77

5.1 `SFEMaNS`: Geometry and mesh

One fundamental step to take when dealing with a Finite Element code is the creation of a mesh that models the geometry of the system with the appropriate resolution. Figure 3.3 of reference [59] provides a detailed sketch of the geometry in the meridional plane that we used as a reference for the generation of our grid. The step size within the conducting region has been chosen according to previous calculations [102]; correspondingly, the temporal step has been set in order to abundantly fulfill the CFL inequality, i.e.,

$$\max_{\mathbf{r}\in\Omega_{cf}} \frac{u(\mathbf{r})\mathrm{d}t}{h} < 0.5,$$

where u is the velocity magnitude, $\mathrm{d}t$ is the discrete time marching increment and h is the mesh step size. The choice of $\mathrm{d}t$ is particularly crucial, since the main MRI mode appears with a very high growth rate and the right $\mathrm{d}t$ is needed in order to catch and resolve the MRI. Moreover, the strategy described in Chapter 4 designed to realistically handle the magnetic boundary

conditions has been exploited. Figures 5.1-5.2 show the meridional plane mesh, with a particular emphasis on the non-homogeneity of the mesh.

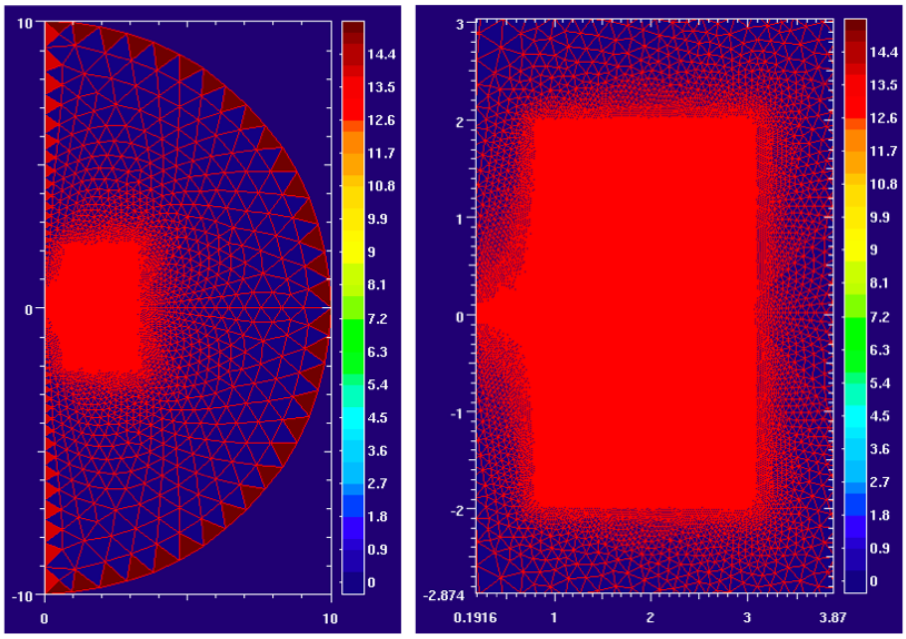

Figure 5.1: *Left*: Mesh of the meridional plane rz of the whole computational domain Ω. A fine resolution of the frontier of the sphere is not required. *Right*: Zoom-in of the left picture: The rectangular conducting domain Ω_c is better resolved.

As already mentioned in Chapter 4, the meridional plane undergoes a domain decomposition procedure (via the software `METIS`) in order to run the simulations in parallel. Figure 5.3 shows a typical partition of the conducting and vacuum domains, realized in order to assign each domain to a different processor.

5.2 Benchmark of `SFEMaNS` and code validation

The feasibility of using `SFEMaNS` to address the MRI problem in this geometry has been extensively studied by benchmarking the results against data produced by `Heracles`, which has been already used to simulate the MRI experiment [25]. Our benchmark has been also described in [91, 103].

For instance, Figures 5.4-5.9 show a series of comparisons of the flow in the meridional plane for hydrodynamic runs with the same initial set-up and the same temporal snapshot (i.e., at t = 0.14 s). The qualitative structure of the flow is similar and distinctive patterns are easily recognizable in both codes. The results agree more and more as the runtime goes on, since – at

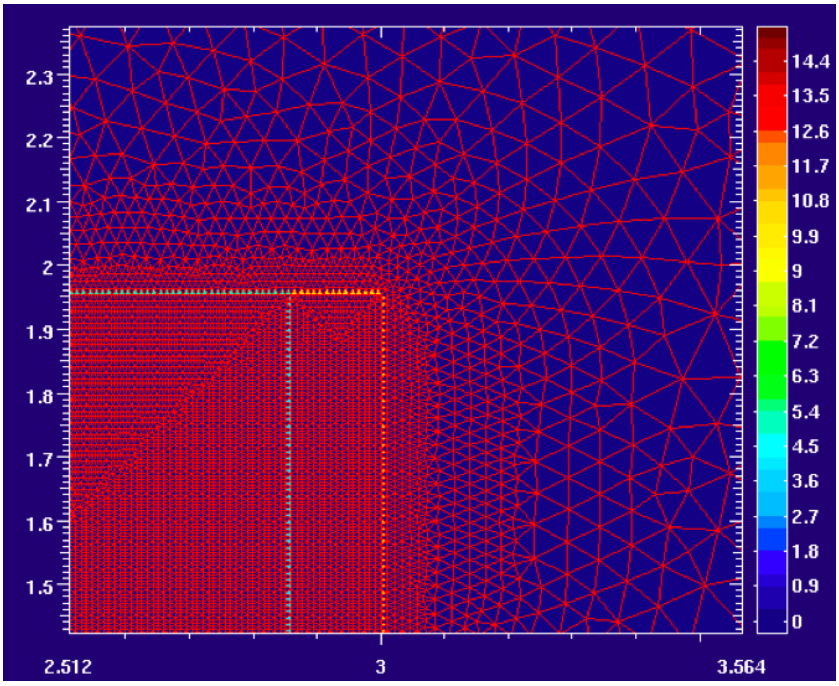

Figure 5.2: Further zoom-in of Figure 5.1. The conducting fluid region Ω_{cf} in the bottom left corner has the same spatial resolution of the conducting, rotating, solid wall (the vertical rectangle in the center), whereas the vacuum region shows a coarser mesh.

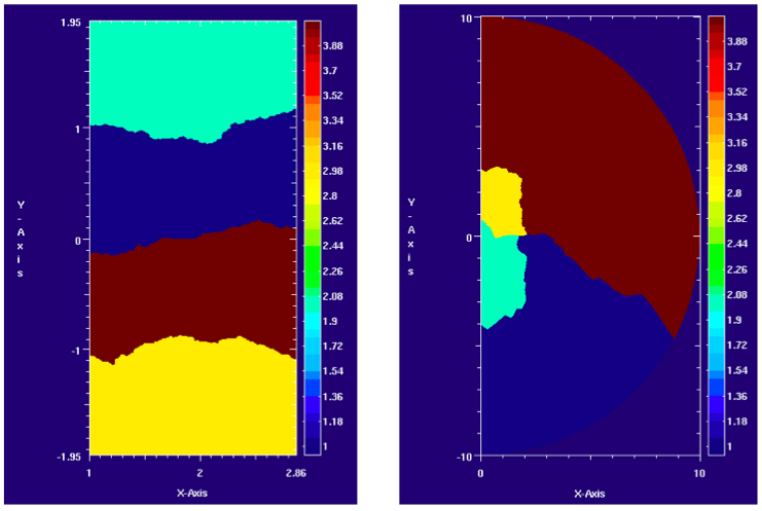

Figure 5.3: Typical partition of the conducting (*left*) and vacuum (*right*) domains obtained – by using `METIS` – in order to assign each portion of the decomposed domain of the meridional plane to one processor.

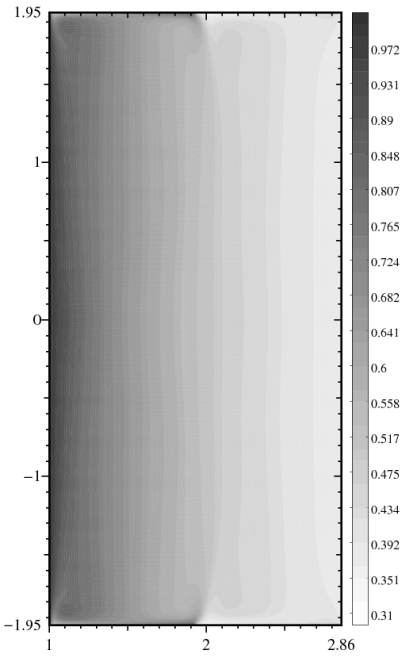

Figure 5.4: θ-component of the flow in the meridional plane as calculated by `SFEMaNS`, t=0.14 s.

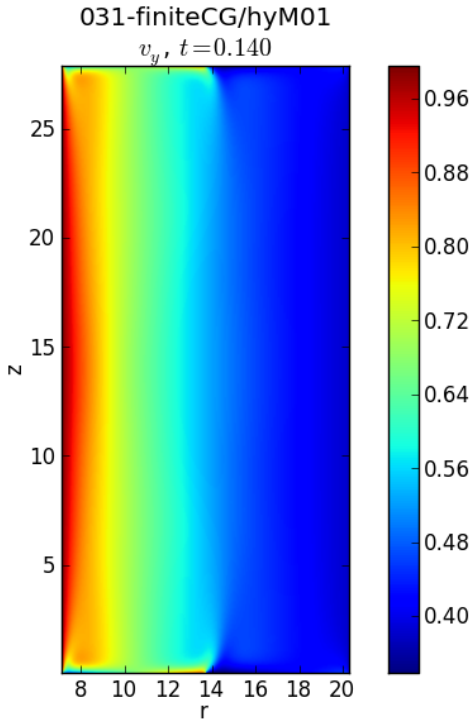

Figure 5.5: θ-component of the flow in the meridional plane as calculated by `Heracles`, t=0.14 s.

the beginning of the runs – waves and transient wave-like phenomena are found with `Heracles`.

5.3 Axisymmetric runs

The simulations described here have been carried out in axisymmetry, as there seems to be little nonaxisymmetric structure in this regime (true of the experiment as well as the simulations, according to the experimentalists). The magnetic boundary conditions do not seem to be decisive here: `SFEMaNS` obtains very similar results with pseudo-vacuum and true-vacuum conditions (whereas `Heracles` is capable only of pseudo-vacuum at present). For these runs, the numerical Reynolds numbers are $Re_0 = 5000$ and $Rm_0 = 15$. In order to obtain the real Reynolds numbers, they should be multiplied by the characteristic length $L = 1.86 (= R_2 - R_1)$ and – in principle – by the characteristic velocity $U (= \Omega_1 R_1)$ (which depends on the particular simulation set-up). By doing so, and considering that a run with 75% of the maximum attainable rotation has U=0.75 (and so on...), we have $Re = \{5000, 3750, 3000, 2500, 1250\}$ and $Rm = \{15, 11.25, 9, 7.5, 3.75\}$. It is

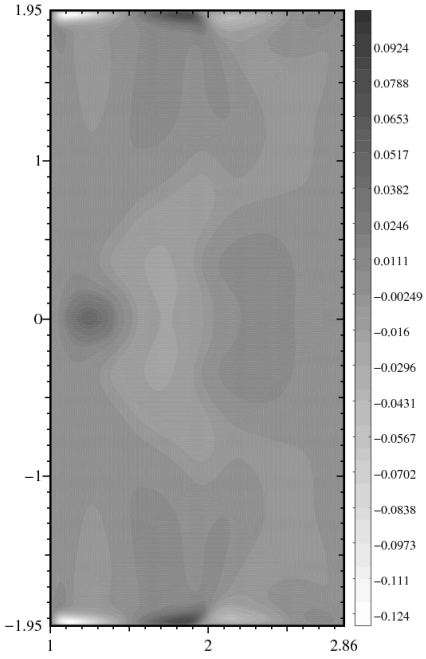

Figure 5.6: r-component of the flow in the meridional plane as calculated by `SFEMaNS`, t=0.14 s.

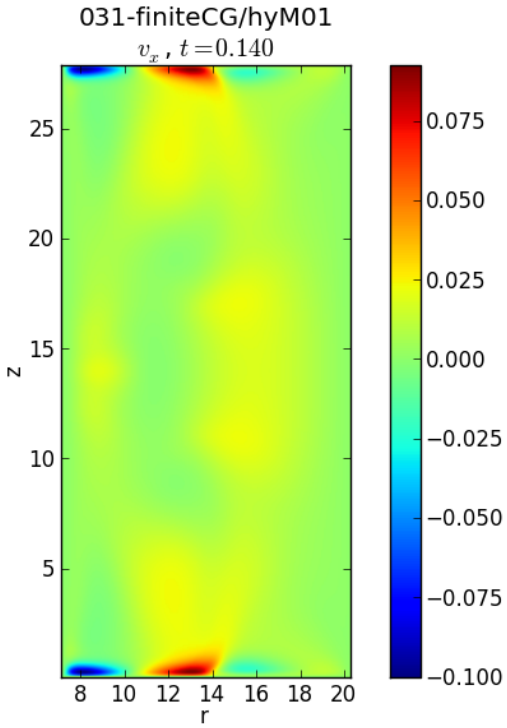

Figure 5.7: r-component of the flow in the meridional plane as calculated by `Heracles`, t=0.14 s.

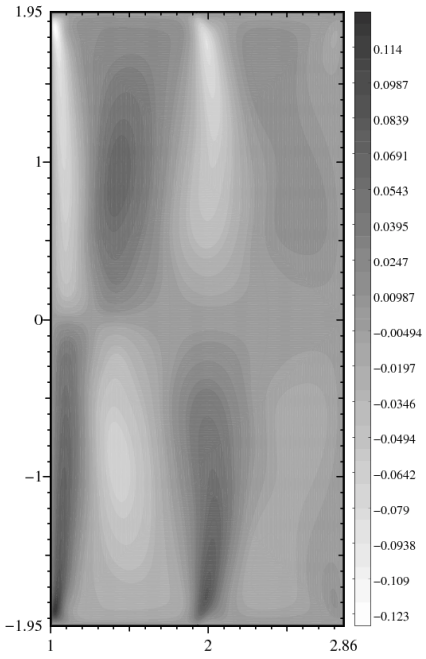

Figure 5.8: z-component of the flow in the meridional plane as calculated by `SFEMaNS`.

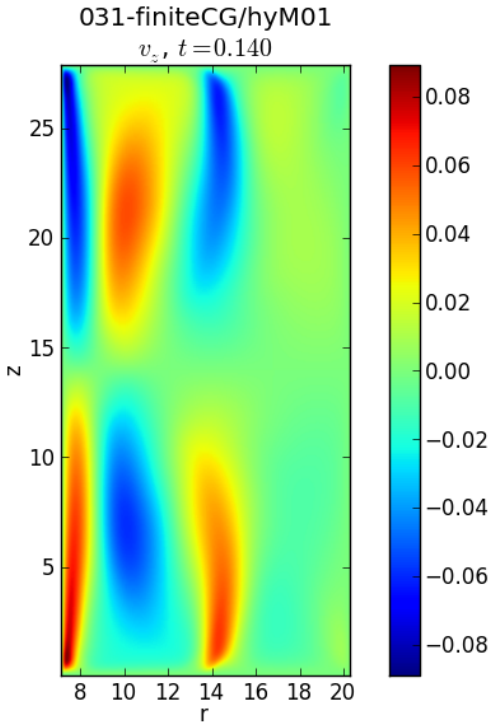

Figure 5.9: z-component of the flow in the meridional plane as calculated by `Heracles`.

important noticing that the Prandtl number Pm is constant for each series of data. Indeed, in the experiment Pm is constant (it depends only on the choice of the conducting fluid), whereas the magnetic Reynolds number Rm (and – correspondingly – the fluid Reynolds number Re) can be modified by changing the rotation rates of the cylinders. In our simulations we fixed the magnetic Prandtl number to 0.003 (a reasonable value our computational resources could handle), keeping only the applied magnetic field and the rotation rates as free parameters (as discussed also in [103]). Previous results have been focused on other aspects of the simulations, but without keeping Pm constant [25]. With this choice, we produce a database corresponding to the same conducting fluid (although more viscous than liquid gallium), and we expect that the simulated results can be compared to the experimental ones more easily. Nevertheless, an extrapolation towards smaller values of Pm is needed.

The dimensionless applied magnetic field B_0 should be multiplied by $\Omega_1 R_1 \sqrt{\mu_0 \rho}$, which corresponds to 2.62 Tesla for the 100% rotation case. Cases with a very strong applied magnetic field have been simulated, in order to benchmark the results against the high Lundquist number runs of [25].

With this series of simulations, we checked whether the codes see the same experimental observation described in Section 3.1: For a single position, $r = 16$ cm at the mid-plane, the normalized azimuthal velocity is constant for normalized Alfvén speed associated to the applied field B_0 [75], where the two quantities are normalized via $u_1 = \Omega_1 R_1$. As Figures 5.10-5.11 (data measured at $r = 16$ cm) and Figures 5.13-5.14 (data measured at $r = 15$ cm) show, the raw simulated data – once normalized – have a similar profile, almost collapsing on the same curve. As explained in section 3.1, "MRI-Z" refers to the setting $\{\Omega_2, \Omega_3, \Omega_4\} = \{0.55 \cdot \Omega_1, 0.1325 \cdot \Omega_1, 0.1325 \cdot \Omega_1\}$ used in the experiment whereas the percentages refer to the values $(\Omega_1/\Omega_{max}) \times 100$, where Ω_{max} is the maximum inner cylinder design speed, i.e., 4000 rpm. The points that show the highest departure from the collapse have been produced by simulations that show also strong MRI amplitudes. This behavior can be qualitatively understood by considering that a strong MRI amplitude can appreciably modify the θ-component of the flow, as depicted in Figure 5.12: When the MRI is strong (*left*), the azimuthal component of the velocity field u_θ shows a different spatial distribution in comparison with a case where the MRI is negligible (*right*). The two simulations have the same applied magnetic field but different rotation rates of the cylinders and endcaps, placing the first one above the MRI threshold and the second one under it in the parameter space (see Figure 3.4). When the MRI mode is strong, $u_\theta(z,t)$ shows a bump close to the mid-plane, hence enhancing the value of the measured azimuthal velocity and giving rise to the departure from the profile of Figures 5.10-5.11: the outlying point in Figure 5.11 has a very strong MRI amplitude ($\sim$20% of the

applied field, whereas in the experiment a percentage of ∼3% is expected) and corresponds to the run shown in Figure 5.12 (*left*).

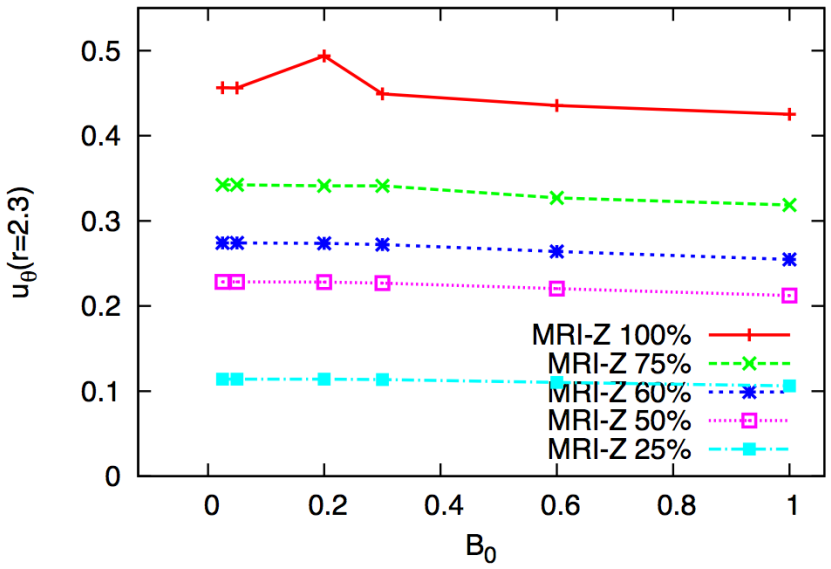

Figure 5.10: Azimuthal component of the velocity field at $r = 16$ cm for different applied fields and rotation rates obtained by `SFEMaNS`.

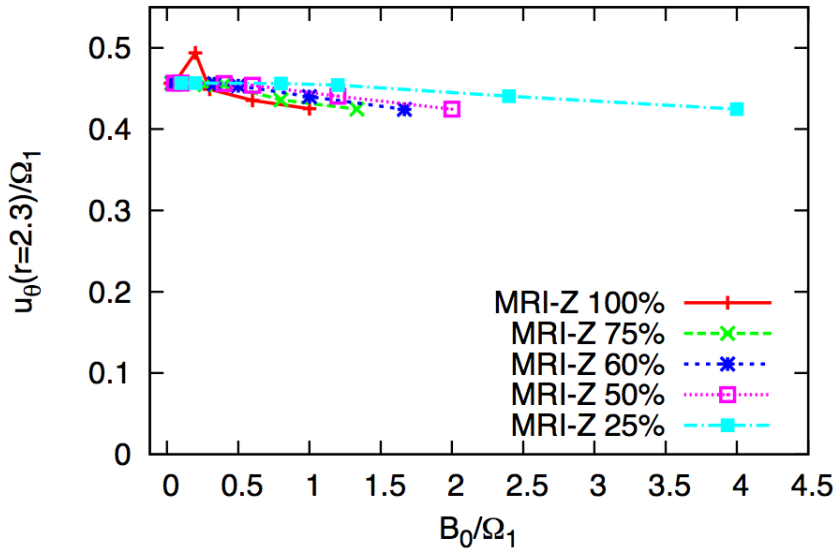

Figure 5.11: Normalized azimuthal component of the velocity at $r = 16$ cm obtained by `SFEMaNS`. Strong departures from the common data collapse are a sign of the presence of a strong MRI mode.

Similarly, as displayed in Figures 5.13-5.14, at $r = 15$ cm we find a similar behavior, although in this case the outlying point is probably due to the strong applied magnetic field. It is worth noticing that `Heracles` also finds a departure from the collapse where a strong MRI amplitude is present. Within this two-code project, `Heracles` has been providing faster simulations, i.e., better statistics and the correlation between the MRI and the departure from the data is more pronounced (see, e.g., Figures 5.15-5.17). Both codes hence confirm that – by properly normalizing the velocity and the applied magnetic field – the data tend to show the same profile; moreover, when the flow is capable of triggering a strong MRI mode, it is modified in such a way that the collapse of the date is not satisfied anymore. In section 5.4, the impact of this preliminary analysis on the future of the numerical or laboratory experiment will be discussed.

5.3.1 Inflow *vs* outflow mid-plane jets

In this section, we will address the main difference between the two codes that ought to be understood by future investigation. According to `Heracles`, the poloidal circulation of the flow always takes the form of two Ekman cells meeting in an inflow at the mid-plane, and the recirculation takes place in a narrow outflowing jet close to the endcaps (in qualitative agreement with [25]). On the other hand, the `SFEMaNS` simulations show also a two

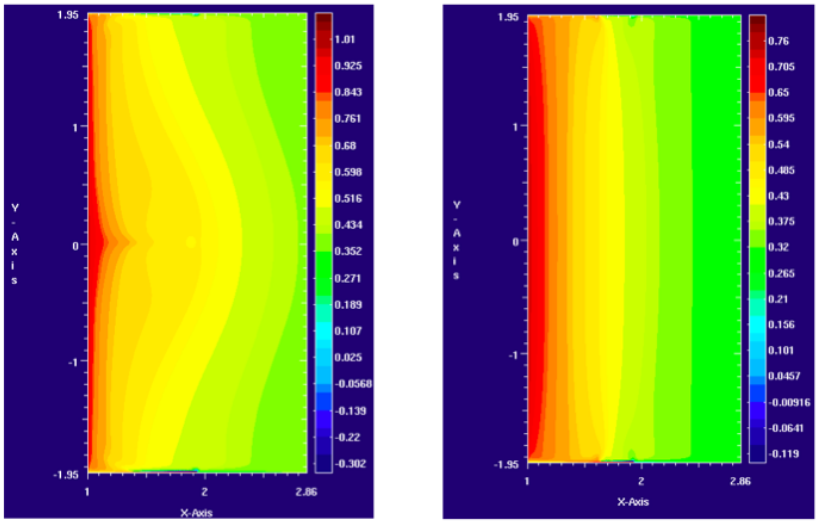

Figure 5.12: Meridional plane of the conducting fluid region, $Pm = 0.003$. The color shows the θ-component of the velocity field when (*left*) a strong MRI mode is present and (*right*) the MRI is very weak. The two simulations have the same Lundquist number S=2.3 but different rotation rates of cylinders and endcaps (i.e., different Rm).

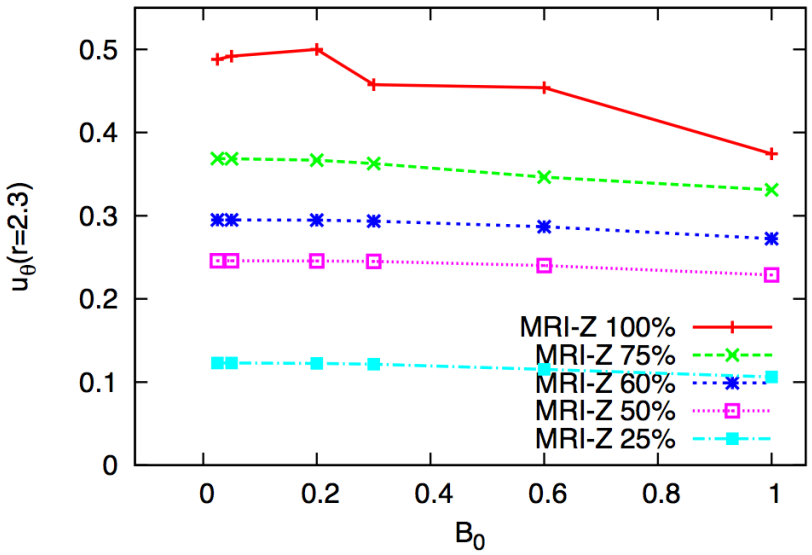

Figure 5.13: Azimuthal component of the velocity field at $r = 15$ cm for different applied fields and rotation rates obtained by `SFEMaNS`.

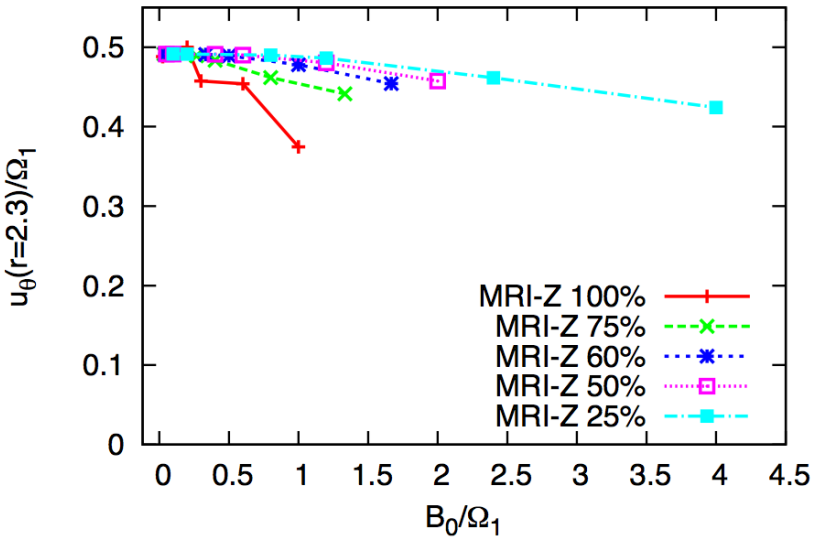

Figure 5.14: Normalized azimuthal component of the velocity at $r = 15$ cm obtained by `SFEMaNS`. The rightmost point of the red curve experiences the effect of a strong applied field, whereas departures from the pale blue profile correlate with the MRI amplitude.

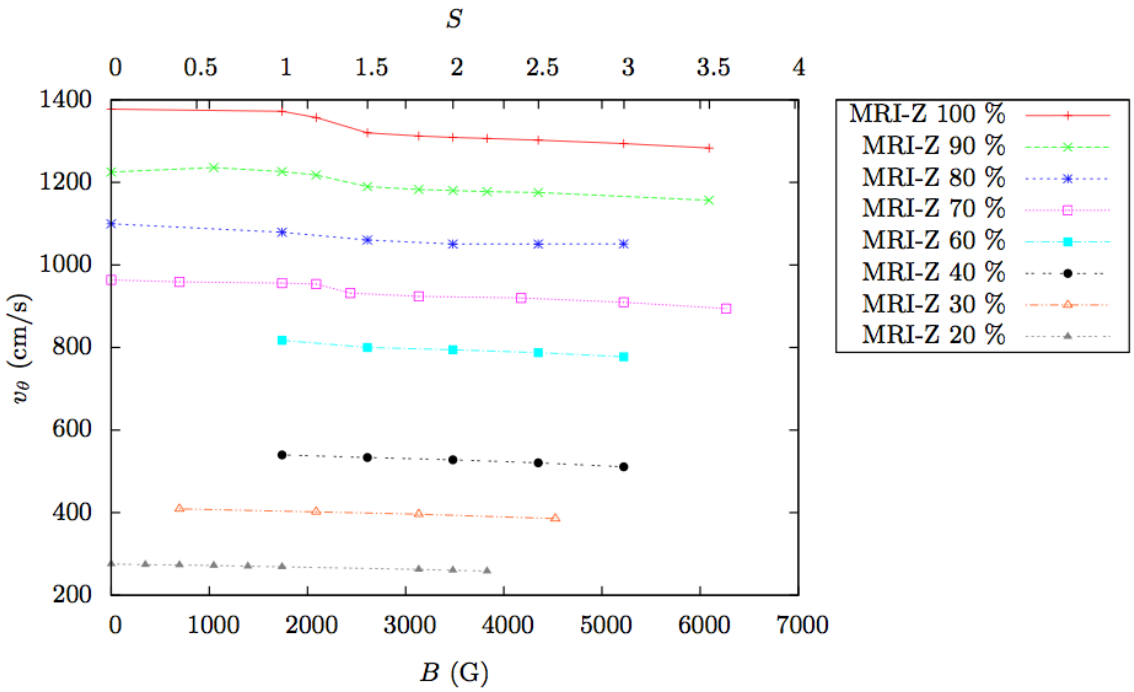

Figure 5.15: Azimuthal component of the velocity field at $r = 16$ cm for different applied fields and rotation rates obtained by `Heracles`. Figure courtesy of J. Weissmann.

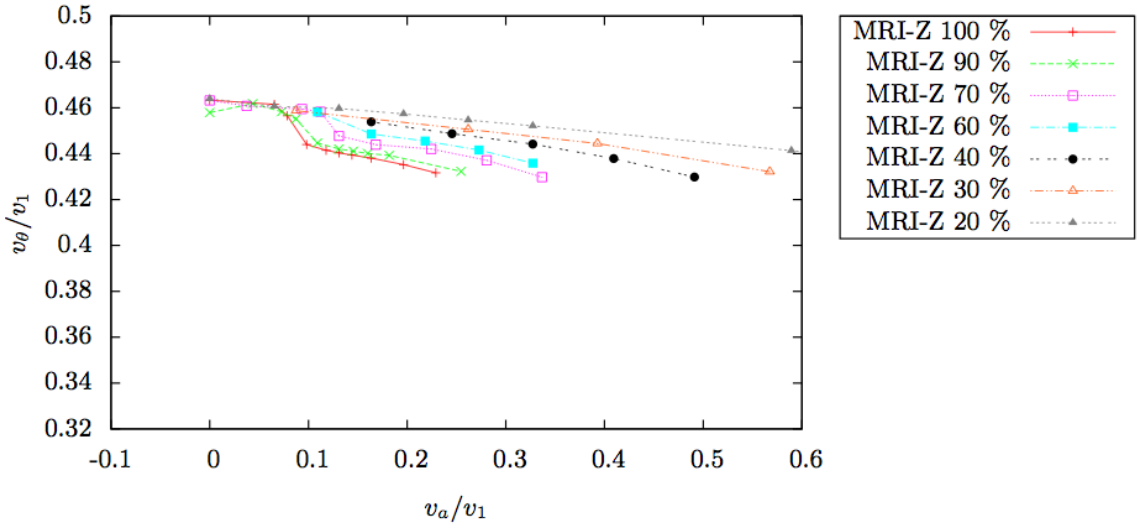

Figure 5.16: Normalized azimuthal component of the velocity at $r = 16$ cm obtained by `Heracles`. For low rotation rates the data series almost collapse, whereas, for higher rotation rates, the curves develop a bump that correlates with the strength of the MRI amplitude (Figure 5.17). Figure courtesy of J. Weissmann.

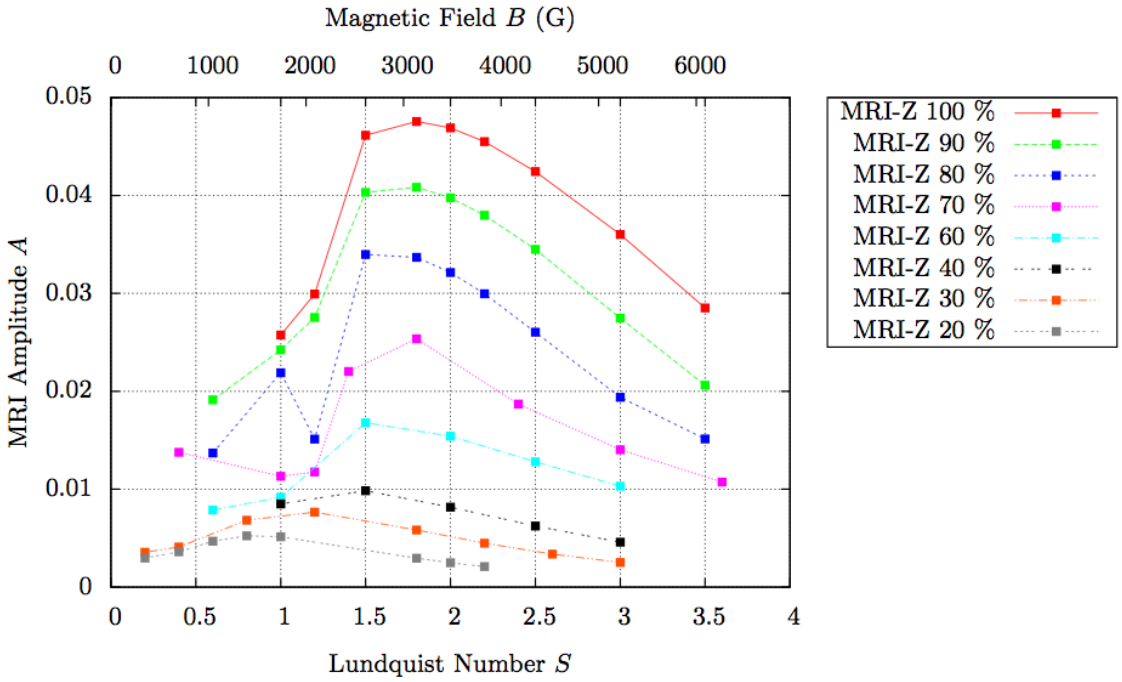

Figure 5.17: MRI amplitude *vs* applied magnetic field for runs with different rotation speeds obtained by `Heracles`. Figure courtesy of J. Weissmann.

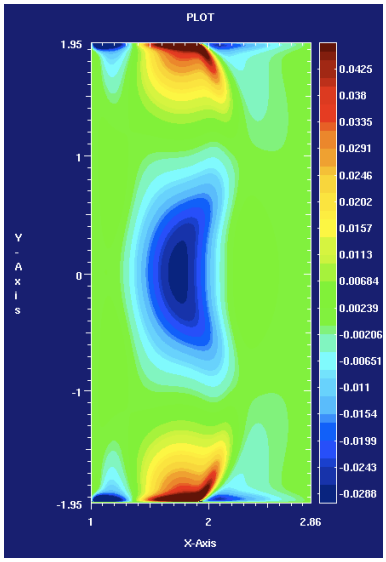

Figure 5.18: *Inflow* mid-plane jet: The poloidal circulation of the flow takes the form of two Ekman cells meeting in an *inflow* at the mid-plane, recirculating in a narrow *outflowing* jet close to the endcaps. These results agree with [25].

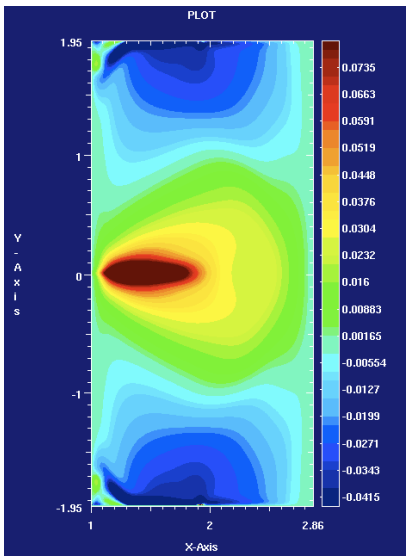

Figure 5.19: *Outflow* mid-plane jet: The poloidal circulation of the flow takes the form of two Ekman cells meeting in an *outflow* at the mid-plane, recirculating in a narrow *inflowing* jet close to the endcaps. These results agree with [59].

Ekman cell poloidal flow, but the two cells can meet either in an inflow at the mid-plane (Figure 5.18), or in the opposite sense (i.e., an outflow at the mid-plane, see Figure 5.19). In the first case, the results agree with the simulations described in [59]. These two opposite results seem to depend upon the fluid Reynolds number; unfortunately, the orientation of the radial component of the flow at the mid-plane in the experiment is still subject to investigations, since there is currently no possibility to determine the flow orientation in the experiment because the ultrasound velocimetry technique produces noisy results when directed radially inward (because of the reflection on the inner cylinder). Thus, the direct validation with experimental results is still missing, but there are plans to upgrade the device in order to allow the measurement of radial velocities at the mid-plane.

5.3.2 Scaling of the MRI Amplitude with Re

Following the investigation in [90], we also analyzed – by using `Heracles` – the scaling behavior of the MRI depending on the fluid Reynolds number Re. With our general approach, we used the fixed rotation speed configuration MRI-Z 100% at a constant applied magnetic field, so that $S = 2.3$. This

set-up corresponds to a fixed magnetic Reynolds number Rm of 15.3. We then varied the kinematic viscosity ν so that $2000 \lesssim \mathrm{Re} \lesssim 40,000$.

Figure 5.20 shows the time development of the MRI amplitude A for simulations with different fluid Reynolds numbers. This figure shows that the growth rates and maximum amplitudes are close to each other, whereas the saturated amplitude A_s strongly depends on Re. The two curves that seem to fall out of this scheme show a different behavior during the growth phase. The saturated value however blends in with the other simulations which is confirmed in the next figure. The reason for this behavior is probably an effect of the initial condition.

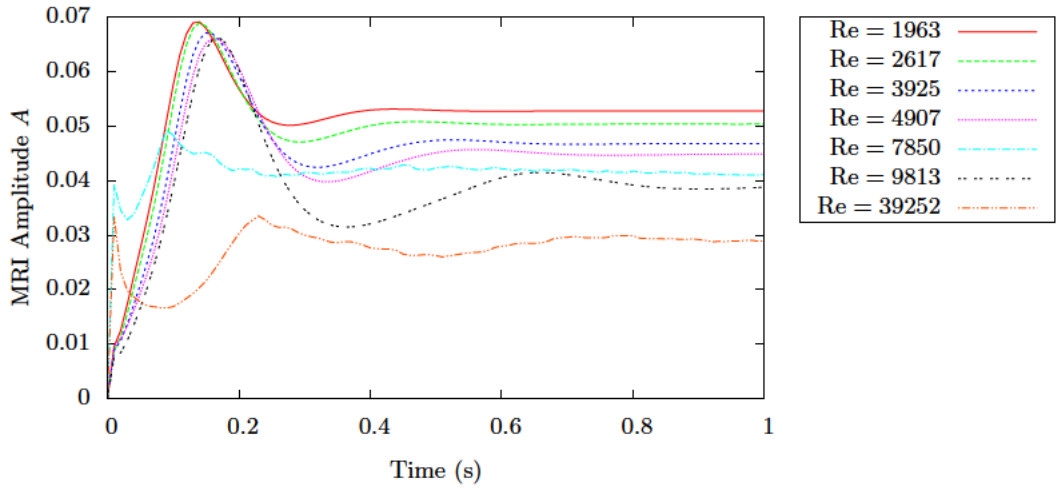

Figure 5.20: Time development of the MRI amplitude A for simulations with different Reynolds numbers Re at otherwise identical parameters with $S = 2.3$ and the MRI-Z 100% configuration. Picture obtained with `Heracles`.

In figure 5.21 we show the saturated MRI amplitude A_s depending on the fluid Reynolds number Re. A fit through the data points shows that the amplitude is scaling with a power law

$$A_s = a \cdot \mathrm{Re}^{-b} \,, \tag{5.1}$$

with $a = 0.24$ and $b = 0.20$, so $A_s \propto \mathrm{Re}^{-0.20}$. Extrapolating these results to the Reynolds numbers in the experiment with $\mathrm{Re} \approx 2 \cdot 10^6$ [75] provides an estimate for the expected amplitude in the experiment of approximately 1.3 %. This estimation blends in very well with the estimate we have just given in the section before. In other words, our results give an upper limit for the saturated MRI amplitude in the experiment of approximately 1.5 %.

Moreover, these findings present a similar scaling as in [90], where a scaling with $A_s \propto \mathrm{Re}^{-1/4}$, and a similar time dependence of the amplitude as we have shown in figure 5.20 has been reported. The difference between

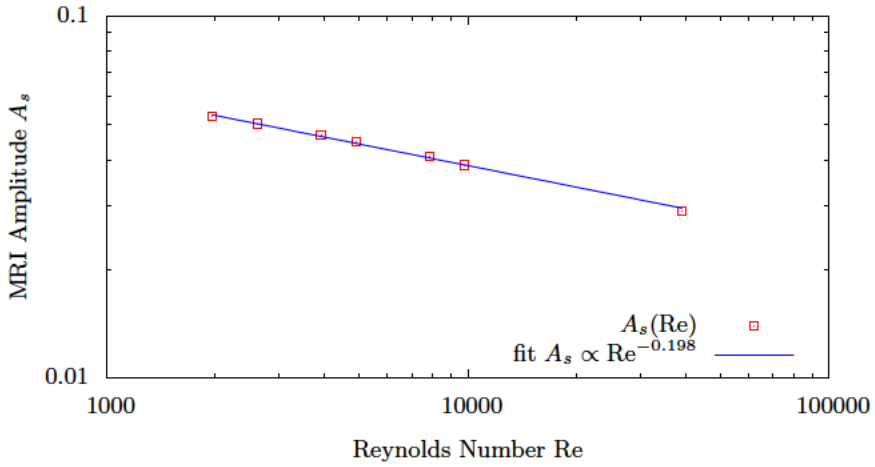

Figure 5.21: Scaling of the saturated MRI amplitude A_s with the fluid Reynolds number Re. The rotation speed configuration was MRI-Z 100%, the applied magnetic field was constant, with $S = 2.3$. Picture obtained with `Heracles`.

the exponent in the scaling relation can be explained by a slightly different configuration of the rotation speeds.

5.4 Conclusions and outlook

Numerical simulations with `SFEMaNS` and `Heracles` show promising results about the possibility of detecting the presence of the MRI. Target of this two-code approach was the investigation of the following topics: (i) Whether the azimuthal scaling can be reproduced with `Heracles` and `SFEMaNS`, and (ii) whether we were able to find out how a MRI mode would influence the scaling. The magnetic boundary conditions do not seem to be decisive here: `SFEMaNS` obtains very similar results with pseudo-vacuum and true-vacuum conditions (whereas `Heracles` is capable only of pseudo-vacuum at present). The rotation rate and the applied magnetic field B_z are the main variable parameters, upon which the MRI amplitude strongly depends. The main result of our analyses is that, by looking at strong departures from the self-similar profile of u_θ/u_1 as function of u_A/u_1, it can be possible – in the experiment – to detect possible influences of the MRI mode on the flow. Past numerical investigations were not able to find this scaling relation [75]. Furthermore, the simulations done by [90] showed that in the experiment the azimuthal velocity is only changed in the order of 2% for a fully saturated MRI amplitude. This value is on the same order of magnitude as the experimentally measured drift below the threshold for the MRI, which complicates the experimental identification of the instability [75].

In order to easily compare simulations and the experiment, we carried out numerical simulations with fixed Prandtl number. With this choice, we were able to follow the experimental procedure more closely, since, in the experiment, Pm is a material constant while the magnetic Reynolds number Rm is modified by changing the rotation rate. The Prandtl number has been chosen according to the available computational resources, keeping only the applied magnetic field and the rotation rates as free parameters. As conclusion of our numerical investigation we can note that we are able to reproduce the scaling relation as reported in [75], namely for small rotation rates (i.e., for small MRI amplitudes). Furthermore, for simulations with larger MRI amplitudes we find a strong correlation between the strength of the MRI and the deviation from the azimuthal velocity scaling. The fact that we do not observe a perfect collapse can probably be explained with the MRI threshold [75] that is expected in the experiment: opposed to the behavior in our numerical simulations where we find MRI also for infinitesimal applied fields.

Another difference with the experiment we observed is the slope of the scaled plots of the azimuthal velocities, since both `Heracles` and `SFEMaNS` foresee a smaller vale of the slope, most probably due to the higher viscosity in the simulations. Despite these differences we can conclude that – according to the numerical results – the azimuthal velocity scaling is indeed suitable to identify MRI modes and to measure their strength.

With the results of this investigation we can also give a rough estimate

for the upper limit of the MRI amplitude in the experiment. A comparison of the numerical with the experimental data suggests that the MRI amplitude in the experiment in [75] is less than 1.5 %, whereas a lower limit cannot be given with this method. In order to support this comparison we have additionally performed a series of simulations to analyze the scaling of the MRI amplitude with the fluid Reynolds number Re. We have shown that the MRI amplitude scales with $A_s \propto \mathrm{Re}^{-0.20}$. If the MRI amplitudes from our simulations are extrapolated to Reynolds numbers comparable to the experiment in the order of $\mathrm{Re} \approx 2 \cdot 10^6$, we get an estimate for the MRI amplitude of 1.3 %. Although both estimates are rather rough, they nevertheless provide a consistent prediction.

Further numerical explorations are needed, in order to firmly confirm (or rule out) this hypothesis. For instance, future simulations can study whether a local refinement of the numerical resolution near the endcaps and perhaps in the mid-plane "jet" has an impact on the results, since the coupling to the endcaps is responsible for the Ekman circulation in the first place. For reasons of computational performance, the resolution may be coarsened in the bulk, where stronger gradients of the physical quantities do not take place. Another possible direction for future investigations is to run simulations with `Heracles` by using as initial condition the "outflow" configuration calculated by `SFEMaNS`. To do this analysis, a mapping of the flow from the `SFEMaNS` grid to the `Heracles` one is needed. Similar efforts have been already put into this idea in [25], but it turned out the only way to produce an outflow (using only `Heracles`) was by changing the ratios Ω_i/Ω_1 ($i = 2, 3$ or 4). On the other hand, a two code approach is worth being explored on this topic.

On the experimental side, plans have been made in order to measure the radial velocity by installing two ultrasound probes in the same port; their beams would point at equal angles on either side of the radial line. In principle, the sum of the two channels should measure u_r (if it is axisymmetric), and the difference should measure u_θ. Moreover, the experimentalists have plans for sensors embedded in the flow (hence facilitating the measurements in the conducting fluid region), but these plans are still in formative stages.

If it will be confirmed that the departure from the self-similar profile is a sign of the presence of the MRI, this can be still not enough for a solid understanding of the phenomenon: The physical meaning of this self-similar behavior is still not clear, since this observation merely comes from the analysis of the experimental data. Further explorations of the parameter space with numerical simulations (but keeping the Prandtl number constant) can be a good strategy to gain insights into this unclear phenomenon. Moreover, future simulations can explore feasible ways of increasing the MRI amplitude in the experiment before these measurements will be physically implemented into the device.

An important difference between the experimental and the numerical

results is the slope of the scaled plots of the azimuthal velocities as functions of the applied field: Both `Heracles` and `SFEMaNS` predict a much smaller slope. We suggest that this discrepancy is a consequence of the high viscosity of the simulations. Nevertheless, we conclude that for our simulations the azimuthal velocity scaling is a suitable way to identify the presence of MRI modes, as originally supposed by the experimentalists [75].

Chapter 6

Quantifying turbulence in the dynamo experiment

> "Turbulence is the most important unsolved problem of classical physics."
>
> Richard Feynman

This Chapter deals with some of turbulent properties detected in the numerical simulations of the Madison Dynamo Experiment. The reason why turbulence plays a fundamental role in liquid metal experiments is the following. The magnetic Prandtl number Pm (i.e., the ratio of the kinematic viscosity to the magnetic diffusivity, or Rm/Re) associated with liquid sodium (the most common liquid used in such experiments) is of the order of 10^{-5}. Since the goal of the experiments is to sustain a dynamo, the threshold of the dynamo instability should be overcome, i.e., the magnetic Reynolds number should be larger than a critical value Rm_c. In turn, Rm_c is typically of the order of 10^2, hence $Re = Rm/Pm$ is of the order of 10^7 for liquid sodium. Such a huge number testifies that is impossible to avoid the development of turbulence in the flow. Hence, characterizing the intermittent properties is a crucial ingredient in the understanding of dynamo action and eventually take measures in the laboratory that can facilitate the onset of the dynamo instability. On the other hand, the presence of turbulent motions in the fluid usually hinders the dynamo process. This last consideration motivated us to investigate – via numerical simulations – more general properties of the turbulent motion in the Madison sphere. Moreover, characterizing the turbulence of the simulated system can be a good way to benchmark the simulations against the experimental data.

In particular, we focused our attention on the possible presence of intermittent behaviors in the MDE system. Intermittency is one of the most intriguing and measurable features of turbulence (for a brief introduction

to it, see 2.4.4). In analyzing the intermittent simulated data, it turned out that the choice of the inertial range (i.e., the range of scales between the scale of the forcing/boundaries and the viscous dissipation scale) could strongly influence our results (i.e., the determination of the scaling law of the structure functions, see below). In other words, with a suitable choice of the extrema of the inertial range, almost every possible result could be extracted from the data, making the analysis poor and arbitrary. In order to avoid this eventuality, we used a technique known as Extended-Self Similarity (ESS) [104–106], which allowed us to obtain a more unbiased analysis. This technique is still not fully understood by the scientific community, yet it is used in many other works; it has been originally developed for homogeneous isotropic turbulence in order to successfully characterize intermittent flows. We will show that not only this method surprisingly works with our data, but that it works also under circumstances in which it is not supposed to work, i.e., in anisotropic and inhomogeneous turbulence.

Needless to say, with our simulations we are not able to reach the fluid and magnetic Reynolds numbers of the experiment, nevertheless it is possible to provide quantitative analyses that can constitute a possible way to compare the real system and the simulated one in a more enlightening way. As already stated above, we use the `DYNAMO` code for this task, since this code provides a unique virtual laboratory, where the physics of a spherical, bounded system in the framework of dynamo theory can be explored.

Contents

6.1 Intermittency 81
6.2 Quantifying intermittency 82
6.3 Numerical setup 85
6.4 Results 86
6.5 Summary and conclusions 93

6.1 Intermittency

Turbulent flows exhibit sudden bursts of activity, especially at small spatial scales. This phenomenon is called *intermittency* and leads to departures from self-similarity and to non-Gaussian probability density functions of the velocity increments, with large central peaks and long tails. Intermittency can be detected in different contexts, such as the solar wind [47,49,107–110], or the interstellar medium [111, 112], as well as in laboratory experiments [107, 113] and numerical simulations [114–116]. This phenomenon is interpreted as an effect of spatially localized structures in the flow such as vortex filaments or current sheets [38]. In other words, turbulent systems show small-scale fluctuations whose statistics exhibit irregular features like

clumpy activity (i.e., irregular spatial distribution of regions where the energy is dissipated or flows from a scale into another). The self-similarity hypothesis, which describes the small-scale statistics of the signal by simply mapping the large scale statistics by a scale factor, does not take into account these irregular effects. In other words, the presence of intermittency in a turbulent system invalidates the hypotheses on which the Kolmogorov 41 phenomenology is based [34, 35].

While intermittency is well studied in the idealized situation of homogeneous isotropic turbulence (see [117] and references therein), there is also considerable interest in quantifying intermittency in flows that are closer to experimental and real-world scenarios. Dynamo experiments may serve as one prominent example for such systems. Here, turbulence is known to shift the threshold for self-sustained dynamo activity, as it has been demonstrated for different setups, both numerically and experimentally, by a number of authors [81, 97, 118–121].

We will proceed by first introducing the main statistical techniques in Sec. 6.2, before we describe the numerical setup in detail in Sec. 6.3. The main results of this study are presented and discussed in Sec. 6.5, before we conclude.

6.2 Quantifying intermittency

Intermittency in turbulent systems is often detected and characterized by studying the statistical properties of the *velocity increments* $\mathbf{u}(\mathbf{x} + \mathbf{r}, t) - \mathbf{u}(\mathbf{x}, t)$ or of the two-point correlation function $\langle \mathbf{u}(\mathbf{x} + \mathbf{r}, t)\mathbf{u}(\mathbf{x}, t)\rangle$, where $\mathbf{u}(\mathbf{x}, t)$ denotes the velocity field and the angular brackets denote averaging. In particular, the investigation described in this chapter is carried out by focusing on the so-called *structure functions*, i.e., the moments of the probability density function of the velocity increments.

It has been shown – experimentally and numerically – that, at high Reynolds numbers, structure functions of order p show an r^{ζ_p} scaling [37,38]. The results of experiments and numerical simulations show that the scaling exponents $\zeta(p)$ of the p^{th}-order structure function deviate from the scale-invariant exponent which is commonly referred to as *anomalous scaling* and the consequence of intermittency. In fact, the analysis of the $\zeta(p)$ exponents can reveal how much the spatial distribution of the energy dissipation is clumpy. If the decay of the vortices occurs in such a way that the vortices are teased out into finer vortices, the vorticity field becomes spotty, as well as the *enstrophy* scalar field, where the enstrophy is just defined as the squared modulus of the vorticity. Since the energy dissipation is proportional to the enstrophy, where the proportionality factor is the viscosity of the medium, then the spatial distribution of the energy dissipation ϵ will have the same degree of spottiness, therefore ϵ will be concentrated only into regions where

high the vorticity is high. Moreover the exponents of the velocity increment functions are correlated with the degree of spottiness of the small-scale structure of the fluid (see [33]), therefore those functions are a reasonable choice for measuring spatially intermittent turbulent behaviors. In particular, one can study the departure of the third-order structure function scaling law from the exact result, derived by Komogorov, that this function follows a linear scaling law. Indeed, from the Kàrmàn-Howarth equation (which describes the evolution of the two-point correlation function) it is possible to derive the *Kolmogorov equation*, which relates structure functions of order 2 and 3 (see, e.g., Ref. [122]). In turn, Kolmogorov equation, in locally isotropic turbulence and for r in the inertial range, predicts a linear scaling for the longitudinal third order structure function (the so-called *four-fifth law*).

Two kinds of structure functions are usually defined: the *longitudinal* $S_{p,L}$ and the *transverse* $S_{p,T}$ structure functions of order p, i.e.,

$$S_{p,L} = \langle \delta v_L^p \rangle \equiv \left\langle \left[\Big(\mathbf{u}(\mathbf{x} \ + \mathbf{r}) - \mathbf{u}(\mathbf{x}) \Big) \cdot \frac{\mathbf{r}}{r} \right]^p \right\rangle \tag{6.1}$$

and

$$S_{p,T} = \langle \delta v_T^p \rangle \equiv \left\langle \left[\Big(\mathbf{u}(\mathbf{x} + \mathbf{r}) - \mathbf{u}(\mathbf{x}) \Big) \cdot \hat{\mathbf{n}} \right]^p \right\rangle, \tag{6.2}$$

where $\mathbf{r}$ represents the separation vector while $\hat{\mathbf{n}}$ is a unit vector perpendicular to $\mathbf{r}$. In case of isotropic and homogeneous turbulence, we have that $S_{p,X} = (\mathbf{x}, \mathbf{r}) = S_{p,X}(r)$, where the subscript X represents L or T.

Due to the finite Reynolds numbers accessible in experiments and numerical simulations, methods have been sought after to more unambiguously characterize anomalous scaling. A significant improvement of the scaling exponent analysis can be given using an empirical technique, known as Extended self-similarity method (ESS, see [104–106]): Instead of considering the dependence of S_p on r, one usually considers the formula

$$|\langle (\delta v_X)^p \rangle| \propto |\langle (\delta v_X)^3 \rangle|^{\zeta(p)}. \tag{6.3}$$

Indeed, in the inertial range, it is expected that $S_3 \sim r$, according to the Kolmogorov four-fifth law; therefore, the generic $p-$th structure function has the same scaling exponent as a function of r or of the third-order longitudinal structure function. Eq. (6.3) can be generalized in the following way [123]

$$|\langle (\delta v_X)^p \rangle| \propto |\langle (\delta v_X)^s \rangle|^{\beta(p,s)}, \tag{6.4}$$

where $\beta(p, s) = \zeta(p)/\zeta(s)$. Recasting expression $|\langle (\delta v_X)^p \rangle| \propto r^p$ in this way has, as a consequence, that the relative exponents $\beta(p, s)$ are independent of the scale (over a broad range) even when the absolute ones are not, as frequently observed [124]. In other words, the motivation of the use of ESS is that the exponents $\zeta(p)$ can be computed – with a higher degree of accuracy

– as $\beta(p,3)$ using the rigorous result $\zeta(3) = 1$ derived by Kolmogorov, as already shown in Eq. (6.3), since these exponents are constant over a larger range of scales and not only in the inertial range [104, 123].

In this chapter, we present results obtained with a variant of the ESS, as originally done in Refs. [104, 105], i.e., by using alternative structure functions, defined with the absolute values of the longitudinal velocity increments,

$$S_{p,X}(r) = \langle |\delta v_X|^p \rangle. \tag{6.5}$$

As pointed out in [125], by using the absolute value, the scalings turn out to be better, but in this way there is no equivalent to the four-fifth law for the third-order structure function that can be used in order to convert relative exponents $\beta(p,s) = \zeta(p)/\zeta(s)$ into the absolute $\zeta(p)$ exponents. If the system shows this above-mentioned large independence of the scaling exponent on the scale, the estimation of the relative exponents is easier, since they are constant in the range $r \in [\eta, L]$, where η is the Kolmogorov dissipation scale. Moreover, it turns out that the relative exponents are independent of flow geometry and fluid Reynolds number, meaning that corrections to Kolmogorov's theory can already be addressed at low fluid Reynolds numbers. In [106] it is pointed out that this feature suggests that scaling and intermittency are concepts which are not specifically related only to fully developed turbulence but that can be found at relatively low fluid Reynolds numbers provided that the right recasting of Eq. (6.3) is performed.

In [123] and [106] the impact of inhomogeneity and anisotropy on the ESS technique are briefly discussed. The authors of these papers state that possible discrepancies between the results obtained from homogeneous system analyses and inhomogeneous ones could be observed (as in [126], where the range of validity of ESS is narrower respect to the expected one). Hence, inhomogeneous flows can show a reduced range of validity of ESS, due to boundary layer effects. Then, ESS should be applied far from the boundaries, where the velocity field shows a local homogeneity and isotropy. The boundary layer thickness (which is of the order of $L\ Re^{-1/2}$, see [18]) is a length scale larger than η (which is of the order of $L\ Re^{-3/4}$, according to Kolmogorov's theory) and this new scale could be able, in principle, to modify the ESS scaling. Experimental data measured closer to the boundaries seem to confirm this last statement [123]. It is therefore important to verify ESS in inhomogeneous, anisotropic systems with large shear flows, as suggested in [106]. As observed in [125], in spite of several attempts to explain the success of ESS (see, e.g., Refs. [44, 124, 127–130], ESS is still not fully understood. In the light of the discussion above, we stress the fact that the main scope of the work described in this chapter is to show that the ESS method can be successfully applied to the data that were numerically generated in order to model an experimental system characterized by

a strong inhomogeneity and anisotropy. Further outcomes of this analysis are discussed in Section 6.5.

The expression of the second-order structure function can be generalized to include the deviation from Kolmogorov scaling ($\zeta(2) = 2/3$) outside the inertial range. As stated in [131, 132], an example of such a generalization can be

$$S_2(r) \propto r^{2/3} f\Big(\frac{r}{\eta}\Big), \tag{6.6}$$

or

$$S_3 \propto r f\Big(\frac{r}{\eta}\Big), \tag{6.7}$$

where $f(r/\eta)$ is a dimensionless quantity – called *form function*. Comparing Eq. (6.7) with the Kolmogorov result $\zeta(3) = 1$, one should expect that the form function is of the order of unity in the inertial range. Keeping the ESS results in mind, a natural consequence of Eq. (6.7) is that it is possible to generalize the scaling properties of the generic p^{th} moment:

$$S_p(r) \propto \Big(r f\Big(\frac{r}{\eta}\Big)\Big)^{\zeta(p)}, \tag{6.8}$$

as suggested in [133].

6.3 Numerical setup

As already mentioned, the results presented in this Chapter have been obtained using the `DYNAMO` code. The simulations have a radial resolution $n_r = 512$, which means that the grid space between the mesh points in the radial direction is of the order of one millimeter. The angular resolutions of those simulations is $n_\theta = 80$ and $n_\phi = 160$ (respectively, the number of longitudinal and latitudinal grid points). The relatively high radial resolution was chosen in order to allow us to study – with the appropriate resolution – structure functions with the separation vector $\mathbf{r} \propto \mathbf{e}_r$ (see Eqs. (6.1) and (6.2)). For this reason, 50 points in the sphere are chosen where the time series of the velocity and magnetic fields are recorded. The coordinates of the first 25 points share the same colatitude and longitude $\theta = 90^\circ$ and $\phi = 0$, therefore in Eq. (6.1) the separation vector $\mathbf{r}$ lies in the equatorial plane, in the radial direction, i.e.,

$$\mathbf{r} \propto \hat{e}_r\Big|_{\theta=\pi/2,\phi=0}. \tag{6.9}$$

Adjacent points are separated by 10 grid points (about 1 cm) and this array of probes is located between $r_1 = 250$, i.e., about 25 cm (which corresponds to the reference probe at $\mathbf{x}$) and $r_2 = 500$, i.e., about 50 cm. The second array is also placed in the radial direction, between the same r_1 and r_2,

but at $\theta = 121^\circ$ and $\phi = 0$. In order to compute the transverse structure functions, we used $\hat{e}_\theta$ and $\hat{e}_\phi$ as the two independent transverse directions on the plane perpendicular to the separation vector (since in Eq. (6.2) we indicated a generic direction $\hat{n}$ on that plane). The choice of the location of the arrays is due the fact that similar locations are used in the MDE [81].

Seven kinds of simulation were performed. In the following table, their most important parameters are reported.

Run	Re_0	Rm_0	Re	Rm	U	$\mathcal{C}$
1	2000	40	1120	22	0.56	0.01
2	2000	40	1060	21	0.53	0.03
3	2000	40	820	16	0.41	0.07
4	2000	40	640	12	0.32	0.15
5	2000	200	540	54	0.27	0.01
6	2000	200	540	54	0.27	0.07
7	2000	200	540	54	0.27	0.15

The number $\mathcal{C}$ represents a dimensionless parameter proportional to the amplitude of superimposed magnetic field, whereas the numbers Re_0 and Rm_0 are numerical parameters read by the `DYNAMO` code before a simulation is started. By multiplying them with the characteristic velocity U, the fluid and the magnetic Reynolds numbers Re and Rm are obtained. The reduction of the characteristic velocity U when stronger background magnetic fields are applied – as shown in the table – is due to the amplification of Lorentz force effect, leading the run into a non-kinematic regime.

6.4 Results

In this section, we discuss the results of the simulations, focusing our attention in particular on the application of the techniques described in section 6.2. It turns out that analyzing the data by means of the plain structure functions does not lead to clear conclusions, since the determination of their scaling exponents is an operation that is biased by the identification of the inertial range. In other words, the results obtained by analyzing the structure function behavior are not robust enough and can lead to misleading conclusions. On the other hand, the sound achievement of the work described in this chapter is that the ESS represents a valuable way of letting the data collapse on straight lines over a range that is to be way larger than the relatively narrow inertial range. It is worth emphasizing, however, that this method does not solve once and for all the identification of the absolute exponents of the structure function scaling laws; on the other hand, this technique turns out – unexpectedly – to work notwithstanding the presence of strong inhomogeneities and anisotropies. As stated in Section 6.2, one of the main motivations of this analysis is that it is important to verify ESS

in inhomogeneous, anisotropic systems, because, for instance, the boundary layer – whose thickness is larger that the Kolmogorov dissipation scale – could negatively affect the applicability of ESS. On the contrary, the system we study provides a new example of inhomogeneous and anisotropic system where the ESS technique turned out to be crucial for extracting the statistical information from the data. In the following, we describe in more details the outcome of the analysis.

Plain structure functions.– Following Kolmogorov's standard analysis, a rough estimate of the viscous dissipation scale is

$$\eta \sim L\ Re^{-3/4}. \tag{6.10}$$

Since for our system $L \sim 0.53$ m (the radius of the MDE sphere), the dissipation scale turns out to be about 3 or 4 mm for the typical Reynolds numbers of the simulations. In consequence, to be sure that the calculation of the scaling exponents was not affected by viscous effects which take place at small scales, we have not considered values of r below $\sim 10\eta$. In fact, Stolovitzsky et al. [134] pointed out that the transition from dissipative to inertial regimes occurs at $r/\eta \gtrsim 11$. Th results show that a (Taylor expansion) dependence up to 30 mm ($\log_{10} r/\mathrm{mm} \simeq 1.5$) is observed – confirming this previous estimation about the viscous range – and a range of approximately constant scaling can be identified between ~ 60 and 110 mm. The interval where the scaling exponents are calculated goes from 30 up to usually 70-80 mm. Considering further points negatively affects the quality of the calculation, as an effect of inhomogeneity due to the force term in the governing equations. The central outcome of this analysis clearly shows that the forcing and the dissipation scales are too close to each other to extrapolate scaling laws of the structure functions.

Use of ESS.– In the following, we use $\zeta(3)$ as the reference exponent, since it can be shown that $\zeta(p)/\zeta(3)$ turns out to be scale independent for low orders and on a larger range [135] and because $\zeta(3) = 1$ exactly in 3D Navier-Stokes turbulence. The error bars of the exponents are calculated via a standard linear regression of the data in a log-log plane using a least-squares method provided by GNUPLOT (see [136]). As an estimate of the fitting procedure error, GNUPLOT reports the standard deviation of the fitted curve σ which is defined as the rms of the residuals. By using geometrical considerations on the growth rates of the magnetic energy, it can be shown that the error on the slope of the curve (slope which corresponds to the exponents we are calculating) is $2\sigma/\Delta x$, where Δx is the length of the range of the independent variable on which the fit is performed. Figures 6.1 and 6.2 show how ESS-corrected structure functions appear. It is clear, therefore, that with this method we can fit a straight line with great accuracy to the functions $\log\langle|\delta u_r|^p\rangle$ with the dependence described by Eq. (6.3). Our results are in line with what the investigations of [104] show: the slopes of

the various curves (i.e., the relative exponents of the structure functions) are constant over the whole range of variation of the separation r. In Section C a detailed overview of the results is shown in tabular form, where the exponents in the tables are all calculated by means of ESS, which turns out to work in every case and providing small uncertainties. The results obtained with the use of ESS analysis are discussed in Section 6.5.

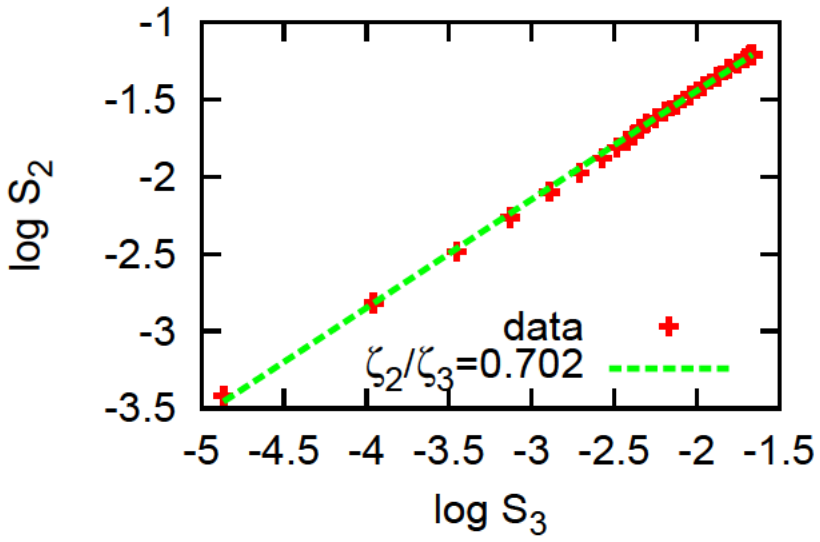

Figure 6.1: Third-order longitudinal structure function vs second-order longitudinal structure function (log-log) for run number 4, $\theta = 90°$. One can visually appreciate how powerful ESS turns out to be, since the range of constant scaling extends over the whole range of separation vector available to the numerical experiment.

Form function.– We use the simulated data to analyze the properties of the form function. Then we extend the array of probes to the inner part of the sphere too (from $r_i = 10$ cm up to $r_i = 50$ cm, every 10 mm) and perform a simulation with an intermediate magnetic field $\mathcal{C} = 0.07$ (see Figure 6.3).

A qualitatively similar result concerning the shape of the form function can be found in [133], where experimental studies were performed for fluids of different Reynolds numbers. As Fig. 6.3 shows, the form function turns out to be independent on the order p. Although the secondary bumps shown by the form function cannot be easily explained, this result confirms that our spherical, bounded, anisotropic flow –immersed in a weak magnetic field – shares properties of real fluids studied in different geometries.

Time intermittency.– As our numerical setup is motivated by the MDE experiment, we also seek for an evaluation of our data that can be compared to experimental measurements. True multi-point measurements are experi-

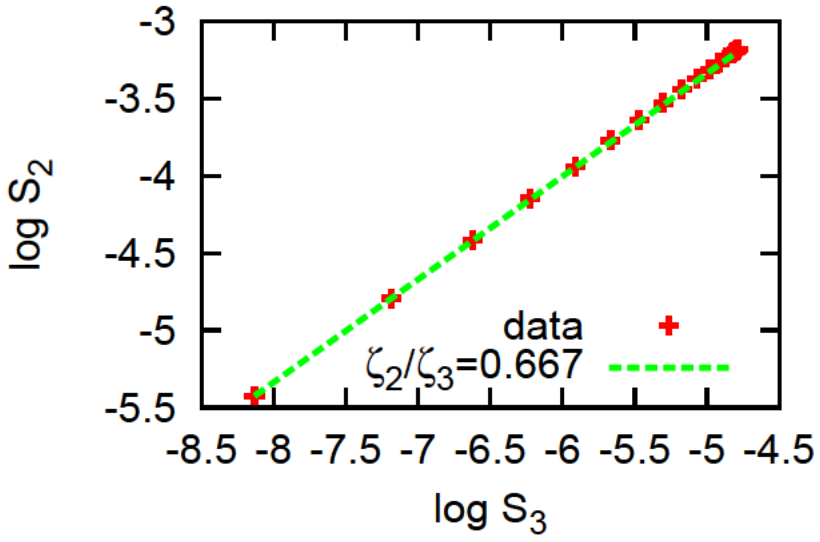

Figure 6.2: Third-order longitudinal structure function vs second-order longitudinal structure function (log-log) for run number 6, $\theta = 90°$. As above, the calculation of the exponent $\zeta(2)/\zeta(3)$ (the slope of the fitted line) is visibly improved.

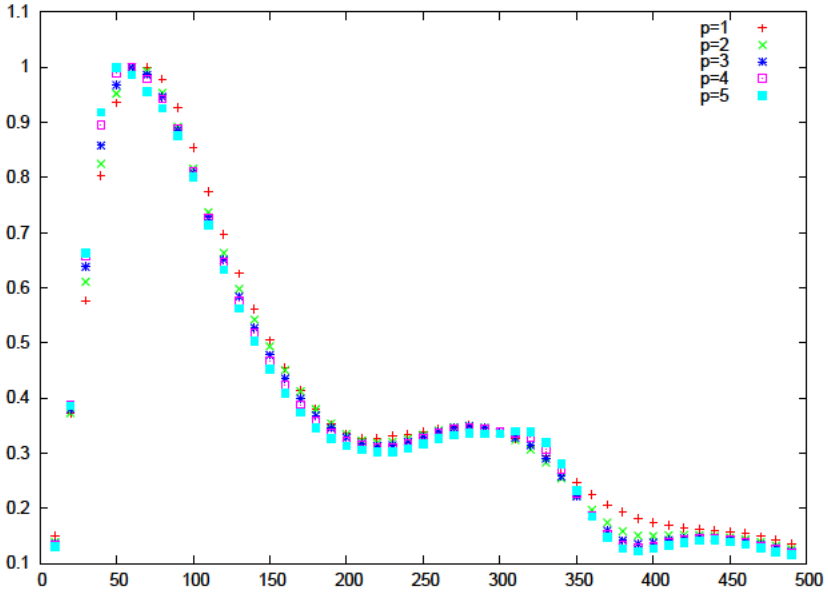

Figure 6.3: Form function vs separation, $\mathcal{C} = 0.07$, $\theta = 90°$. The form function is equal to 1 in what can be identified as the inertial range.

mentally hard to realize, which is why often temporally resolved single-point measurements are taken. This method is used also for solar wind observations, where the data are measured by a single satellite which does not have the possibility to spatially cover the large scales which characterize the solar wind; instead, it focuses on the temporal analysis of the turbulence advected by the solar wind towards the location of the satellite. The single-point measurements then can be related to multi-point measurements by some additional assumptions like Taylor's frozen flow hypothesis or the random sweeping hypothesis by Tennekes and Kraichnan. For the present investigation it turns out that ESS can also be detected in the temporal signals. In formulas, the temporal structure functions of order p is

$$S_p(\tau) = \langle |v(t+\tau) - v(t)|^p \rangle, \tag{6.11}$$

where τ is the temporal separation of the two recordings. As an illustrative example, in Figure 6.5 we show the structure functions of order p of the *magnitude* of the velocity field versus the temporal separation τ in a log-log plot for run number 2 at the location $\theta = 121°$, $r_1 = 400$, $\phi = 0$. A linear phase can be distinguished when τ is less than about 6 times the diffusivity time τ_σ and it demonstrates and quantifies the presence of a memory effect of the signals (related to the effects of viscosity).

The same data showed in Figure 6.5, are re-plotted versus the generalized coordinate S_3 in Figure 6.6, according to the ESS technique. This plot shows how strongly we can improve the robustness of the evaluation of the scaling

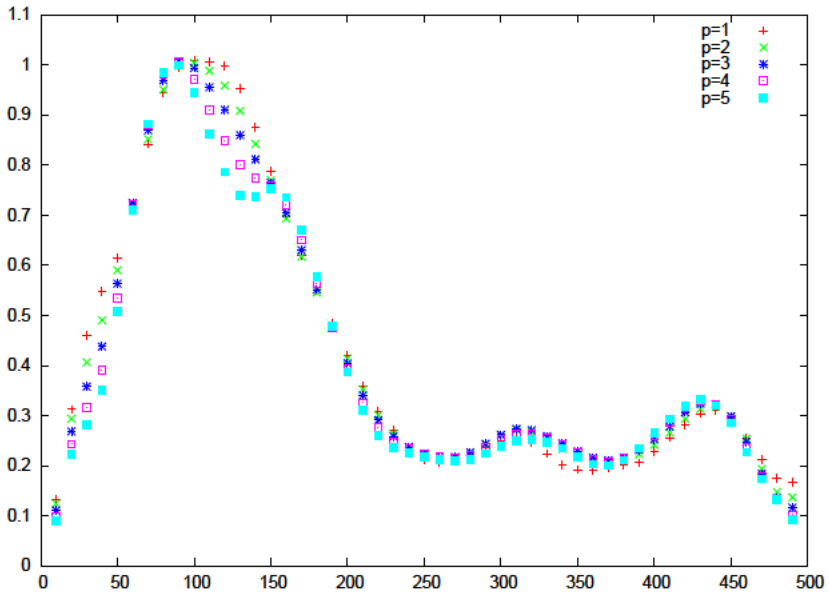

Figure 6.4: Form function vs separation, $\mathcal{C} = 0.07$, $\theta = 121°$.

exponents, since they are evaluated via a linear fit of the logarithm of the independent and dependent variables. In Appendix D, we reported the calculated relative exponents $\zeta(p)/\zeta(3)$ for two points at $\theta = 121°$, precisely at $r_i = 250$ and at $r_i = 400$. The results show a strong deviation from the Kolmogorov prediction in most of the cases, although we observe non-intermittent signals for some runs.

The similarity of these results to those in [137], obtained from edge plasma turbulence is noteworthy. The exponents of the temporal analysis are shown in tabular form in Section D. As well as in the spatial case, all the exponents are calculated exploiting the ESS method. In the tables, r_{probe} indicates the radial location of the probe where the simulated temporal signals are measured.

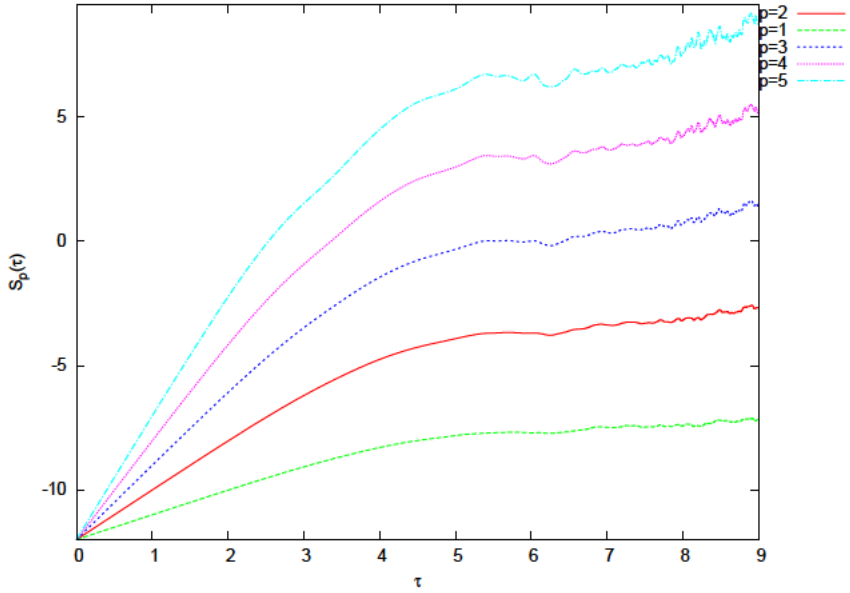

Figure 6.5: Structure functions of order p of the magnitude of the velocity field versus the temporal separation τ in a log-log plot for run number 2 at the location $\theta = 121°$, $r_1 = 400$, $\phi = 0$ (since the latitude is the same used also in the MDE). The scaling is linear when τ is less than about 6 times the diffusivity time τ_σ, and this proves the presence of memory effect of the signals.

Scaling properties of the Elsässer variables.– An analysis similar to Kolmogorov's was carried out for magnetohydrodynamics (MHD) by Iroshnikov [40] and Kraichnan [39]. The considered fields are the symmetrized Elsässer variables $\mathbf{z}^{\pm} = \mathbf{u} \pm \mathbf{B}$, where $\mathbf{B}$ is the normalized field $\mathbf{B}/\sqrt{\mu\rho}$. It can be shown that for the study of the scaling exponents, the superscripts $\pm$ of the Elsässer variables are unimportant; in the following we will drop them, using for the calculations the variable $\mathbf{z}^{+}$. The theoretical studies of

Kraichnan and Iroshnikov take into account the different mechanism of the energy cascade due to the presence of the magnetic field and starts from the hypothesis of scale independence of the energy dissipation. This set of hypotheses leads to the equations

$$\langle (\delta z_L)^p \rangle \equiv \left\langle \left| \Big(\mathbf{z}(\mathbf{x}+\mathbf{r}) - \mathbf{z}(\mathbf{x}) \Big) \cdot \frac{\mathbf{r}}{r} \right|^p \right\rangle \propto r^{\zeta_p}, \quad \zeta_p = \frac{p}{4}. \tag{6.12}$$

It can be shown that, starting from these equations, the energy spectrum presents the scaling $E_k \sim k^{-3/2}$ instead of the Kolmogorov $E_k \sim k^{-5/3}$ prediction. The Iroshnikov-Kraichnan spectrum can be observed in direct numerical simulations of 2D MHD decaying turbulence at moderate Reynolds numbers (lower than ours, see [138]). Higher Reynolds number simulations [139] or satellite observations of MHD turbulence in the solar wind [47–49] emphasize that the Iroshnikov-Kraichnan scaling should be modified in favor of nonlinear models of the functions $\zeta(p)$ [46, 50, 52, 53]. Since we are dealing with 3D MHD simulations, we should compare our results with those of works like [140] or [141], highlighting that – in our case – we model the stirring in such a way in order to mimic the real stirring in the MDE, leading to an inhomogeneous and anisotropic force term in the equations. Exploiting again the ESS technique but using $\zeta(4)$ as a reference exponent (according to [39, 40, 50] this exponent is expected to be close to unity), we perform a simulation with $\mathcal{C} = 0.07$ and $Rm_0 = 40$. In

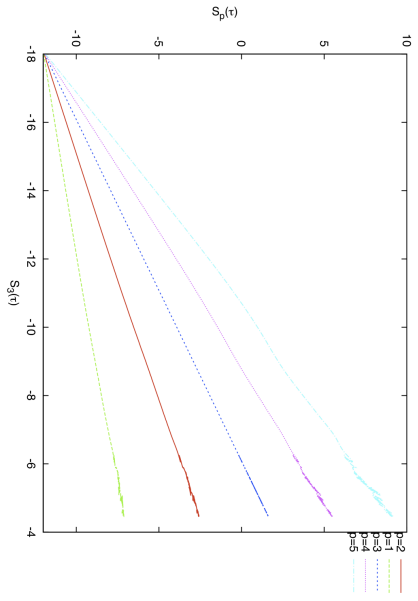

Figure 6.6: The same data showed in Figure 6.5, here plotted versus the generalized coordinate S_3, according to the ESS technique.

this case we take into account the inner part of the sphere too: Previous simulations [98] in fact suggested that a large value of the magnetic field can be observed in the inner core and in order to have a **B** amplitude comparable with the **u** amplitude, we prolong our two arrays from the center up to the 50 cm. Results can be seen in Tables 6.1 and 6.2, along with a model developed independently by Grauer, Krug, Marliani [50], and Politano and Pouquet [51] (we will call it the GKMPP model in the following). This model has the advantage to give predictions without any use of adjustable parameters. It was developed as an extension of the She & Lévêque model to MHD using the same Iroshnikov-Kraichnan hypothesis on the temporal scale of the energy transfer (which differs from the Navier-Stokes one). It should be emphasized again that these results do not give us information about the absolute exponent $\zeta(4)$, for which the expectation $\zeta(4) = 1$ is wrong, as pointed out in [141].

Table 6.1: Relative exponents of the structure functions of the Elsässer variable $\mathbf{z}^+$, $\theta = 90°$.

	longitudinal ($\hat{e}_r$)	transverse ($\hat{e}_\theta$)	transverse ($\hat{e}_\phi$)	GKMPP	$p/4$
ζ_1/ζ_4	0.279 ± 0.013	0.285 ± 0.003	0.34 ± 0.03	0.284	0.25
ζ_2/ζ_4	0.533 ± 0.017	0.536 ± 0.004	0.61 ± 0.04	0.543	0.5
ζ_3/ζ_4	0.769 ± 0.013	0.7714 ± 0.0022	0.82 ± 0.03	0.780	0.75
ζ_5/ζ_4	1.234 ± 0.021	1.225 ± 0.003	1.17 ± 0.04	1.204	1.25

Table 6.2: Relative exponents of the structure functions of the Elsässer variable $\mathbf{z}^+$, $\theta = 121°$.

	longitudinal ($\hat{e}_r$)	transverse ($\hat{e}_\theta$)	transverse ($\hat{e}_\phi$)	GKMPP	$p/4$
ζ_1/ζ_4	0.289 ± 0.011	0.292 ± 0.008	0.30 ± 0.03	0.284	0.25
ζ_2/ζ_4	0.540 ± 0.012	0.544 ± 0.009	0.55 ± 0.03	0.543	0.5
ζ_3/ζ_4	0.775 ± 0.008	0.777 ± 0.006	0.78 ± 0.02	0.780	0.75
ζ_5/ζ_4	1.220 ± 0.010	1.218 ± 0.009	1.22 ± 0.03	1.204	1.25

6.5 Summary and conclusions

The main motivation of our study was the quantitative characterization of a turbulent system that was originally designed for triggering the growth of a magnetic field in an optimal way. It is known, indeed, that turbulence in liquid metals obstacles this process. One possible way to study this problem is the precise spatio-temporal characterization of the eddies that play a detrimental role for dynamo action [120,121]. Another, more general way to face this problem is to search for possible hidden symmetries of the turbulent

flow, as the investigation of the scaling properties of the structure functions can provide. The goal is threefold: (i) Testing existing models in order to understand what kind of turbulent behavior is taking place in the system under study (e.g., the She & Lévêque model, the Politano & Pouquet model, etc); (ii) testing different techniques used under other sets of hypotheses in order to suggest to the experimentalists how to extract the information from the data (e.g., ESS, characterization of the *form function*, etc); (ii) Providing numerically generated data that can be directly compared to the ones obtained by the MDE. Let us discuss in more detail these three points.

Concerning point (i), we have found that our system shows features that are best described by models like those proposed by She & Lévêque (for hydrodynamic investigations) or by Grauer, Krug, Marliani, Politano and Pouquet (for MHD intermittency, [50, 51]). These models turn out to be good references for the predictions of the departure of the results from the homogeneous and isotropic theory in the MDE simulated system. The reason why we performed this structure function analysis lies in the fact that the study of scaling exponents is a standard way to characterize the intermittent properties of the turbulent system. Since different models have been elaborated for describing intermittency, it is important to compare them to our findings.

In addition to these considerations, let us stress that the main result of our study concerns point (ii). Indeed, we have shown that it is possible to successfully make use of a set of methods that are conceived for homogeneous and isotropic systems. A sound proof of why these techniques can be applied to this system is still lacking. A possible explanation can be given in light of the interpretation described in [142], although further analyses should be carried out in order to benchmark the formulas therein against numerically simulated data. In fact, in the present context, the major obstacle to having a clear characterization of the turbulent behavior is the fact that a reliable measurement of the *absolute* exponents of the structure functions is not possible, due to the narrowness of the inertial range. This problem is usually overcome with a questionable identification of the inertial range, i.e., considering the Kolmogorov's prediction $\zeta(3) = 1$ valid, irrespective of the width of the interval where this scaling can be observed. In order to overcome this issue, we exploited the Extended Self-Similarity technique, i.e., adopting the point of view of the relative exponent measurement. This method makes the calculation more unbiased, since the results do not depend on the identification of the inertial range.

The exponents we find via ESS turn out to be very similar to the predictions of models used for investigations in periodic box simulations. In fluid turbulence, She & Lévêque [52] and Dubrulle [143] postulated that the ESS method works thanks to a hidden symmetry of the Navier-Stokes equations. The usefulness of ESS was already discussed by [108] and [144] for MHD turbulence or by [145] and [137] for edge plasma turbulence of fusion

devices.

The simulations show that MHD effects must be taken into account when the magnetic field amplitude is higher, as found in the core of the sphere where a strong magnetic field can be detected ($B \sim 10B_{applied}$). Under these circumstances, the combined fields $\mathbf{z}^{\pm} = \mathbf{u} \pm \mathbf{B}$ turn out to be more suitable for the study of scaling laws. Again, ESS allows us to quantify the scaling laws of these fields. The scaling behavior is more similar to that predicted by the GKMPP model than to the standard Iroshnikov-Kraichnan $p/4$ scaling, due to the impact of inhomogeneity and anisotropy of the system. The justification that the Iroshnikov-Kraichnan theory turns out to be inaccurate can be found in [54,55]. Those effects can be described, within the statistical uncertainties, by means of a non-linear model (i.e., the GKMPP model) which departs from the prediction of the Iroshnikov-Kraichnan theory, quantifying the deviation from self-similarity and again confirming the presence of intermittency.

We investigated the *form function* of the structure functions too. The qualitative shape of the simulated form function $f(r/\eta)$ resembles that found in wind-tunnel experiments [133], although the experiments have a completely different geometry and different fluid Reynolds numbers, enforcing the original hypothesis that this function carries universal properties. Moreover, the form function does not depend on the exponent p, as shown also by the experiments. Further investigations on the physical meaning of this function are hence needed.

Another sound finding concerns the investigation of time intermittency as well, which we detected by applying again the ESS technique, by analyzing the temporal behavior of the fields in specific locations. Also in this case, the best way to characterize intermittency is by means of ESS, which turns out to be a crucial tool, without which a robust estimation of the exponent and the detection of time intermittency would be technically difficult. The outcome (i.e., the ESS can be applied to the temporal analysis) can facilitate the comparison with the experiment (point (iii)). Indeed, the reason why we check whether we can apply ESS to the temporal domain is that in the experiments it is easier to measure a temporal signal with a single probe than with an array of probes registering several signals at the same time at different locations for spatial analyses. In other words, we suggest to the experimentalist to accomplish the same kind of analysis and to see whether the same behavior can be detected. Characterizing which kind of intermittency takes place in the experiment can give further insights into the understanding of the system and can represent a new step towards the control of turbulent effects that hinder dynamo action.

Chapter 7

Facilitating dynamo action via turbulence control

As already mentioned in previous chapters, the identification of flow geometries and topologies that are optimal for the attainment of a magnetic instability is crucial [146, 147]. In order to achieve the dynamo mechanism, experiments are focused on the investigation of the optimal setup which enhances the probability of achieving dynamo action. The design of the geometry, the choice of the fluid, the forcing mechanism, as well as the boundary conditions and their material (for plasma dynamo experiments, see [148]) play a crucial role in creating a flow field whose geometry provides the right feedback mechanism for the creation of a self-sustaining magnetic field. However, the design of the geometry of an experiment is not enough for such a task because one should take into account also the detrimental effects that turbulence has on the dynamo process, as recent experimental investigations [81,119] have shown. In [84] it is experimentally observed that turbulence enhances the magnetic diffusivity of the liquid, an effect that hinders dynamo action. The effects of turbulence have also been investigated via numerical simulations: A fundamental work is described in [118], which studied whether turbulence (in a Taylor-Green flow and in periodic boxes) raises or lowers the dynamo threshold (i.e., the so-called critical magnetic Reynolds number Rm_c, above which the magnetic field growth takes place). The main result of [118] is that the addition to the mean velocity field of a large-scale stochastic noise significantly increases the threshold, whereas for small-scale noise, the results depend on the correlation time of the noise and the magnetic Prandtl number (the ratio of the magnetic to the fluid Reynolds number).

Keeping these results in mind, one of the natural interpretations of the fact that the Madison Dynamo Experiment has not yet achieved self-excitation is that the rather high observed fluctuation level of large eddies has played this detrimental role. It should be noted, in fact, that the mean

flow of this experiment is supposed to be optimal for dynamo purposes (according to [80]), hence it is hypothesized that the fact that the instantaneous flow can differ significantly from the mean flow is the reason of that failure. In order to make the instantaneous flow closer to the mean flow which favors dynamo action, an axisymmetric equatorial baffle (or annulus) near the boundaries has recently been added to the MDE.

This Chapter deals with our first attempts to reduce the influence of turbulence on the dynamo process. Although the results presented in this Chapter do not give us a positive answer, this part of the analysis turned out to be useful in the Chapter 8, where a more successful strategy has been proposed to the experimentalists. Moreover, this first failure has been the crucial step that fostered us to use a more powerful technique, the Singular Value Decomposition technique, as described in Chapter 8

Contents

7.0.1 Suppression of large-scale eddies in the MDE . . . 97
7.0.2 Suppression of the turbulent resistivity 98
7.1 Role of the baffle in numerical simulations . . . 99
7.1.1 Implementation of the equatorial baffle in the spatial domain 100
7.1.2 Implementation of the equatorial baffle in the spectral domain 103
7.2 Summary and interpretation of the results . . . 109

7.0.1 Suppression of large-scale eddies in the MDE

After the introduction of the equatorial baffle in the MDE, new measurements of the magnetic modes on the surface of the sphere were performed and these measurements were compared in turn to the ones obtained without the baffle [81]. From this comparison, it is hence possible to identify which interactions of the bubble diagram are more affected by the baffle. In other words, it is possible to identify these three-wave interactions which are suppressed by the presence of the baffle. It turns out that the velocity modes which are more weakened are s_1^0 and t_1^1. We emphasize that this last deduction is indirect, i.e., it is based on the assumption that the nonlinear interactions among the magnetic and the velocity modes follow the bubble diagram suggested by the Bullard-Gellman formalism. According to the results, these two modes are the most significantly damped modes, while the small scales (high l numbers) are almost unaffected by the baffle. The eddies associated with s_1^0 and t_1^1 would flow across the equatorial baffle, as can be seen in Figures 7.1 and 7.2. These two figures show a graphical representation of the velocity field lines of two eddies described by s_1^0 and

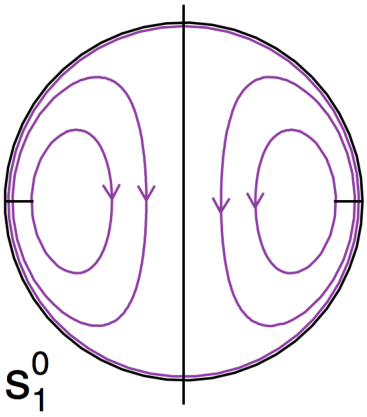

Figure 7.1: Eddy associated with the Bullard-Gellman function $s_1^0(r)$. Reprinted figure with permission from [81].

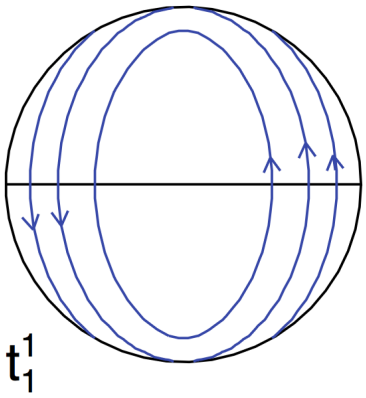

Figure 7.2: Eddy associated with the Bullard-Gellman function $t_1^1(r)$. Reprinted figure with permission from [81]

t_1^1: they form a shear layer adjacent to the boundaries of the sphere which flows perpendicularly through the equatorial plane.

7.0.2 Suppression of the turbulent resistivity

A second effect of the baffle which has been detected experimentally is the reduction of the 'global' *turbulent resistivity* (or *turbulent magnetic diffusivity*).

The mean field theory (MFT) predicts in fact that the turbulent fluctuations of **u** and **B** lead to an alteration of the *resistivity* or *magnetic diffusivity* η [30]. It can be shown within the framework of this theory that the modified quantity, η_{eff}, is larger than the molecular one, η; specifically, the relation is $\eta_{eff} = \eta + \eta_T$, where η_T is called *turbulent resistivity*. If – as just stated – the effective resistivity is *larger* than the molecular one, it means that the effective magnetic Reynolds number Rm_{eff} is *smaller* than Rm by a factor of η/η_T. In consequence, the dynamo excitation threshold is enhanced and more difficult to reach. The main goal of the suppression of the turbulent energy by means of an equatorial baffle can hence be viewed as the reduction of the turbulent resistivity, lowering dynamo threshold. The mathematical explanation of this effect from the MFT point of view has been described in Chapter 2.

As stated above in this section, the experiments show that this baffle is able to reduce the amplitudes and the fluctuation levels of large eddies, whose spatial extent is of the order of the experimental device itself. It can be shown that – as a consequence – the final effect is a global reduction of the turbulent resistivity. In fact, since the spectrum of the turbulent *s2t2*

flow (driven by a large scale force peaked at $l = 2$) drops off rapidly with l, the fluctuations at low l mainly contribute to the turbulence, whereas high l play only a minor role. In other words, large scale eddies usually carry most of the turbulent energy in this flow. Consequently, they are expected to be the main source of turbulent resistivity η_T. Suppressing them, the global value of η_T is reduced.

7.1 Role of the baffle in numerical simulations

In order to mimic the influence of the equatorial baffle in the MDE, we implemented in the `DYNAMO` code a model which operates on the spatial fields or on the spectral fields or on specific large eddy modes. As already stated, a reduction of shear layer fluctuations by an equatorial baffle has already been observed in water experiments with similar geometry [58, 149]. This method seems to be capable of improving the probability to exceed the critical magnetic Reynolds number as results of other works suggest.

Before proceeding further, as already stated in previous section, a warning is necessary. Numerical studies of Laval *et al.* [118] show indeed that large-scale noise tends to increase the dynamo threshold, suggesting thus that in an experiment, it is crucial, for dynamo action to occur, to control the large scale fluctuations, trying to keep them as stationary as possible. Nevertheless, we should be very mindful of the fact that in [81], MFT is used, applying its results to systems where large scale turbulence can play a fundamental role, although one of the basic assumptions of MFT is – as already pointed out – that the characteristic time and length scales of the fluctuations are *small compared with those of the mean fields*. If we suppose – as we did – that large eddies on the scale of the diameter of the spherical system are capable of carrying most turbulent energy, we are implicitly assuming that the correlation length can be large as the system size; in consequence, the calculation of the order of magnitude of α or β could be in principle not exact or even misleading, since these quantities could be not able to describe fully and meaningfully the effect of turbulence on the MHD system under consideration.

In order to study all these aspects via numerical simulations, several runs were performed with the purpose to investigate an impact of this baffle on the dynamo threshold. The first one is the implementation of a baffle in the spatial domain, slightly modifying the field at every time step. The second method is an implementation of the same effect of the spectral field by a modification of the toroidal modes which can be responsible of the large-scale fluctuations observed in the experiment. This procedure exploits the particular expression that the toroidal field has, i.e., the relation between the θ component of the toroidal velocity field and the toroidal spectral functions $t_l^m(r)$. In particular, the toroidal mode $t_1^1(r)$ is the main mode which

is subjected to this modification. The third baffle model is a spectral modification of the predicted flow, by zeroing out all the responsible modes of the shear layer. A forth and final implementation uses a single mode zeroing procedure: At every time step, single selected shear layer modes are zeroed out. These four implementations are described and studied in detail in the next subsections.

We chose to implement four different models of the baffle because every one of these four has its pros. For instance, the first implementation – in the spatial domain – is the most natural to design, since it operates directly on the flow in order to suppress the motion through the equatorial baffle near the boundaries. On the other hand, the implementations in the spectral domain are conceptually simple, since they use the Bullard-Gellman decomposition and permit to modify the profiles of specific modes. Moreover, the use of a "spectral baffle" gives us the possibility to mimic more easily the observed effects of the baffle in the MDE, since, in the experiment, indirect measurements of the amplitude of the most important modes are performed and then compared to the ones obtained without the use of the baffle [81]. By making use of these different advantages of the four approaches, we want to ensure the robustness of our results.

7.1.1 Implementation of the equatorial baffle in the spatial domain

The first type of model is a modification of the computed velocity field. As is explained in [81], the large-amplitude fluctuations of the shear layer modes that we are trying to suppress are well captured, to lowest order, by the t_1^1 and s_1^0 modes, i.e., large eddies with a prominent θ component on the equatorial plane, near the boundaries. In the code, a spatially smooth suppression of this component was performed at every time step as a filter on the predicted velocity field. More precisely, the z component of the field was damped on the equatorial plane, near the boundaries, according to

$$\mathbf{u}(r,\theta,\phi) \to \mathbf{u}(r,\theta,\phi) - v_z f(r,\theta,\phi)\hat{\mathbf{z}},$$

where the function f carries the spatial information of the damping mechanism. In order to avoid abrupt damping effects and steep gradients in the simulations, the function f employs Gaussian functions to describe the transition between the region where the damping effect is present and the region where it is not. In fact, it turned out that this Gaussian approach is well suited to avoid numerical instabilities. In conclusion, the functional form of f was chosen as

$$f(r,\theta,\phi) = \exp\{-\frac{r^2\cos^2\theta}{2\sigma_z^2}\} f_{ring}(r,\theta,\phi),$$

where, in turn,

$$f_{ring} = \begin{cases} \exp\{-[(r\sin\theta - \rho_{ring})^2]/(2\sigma_r^2)\} & r\sin\theta < \rho_{ring} \\ 1 & r\sin\theta > \rho_{ring} \end{cases}$$

The interpretation of the adjustable parameters σ_z, σ_r, and ρ_{ring} is as follows. The first parameter, σ_z, is a measure of the thickness of the baffle; σ_r represents a damping parameter along the radial direction; ρ_{ring} is a measure of the difference of the radius of the sphere and of the radius of the baffle (in the experiment, it is 8 cm). Since the MDE has focused the attention on the reduction of the turbulent resistivity (and hypothetically on the reduction of the threshold, if we follow MFT results, see previous sections), we can use our simulations to shed light on the impact of such a baffle on the dynamo growth rates and on the dynamo threshold. The reason why we implemented the filter with such a particular spatial shape can be understood by inspecting the spatial behavior of the eddies we are trying to influence (to have a graphical clue, see Figure 1 in [81]).

From first tests, it turns out that the main adjustable parameter is the "baffle width", i.e, the difference between the sphere radius and ρ_{ring} (in the MDE, it is 8 cm). A series of 23 runs was performed, as indicated in Tables 7.1 and 7.2, with three different values of this parameter (whose value, once translated into real dimensions, is about 5.3 cm, 10.6 cm and 15.9 cm). Among these 22 runs, 14 were performed using the smooth version of the impellers model, while for the remaining 8 the non-smooth version of the force was chosen.

The truncation level l_{max} of the spherical harmonic expansions was chosen as it was done in previous studies carried out making use of the `DYNAMO` code [87]; more precisely, the maximum number of l modes was chosen in order that energy spectra of the flows in Reuter's hydrodynamics studies drop off by at least three orders of magnitude between their maximum at l = 2 and their tails.

It is important at this point to clarify the meaning of the parameters Re_0 and Rm_0 used in the `DYNAMO` code. These two parameters appear in the system of the governing equations solved by the `DYNAMO` code as coefficients with the role of Reynolds numbers. The Reynolds numbers should depend, however, on the characteristic amplitude of the velocity field, according to the definition; in other words, they cannot be established *a priori*, before starting a simulation, without any knowledge of the resulting flow field. Hence, in order to realistically represent the usual dimensionless Reynolds number, we follow an established convention according to which the root mean square amplitude of the dimensionless velocity field, $U = \overline{\sqrt{\langle|\mathbf{u}|^2\rangle}}$, is multiplied with Re_0 and Rm_0 in order to obtain a more realistic estimation of the standard fluid and magnetic Reynolds numbers[1]. In Tables 7.3 and

[1]In the definition of U, the overbar represents a temporal average, while the brackets

Table 7.1: Run series A: Simulations with the first model of the baffle and the smooth version of the force.

Run	baffle width (cm)	Re_0	Rm_0	n_r	l_{max}
A1	5.3	100	90	320	30
A2	5.3	100	100	320	30
A3	5.3	200	90	320	30
A4	5.3	200	250	320	30
A5	5.3	300	80	320	30
A6	5.3	300	130	320	30
A7	5.3	300	175	320	30
A8	5.3	300	250	320	30
A9	5.3	600	250	360	52
A10	10.6	1000	200	512	52
A11	10.6	1000	350	512	52
A12	15.9	1000	200	512	52
A13	15.9	1000	230	512	52
A14	15.9	1000	240	512	52
A15	15.9	1000	350	512	70

Table 7.2: Run series B: Simulations with the first model of the baffle and the non-smooth version of the force.

Run	baffle width (cm)	Re_0	Rm_0	n_r	l_{max}
B1	5.3	100	90	320	30
B2	5.3	100	100	320	30
B3	5.3	200	90	320	30
B4	5.3	200	250	320	30
B5	5.3	300	80	320	30
B6	5.3	300	250	320	30
B7	5.3	500	250	320	30
B8	5.3	600	100	320	30

7.4, we list, for those runs, the values of the root mean square velocity U, the Reynolds numbers Re and Rm, the time range $\Delta\tau$ over which the calculation of the growth rate γ was carried out, the growth rate itself and its error $\Delta\gamma$. With regard to the growth rate error, an already established method was used: a least-squares method was used to fit a straight line to the logarithm of the magnetic energy. Within the program GNUPLOT, the least-squares algorithm minimizes the sum S of the squared differences (or residuals) of the input data points and the straight function values, i.e.,

$$S = \sum_{1}^{N} (y_i - g(t_i))^2,$$

where $y_i = \ln E_M(t_i)$ are the discrete data values of the logarithm of the magnetic energy at time t_i and the function $g(t)$ represents the fitted straight line. As a measure of the goodness-of-fit, GNUPLOT gives the value σ of the root mean square of the residuals. From geometrical considerations, a good estimation of the error of the growth rate is given by $2\sigma_g/\Delta\tau$. This expression was taken as the definition of $\Delta\gamma$ [87].

The results obtained via this kind of baffle model do not exhibit any gain in the growth rate or any significant drop of the threshold (in most cases the situation is even worst, especially for the non-smooth force) when we compare them to the simulations of previous works [87] or with new runs without the baffle. Among the cases where the growth rate is greater than the ones obtained with simulations without the baffle (see Table 7.1, growth rates in bold face), run A8 seems to be particularly interesting, since the growth rate error is relatively low and it is a turbulent case.

In Table 7.5, we report a tabular overview of the simulations without baffle. We use these results as a reference in order to compare the effects of the modification of these default runs. Previous numerical investigations [87] permit us comparison with simulations whose Reynolds numbers are not indicated in Table 7.5.

7.1.2 Implementation of the equatorial baffle in the spectral domain

Damping the $\mathbf{t}_1^1$ field

We implemented a second possibility of mimicking the effect of the baffle. In order to explain how this method works, let us start from the expression of the θ and ϕ components of the toroidal vector field $\mathbf{u}_{tor}$ in the Bullard-Gellman decomposition of the velocity field $\mathbf{u} = \mathbf{u}_{tor} + \mathbf{u}_{pol}$. As shown in the original paper [32], it reads:

a spatial average.

Table 7.3: Run series A: Simulations with the first version of the baffle and the smooth version of the force. The bold face growth rates are the only ones which are larger than the growth rates obtained from simulation without the baffle.

Run	U	Re	Rm	$\Delta\tau$	γ	$\Delta\gamma$
A1	0.38	38	34	1.25	**15.523**	0.008
A2	0.38	38	38	1.6	19.488	0.004
A3	0.41	82	37	0.7	-0.45	0.18
A4	0.41	82	102	1	74.6	1.1
A5	0.29	87	23	1.2	-10.55	0.03
A6	0.29	87	38	9.5	-0.184	0.008
A7	0.29	87	50	1.3	9.19	0.07
A8	0.46	138	115	0.3	**49**	3
A9	0.33	198	83	2.25	16.4	0.6
A10	0.4	400	80	0.6	-4.17	3
A11	0.57	570	200	0.14	-19	7
A12	0.56	560	110	0.32	0	3
A13	0.56	560	128	0.2	3	4
A14	0.56	560	135	0.42	$\mathbf{-0.5}$	1.4

Table 7.4: Run series B: Simulations with the first version of the baffle and the non-smooth version of the force.

Run	U	Re	Rm	$\Delta\tau$	γ	$\Delta\gamma$
B1	0.23	23	21	2.5	4.54582	0.00006
B2	0.23	23	23	1.05	8.00	0.06
B3	0.34	68	31	2.55	8.61638	0.00017
B4	0.34	68	85	0.83	61.11	0.08
B5	0.41	123	33	16	-10.39	0.07
B6	0.41	123	103	0.4	26.3	0.32
B7	0.51	255	128	1.2	19.0	0.7
B8	0.54	324	54	2.3	-4.55	0.4

Table 7.5: reference simulations without the use of the baffle.

Run	Re_0	Rm_0	n_r	l_{max}	$\Delta\tau$	γ	$\Delta\gamma$
def1	100	85	320	30	1.4	2.790	0.002
def1	100	90	320	30	0.7	15.50	0.014
def2	100	100	320	30	1.3	19.494	0.004
def4	200	60	320	30	2.4	-2.983	0.007
def5	200	67	320	30	2	-0.2866	0.00014
def6	200	68	320	30	2.8	0.10138	0.00013
def7	200	70	320	30	12	0.861	0.006
def8	200	90	320	30	1.35	8.613	0.004
def9	200	250	320	30	3.23	74.6	1.1
def10	300	80	320	30	6	5.6	0.6
def11	300	250	320	30	0.4	40.2	1.5
def12	600	100	360	52	1.6	-6.0	0.4
def13	600	250	360	52	1.6	24.42	1.1
def14	1000	200	512	70	0.8	-2.3	1.5
def15	1000	350	512	72	0.9	12	2
def16	2000	200	512	70	1.7	-13.8	0.9

$$\mathbf{u}_{tor} \cdot \hat{\mathbf{e}}_\theta = \sum_{l,m} \frac{t_l^m(r)}{r \sin\theta} \frac{\partial \mathcal{Y}_l^m(\theta,\phi)}{\partial \phi}, \tag{7.1}$$

$$\mathbf{u}_{tor} \cdot \hat{\mathbf{e}}_\phi = \sum_{l,m} \frac{t_l^m(r)}{r} \frac{\partial \mathcal{Y}_l^m(\theta,\phi)}{\partial \theta}. \tag{7.2}$$

As already explained, the goal of the introduction of the equatorial baffle is to suppress the shear layer fluctuations in the equatorial plane. This is translated into a damping of the θ component of the toroidal part of the velocity field. This task can be accomplished by a reduction of the toroidal spectral functions modes $t_l^m(r)$ near the boundaries (i.e., at $r \sim 1$), as can be easily seen from Equations (7.1) and (7.2), under the hypothesis that in this way a global reduction of the toroidal large scale eddies can be obtained. This kind of filtering is performed by the `DYNAMO` code every time step of the calculation in order to weaken the toroidal field in that region[2]. As a first attempt, we choose to damp the toroidal function t_1^1 (see [81]), one of the modes that are mainly responsible of the large scale shear layer. The damping was performed making use of an exponential prefactor in order to

[2]It is possible, in principle, to use the same strategy for the poloidal modes too, but in this case, since the equations analogous to Equations (7.1)-(7.2) involve the derivative of the poloidal functions respect to r and not simply the poloidal functions, the same procedure leads to a damping of the derivative, which we avoided in order to not create too steep gradients in the numerical runs.

Table 7.6: Run series C: simulations with the second version of the baffle model and the non-smooth version of the force.

Run	σ_{damp}	Re_0	Rm_0	n_r	l_{max}
C1	0.05	300	250	320	30
C2	0.1	300	250	320	30
C3	0.05	1000	350	512	70
C4	0.15	1000	350	512	70

influence the field near the boundaries in the following way:

$$t_1^1(r) \rightarrow t_1^1(r) \times \Big(1 - \exp\Big\{ - \frac{|1-r|}{\sigma_{damp}} \Big\}\Big).$$

In this formulation, we use the adjustable parameter σ_{damp} as a measure of the width of the baffle. In Table 7.6, the runs which were performed are listed.

It should be noted that, as a spurious effect of this numerical filter, the ϕ-component of the toroidal field is damped too, since expression (7.2) shows that the ϕ-component depends – as well as the θ-component of the field – on the functions t_l^m in a similar fashion. In Table 7.7, the results of series C runs are listed. This technique seems to be promising, since runs C1 and C3 show growth rates which are just slightly larger than the ones obtained by the default simulations. The reference case for run C1 gives $\gamma = 40$, while for run C3 we find a value of 12. As reference cases, we can use the results of previous studies (see [87]); in this former investigation, however, the simulations used lower resolutions than ours and we should be careful when we compare the results. With lower resolutions, in fact, the predictions of the growth rates can be quite optimistic, i.e., they lead to larger values. For instance, the reference case for run C3 has a growth rate of 15, as it can be easily calculated by interpolating the results of these previous simulations (in this case, $n_r = 320$ and $l_{max} = 38$, less than our $n_r = 512$ and $l_{max} = 72$). These results should not be overestimated: although an enhancement of the growth rate – taking into a account the uncertainties – can be detected, the impact on the threshold does not seem to be tremendous. Nevertheless, we should underline that, according to this analysis, an optimum value of the numerical baffle width exists, since runs C1 and C3 share the same value of the adjustable parameter σ_{damp} (whose amplitude is related to the spatial extension of the filtering effect of the numerical baffle). Using larger values, as the results suggest, seems to have even more detrimental effects on the dynamo instability. If this technique is enough realistic in order to mimic the effect of a real baffle, as future investigations can probably confirm, what we learnt from these results is that the dynamo threshold can be rather sensitive to the choice of the width of the installed baffle.

Table 7.7: Run series C: Results.

Run	U	Re	Rm	$\Delta\tau$	γ	$\Delta\gamma$
C1	0.48	144	120	0.41	**45**	3
C2	0.48	144	120	0.45	42.5	1.6
C3	0.57	570	200	0.8	**17.1**	1.8
C4	0.56	560	200	0.65	15	4

Damping the toroidal modes with a positive θ-component in the equatorial plane

An analogous test was made applying the same damping to all the $t_l^m(r)$ functions which can be responsible for the shear layer flow observed in the experiment. The toroidal modes we are talking about are those with both even l and even m or those with both odd l and odd m. In other words, we are only interested in modes which contribute to a non-zero value of the θ component of the velocity field on the equatorial plane. It can easily be shown, using the properties of the spherical harmonics $\mathcal{Y}_l^m$, that zeroing these modes makes expression (7.1) identically zero at $\theta = 90°$ (i.e., on the equatorial plane), irrespective of the functional form of the t_l^m modes. With this modified version of the spectral baffle, a simulation was performed using $\sigma_{damp} = 0.15$. The other parameters were: $Re_0 = 1000$, $Rm_0 = 350$, $n_r = 512$, $l_{max} = 70$. With this choice, it is possible to use run C4 as a reference case. The growth rate turns out to be smaller that that of run C4, having the value of 3 (± 3) over a time range of about 0.5 diffusivity time units.

Zeroing out the shear layer modes

Another way to introduce in the simulations the effect of the baffle is the zeroing out of a specific set of modes during every time step. The set of toroidal modes which were zeroed out is formed by the mode responsible of the shear layer (the same one damped in the previous version of the baffle, see description), while the set of poloidal modes is formed by modes whose l and m indexes are not both contemporarily even or odd. The zeroed poloidal modes were chosen following the same criterion described in the previous section, i.e., the set of modes to be zeroed out must contribute to the θ-component of the velocity field on the equatorial plane. According to the Bullard-Gellman decomposition, the expression – analogous to Eqs (7.1) – for the θ-component of the poloidal part of the velocity field is

$$\mathbf{u}_{pol} \cdot \hat{\mathbf{e}}_\theta = \sum_{l,m} \frac{1}{r} \frac{\mathrm{d}s_l^m(r)}{\mathrm{d}r} \frac{\partial \mathcal{Y}_l^m(\theta,\phi)}{\partial \theta}. \tag{7.3}$$

Simulations at $Re_0 = 1000$ with two different magnetic diffusivities ($Rm_0 = 350$ and $Rm_0 = 600$) were performed, with a radial resolution of $n_r = 512$ and $l_{max} = 70$ $l-$modes. For the case with $Rm_0 = 350$, the growth rate turns out to be -28±4 over 0.25 τ_σ, while in the case with $Rm_0 = 600$, the growth rate is -22±2. In both cases, the introduction of the baffle was particularly detrimental if we consider that the dynamo threshold is expected to be about $Rm_c = 111$, according to previous simulations [87].

Zeroing out single specific modes

Zeroing out specific modes (e.g. $s_1^0(r)$ and $t_1^1(r)$) can represent another possible way to induce in the system the effects of the baffle, without destroying too much the interaction among velocity and magnetic modes, as it happens when the previous version of the baffle is applied. As can be seen in [81], experiments show that one of the main effects of the equatorial baffle is a weakening of the amplitude and of the fluctuations of these two modes, which represent (to lowest order) the shear layer. In order to complete this analysis, other investigations on the impact on the growth rate were conducted zeroing other modes too, i.e., $s_1^1(r)$, $s_2^1(r)$, $t_2^1(r)$ (see table 7.8 for an overview of the simulations).

Table 7.8: series D: simulations with a by "hand" zeroing of various specific velocity modes.

Run	Zeroed modes	Re_0	Rm_0	n_r	l_{max}
D1	s_1^0	1000	200	512	52
D2	s_1^0	1000	350	512	52
D3	s_1^0	600	140	360	30
D4	s_1^1	600	250	320	30
D5	t_1^1	600	250	320	30
D6	t_2^1	600	250	320	30
D7	s_2^1	600	250	360	52
D8	$s_1^0,\ t_1^1$	600	250	320	30
D9	$s_1^0,\ t_1^1$	1000	200	512	52
D10	$s_1^0,\ t_1^1$	1000	230	512	52
D11	$s_1^0,\ t_1^1$	1000	250	512	52
D12	$s_1^0,\ t_1^1$	1000	350	512	52

As in the previous approach, this implementation is detrimental for the amplification of the magnetic field. In fact, looking at the results in Table 7.9 and comparing them to the default simulation, none of them seems to represent a step forward in the attempt to enhance the growth rate. The main conclusion is that, although these large scale modes are probably responsible for large departures from the Dudley-James mean flow, as the

Table 7.9: Run series D: results.

Run	U	Re	Rm	$\Delta\tau$	γ	$\Delta\gamma$
D1	0.57	570	114	0.23	2	3
D2	0.58	580	203	0.5	-4.7	1.5
D3	0.54	324	75	0.8	2	3
D4	0.53	318	132	2	17.6	0.9
D5	0.56	336	140	1.2	18.4	1.4
D6	0.53	318	132	5	4.9	1.1
D7	0.36	216	135	0.35	12	3
D8	0.54	324	90	1.5	19.7	1.1
D9	0.57	570	114	0.35	-9	3
D10	0.57	570	131	0.9	-1.4	1.3
D11	0.57	570	142	1.11	-2.8	0.8
D12	0.57	570	200	0.7	7.3	1.5

experiments seem to suggest, their complete absence (numerically speaking, the zeroing at every time step of the corresponding function s_l^m and t_l^m for every value of the radius) can anyway disturb too much the complex interaction[3] among the various velocity and magnetic modes.

7.2 Summary and interpretation of the results

The investigation described in this chapter was performed by modifying the default version of the `DYNAMO` code in such a way that the effect of the equatorial baffle of the MDE could be mimicked. The goal was to study the changes associated with the baffle that are detected experimentally, as described in [81]. The results of these new simulations were compared to the default ones. The latter were started afresh when it was needed (when the Reynolds numbers were not yet explored with the `DYNAMO` code). In some other cases, simulations performed for previous investigations [87] were used. The main observables used for such a comparison were the root mean square velocity U as a measure of the back-reaction of the magnetic field on the flow and the growth rate of the magnetic energy in order to quantify the 'efficiency' of the dynamo mechanism. Four different strategies were used. The first one was the modification in the spatial domain of the velocity flow in order to filter out the θ-component of the flow near the boundaries and on the equatorial plane. The remaining methods were focused on the modification of the velocity field in the spectral domain, filtering out the amplitude of the toroidal functions of the Bullard-Gellman decomposition

[3] A graphical representation of this interaction can be seen in [32] in the shape of a bubble diagram which shows the transfer of energy among the magnetic modes using specific velocity modes as catalysts.

near the boundaries or by zeroing specific modes that the experiment indicates as possible disturbance for the dynamo mechanism. The first goal of this modification of the code was the reduction of the turbulence level of these modes, while the final goal was the enhancement of the effective magnetic Reynolds number in order to exceed the dynamo threshold also for runs below the critical value Rm_c (since a reduction of the turbulent resistivity is expected thanks to the baffle).

The results of the simulations do not show a particular trend toward the lowering of the threshold. Except for a few runs, the introduction of these modifications seems to be even more detrimental for the dynamo mechanism. Despite these difficulties and limitations, interesting conclusions shall be anyway drawn. The first one is the realization that the best way of introducing the effects of the baffle without affecting too much the complex interaction between the velocity field and the magnetic field is to operate in the spectral domain. Thanks to the Bullard-Gellman decomposition, in fact, we are able to manipulate directly single flow modes and study the effects of our modifications using the net of three-wave interactions described by the bubble diagram (shown in [32]). This possibility turns out to be very important, because the experiment measure the energy in these specific modes, therefore a more direct comparison between experimental and simulated data can be done. Moreover, a spectral model of the baffle is the easiest way to suppress the fluctuation level of the energy contained in the eddy associated with t_1^1. By modifying the amplitude of the radial function $t_1^1(r)$ at the radial distance r we want, we are able to make changes to the shear layer flow in a very specific way. It is promising that, with this technique, not only the mean energy in the eddy associated to t_1^1 can be suppressed, but also of its fluctuation level. This result is highly desirable because, as the MFT shows, a decrease in the fluctuation level of t_1^1 leads to a correspondent decrease of the turbulent resistivity [81].

It turns out from this baffle model analysis that the interactions among the various modes that are responsible for the dynamo instability are very fragile. It is not a surprise that the geometry of the flow field can be of crucial importance for the onset of the dynamo instability (one of the main purposes of dynamo theory is, in fact, the identification of geometries which foster this phenomenon), but in this case even a very slight modification of the predictor-corrector steps of the Crank-Nicholson discretization method can result in a lowering of the growth rates and, consequently, in an enhancement of the threshold.

In order to lower the dynamo threshold, several strategies were explored so far. Among the ones which turned out to be numerically stable, the best one is represented by a filtering of the toroidal spectral functions $t_1^1(r)$ for value of r close to the maximum value 1. Concerning this technique, the spatial extent of the 'filtering region' can lead to very different results, as the simulations show. This is, of course, in agreement with the fact that

perturbing the geometry too much can enhance the instability threshold, but besides this qualitative result, we find a limiting value of the baffle width (0.05 times the radius of the sphere) which – at least according to the DYNAMO code – should not be exceeded. Apparently, a too significant modification of the flow creates an obstacle to the dynamo mechanism especially to the α effect. In fact, it can be shown that α depends on the correlation between poloidal e toroidal velocity modes which share the same l (see, e.g., equations in [81]). If the α effect is reduced, the generation mechanism of a large scale magnetic field through the interaction of small scale velocity and magnetic fluctuations is obstructed, as the enhancement of the threshold shows.

A promising result is the comparison of the experimental spectra of the components of the velocity and the magnetic fields with the simulated ones. It turns out that, especially for the magnetic field, the statistics of the time series is very similar. This analysis – which future investigations should keep exploring – shows that the real and the simulated systems are getting closer, thanks to the suppression of the fluctuations of the energy contained in the shear layer eddy t_1^1 and the introduction of the equatorial baffle in the experimental device. We interpret the suppression of the energy fluctuation by 25% of the previous value as a signal of decrease of the turbulent resistivity, as the MDE has experienced with the introduction of the equatorial baffle. From these analysis, we confirm that the equatorial baffle is not able to change drastically the dynamo mechanism – although it has a positive impact on the velocity field fluctuations – and that other modifications of the flow (or of the boundary conditions) should be taken into account in order to stimulate the magnetic field instability at lower Reynolds numbers.

Only a different strategy, as described at the end of chapter , will solve the issue that the equatorial baffle was not able to solve. The justification of this can be found in next chapter, where a completely different approach has been carried out after the unsuccessful results described in this chapter. This approach has been a thorough quantitative analysis of turbulence in the numerical MDE carried out in order to precisely identify vortexes with detrimental effects on dynamo action. The technique used to perform this task is the so-called Singular Value Decomposition (SVD). This statistical tool did not only allow us to explain why the equatorial baffle approach did not bring the positive results. It also gave us the possibility to gain further insight into the problem and therefore to design a new implementation of the baffle that turned out to foster dynamo action.

Chapter 8

Shedding light on the dynamo mechanism: The role of turbulence

8.1 Introduction

This Chapter represents the core of this dissertation: A detailed study of the role that turbulence plays in the MDE. This task has been accomplished by applying – for the first time in dynamo theory – a well-known technique to analyze the spatio-temporal statistical properties of the data produced by the `DYNAMO` code. The aim of this Chapter is hence to scrupulously describe the dynamics of the flow in order to understand which configurations are mostly detrimental for the dynamo process and which ones are favorable. The idea is the following: Decomposing the field via the Bullard-Gellman decomposition [32], we identify the modes which turn out to have an impact on the dynamo threshold Rm_c. In order to facilitate this analysis, we analyze the velocity field – simulated by the `DYNAMO` code [94, 98] – with a technique known as Singular Value Decomposition (SVD). This technique has been widely applied to the analysis of turbulent flows [150] and, more recently, to a variety of transport processes in plasma microturbulence, including impurity transport [151], electromagnetic transport [152], resistive ballooning plasma fluctuations [153], and saturation mechanisms [154]. A pedagogical introduction to this decomposition and its applications can be found in [155].

The Chapter is structured in the following way: in Section 8.2 we will describe the Singular Value Decomposition, with emphasis on the decomposition of the flow fields predicted by the `DYNAMO` code; in Section 8.3 we focus on the results of a "water" experiment (setting the magnetic conductivity to zero), showing the detailed structure and dynamics of the turbulent field found via SVD; in Section 8.4 we use the analysis of our results in order

to explain in more detail the dependence of the dynamo threshold Rm_c on turbulence (i.e., the curve $Rm_c(Re)$, previously found for this spherical system); Section 8.5 deals with possible ways to control large scale turbulence in order to facilitate dynamo action. Part of the results discussed in this Chapter have been recently published or submitted [120, 121].

Contents

8.1 Introduction 112
8.2 SVD analysis 113
8.2.1 Statistical aspects of SVD 115
8.2.2 Further important properties of the SVD analysis and application to the DYNAMO data 117
8.3 SVD analysis of the virtual water experiment . 121
8.3.1 First SVD mode 121
8.3.2 Second SVD mode 122
8.3.3 Singular values 125
8.3.4 Temporal evolution 126
8.3.5 Comparison with previous results 130
8.3.6 Role of time-stationary $u_2(\mathbf{r})$ in the dynamo process 131
8.4 An interpretation of the $Rm_c(Re)$ curve 132
8.5 Strategies for turbulence control for dynamo purposes 133
8.5.1 Role of an equatorial baffle 134
8.5.2 Role of a disc-shaped equatorial baffle between the impellers 135
8.5.3 Results 136
8.6 Interpretation of the results 136
8.7 Summary 137

8.2 SVD analysis

The *Singular Value Decomposition* (SVD) also known as *Proper Orthogonal Decomposition* or *Principal Component Analysis*, is a mathematical technique used in the framework of multivariate statistics in order to simplify the representation of datasets or in order to reduce the memory which is needed to store them. Pedagogical introductions to this analysis and its applications can be found in [150, 151, 155].

The principal aim of this method is the reduction of the number of variables used to quantify the properties of the data under analysis.

This reduction is obtained by substituting the original variables with a set of latent variables which are less numerous, via an orthogonal linear

transformation of the former variables. This process can be easily understood geometrically with the following picture. A dataset can be represented as a set of points immersed in a cartesian system (the parameter space). The geometrical distribution of these data points – generally speaking – could not have any correlation with the variables represented by the cartesian axes. On the contrary, the SVD analysis finds the *principal components* of the set of points, in other words, it finds new cartesian axes which have the highest correlation with the geometry of the distribution of the points: The data points are hence spread mainly over the new axes. Mathematically, this means that the distribution of the data has its maximum variances in correspondence with the new set of variables. The fact that the SVD analysis chooses variables with maximized variance comes from the result that the variance of a particular variable of a dataset quantifies how much the distribution of the points is spread over the axis of that variable. Moreover, this technique chooses a particular ordering of the new variables: they are ordered according to decreasing variance. This means that the first variables contain more information than the others and describe the large-scale features of the geometrical distribution; the other variables add less information to the description, focusing on the small-scale features[1].

With this new representation of the data, it is possible to reduce the complexity of the dataset by projecting the data on the first new variables and limiting oneself to analyzing only the information described by these first *principal components*. In other words, the technique suggests an optimal set of eigenmodes that capture the main features of the data. Differently from other linear transformations used in statistics, in this technique the dataset itself determines the transformation, i.e., the technique tailors itself to the data. The SVD analysis is a very general and powerful technique applied in different contexts: in cosmology and astronomy (for the huge catalogues of galaxies), in the problem of the compression of the data (e.g., images), even to analyze medicine data. Further readings about the applicability of this technique can be found in a dedicated chapter in reference [155] and references therein or in Ref. [156]. In this last reference, several applications of this decomposition can be found and a similar matrix formalism is employed. Guidelines about how to implement a SVD routine can be found in the classical textbook [157].

The reduction of the complexity of the dataset leads, obviously, to a loss of information, i.e., to the degradation of the quality of the information respect to the original dataset. Nevertheless, it also provides a very good control on the loss of information, which can be handled simply choosing a

[1]The expressions *large-scale* and *small-scale* are used here in a context which is different from the context of turbulence in fluids, treated in the previous chapters; nevertheless, if the SVD analysis is applied to fluid mechanics data, the large (small) scale features of the distribution of the data often coincide with the large (small) scale features of the turbulent fields.

larger number of the principal component variables.

The mathematical aspects of the SVD analysis reveal interesting and useful features, as described in Section 8.2.1 and 8.2.2. In the context of this project, this technique was not merely used in order to save computer memory. The reason is more fundamental: By means of this method it is easier to understand the behavior of the system by isolating the most important dynamics and decomposing the fields in a more general (and appropriate) way and finally in order to explore in details the dynamo mechanism, shedding light on the details of the transfer of the energy between the kinetic and the magnetic component of the system.

8.2.1 Statistical aspects of SVD

There are two mathematical approaches used in order to treat the problem of the proper orthogonal decomposition. In this Section, we will describe the approach which is more pedagogical, briefly described in the last Section. In Section 8.2.2, we will discuss the other approach which is used normally in practice, making use of the Singular Value Decomposition theorem of an $M \times N$ matrix (see Appendix B.4). The two procedures are mathematically equivalent, as we will explain in next Section.

Let us start considering a set of N measures, where the $i-$th measure can be represented as a M-dimensional column vector $\mathbf{X}_i$ (i.e., M parameters characterize each observation). The dataset can be viewed hence as a $M \times N$ matrix (the so called *matrix of observations*). The goal of principal component analysis is to find an *orthogonal* (*unitary*, if the data are complex) *transformation* of the M coordinates axes of the parameter space, in order to obtain new axes such that the data are spread mainly along the first axes and such that the coordinates of the observations in the new representation are uncorrelated statistically (or, at least, as much as possible). Mathematically, the M-dimensional column vector of the new coordinates, $\mathbf{X}'$, is written as

$$\mathbf{X}' = P\mathbf{X}, \tag{8.1}$$

where P is an $M \times M$ orthogonal matrix and $\mathbf{X}$ is an M-dimensional column vector of the old variables. Let us indicate as A'_{ij} the ij-th component of the matrix of the observation in the new system of coordinates. According to Eq. 8.1, $X'_{ij} = \sum_{k=1}^{M} P_{ik} X_{kj}$. The new sample mean of the new observation vectors $\mathbf{X}'_1, ..., \mathbf{X}'_N$ is an M-dimensional vector $\hat{\mathbf{X}}'$, whose i-th component reads

$$\hat{X}'_i = \sum_{j=1}^{N} \frac{X'_{ij}}{N} = \frac{1}{N} \sum_{k=1}^{M} \sum_{j=1}^{N} P_{ik} X_{kj} = \sum_{k=1}^{M} P_{ik} \hat{X}_k,$$

i.e., the mean vector transforms via the same matrix which performs the transformation.

The new covariance matrix $\mathbf{\Sigma}' = (\sigma'_{ij})$ reads

$$\sigma'_{ij} = \sum_{l=1}^{N} \frac{(X'_{il} - \hat{X}'_i)(X'_{jl} - \hat{X}'_j)}{N-1}.$$

Using expression 8.1 and the transformation property of the mean vector, it is easy to show that

$$\sigma'_{ij} = \sum_{l=1}^{M} \sum_{m=1}^{M} P_{il} P_{jm} \sigma_{lm},$$

i.e., $\mathbf{\Sigma}' = P\mathbf{\Sigma}P^T$.

Let us impose that the transformation matrix P has the property that the data have maximized variance along the first new coordinate y_1; thus, we want to maximize the quantity $\sigma'_{11} = P_{1m}P_{1n}\sigma_{mn}$(having used Einstein's convention), with the constrain that $P_{1m}P_{1m} = 1$ (from the orthogonality condition of the matrix P, i.e., $P_{mk}P_{nk} = \delta_{mn}$). The Lagrange multipliers technique (see Appendix B.3) prescribes that, in order to obtain the solution, one should find the extrema of the function

$$\mathcal{L}(P) = P_{1m}P_{1n}\sigma_{mn} - \lambda(P_{1m}P_{1n} - 1).$$

The extrema are found by imposing the conditions

$$\frac{\partial \mathcal{L}}{\partial P_{1k}} = 2(\sigma_{mk} - \lambda\delta_{mk})P_{1m} = 0. \tag{8.2}$$

Eqs. 8.2 represent a homogeneous system of M equations in the M unknowns P_{1m}. This system has a non-trivial solution if and only if

$$\det(\sigma_{ij} - \lambda\delta_{ij}) = 0, \tag{8.3}$$

in other words, by diagonalizing the covariance matrix $\mathbf{\Sigma}$. In order to understand the meaning of the eigenvalues of $\mathbf{\Sigma}$, let us calculate the variance of the data respect to the first new coordinate, i.e.,

$$\sigma'_{11} = P_{1\alpha}P_{1\beta}\sigma_{\alpha\beta}. \tag{8.4}$$

Equation 8.2 shows that $P_{1\alpha}\sigma_{\alpha\beta} = \lambda_\gamma P_{1\beta}$, where λ_γ is one of the solutions of the secular equation 8.3, then Eq. 8.4 becomes

$$\sigma'_{11} = \lambda_\gamma P_{1\beta}P_{\beta 1} = \lambda_\gamma,$$

i.e., the eigenvalues of the covariance matrix $\mathbf{\Sigma}$ are the variances of the dataset respect to the new coordinates. By ordinating the eigenvalues according to the descending values, i.e., $\lambda_1 > \lambda_2 > ... > \lambda_M$, one associates to the first new variable the largest variance, to the second one the second

largest value of the variance and so on, creating in this way a hierarchy of new coordinates. Moreover, the fact that the off-diagonal terms of the matrix $\mathbf{\Sigma}'$ are zero (because in the new system, the covariance matrix is diagonal) assures that the variables are statistically uncorrelated.

8.2.2 Further important properties of the SVD analysis and application to the DYNAMO data

Section 8.2.1 was introduced mainly in order to show the statistical properties of the SVD analysis and in order to explain to the reader the idea beyond this method. In this section, instead, we describe in details how we used this technique on our datasets and with which consequences. In Figure 8.1, a sample dataset of observations in represented as a set of points immersed in the parameter space. With a translation of the axes it is possible to use the sample mean point as the origin of the new coordinate axes (*mean-deviation form*, geometrically represented in Figure 8.2).

Figure 8.1: This plot represents a scatter plot of the N observations in the parameter space, view as a set of N points immersed in a M-dimensional cartesian coordinate system (in this schematic example, $M = 2$). Picture taken from reference [155].

The matrix of observations, in this new representation called B, has as ij-th element the value $B_{ij} = X_{ij} - \hat{X}_i$. The *sample covariance matrix* is an $m \times m$ matrix S defined by

$$S = \frac{1}{N-1} BB^T.$$

The procedure described in section 8.2.1, i.e., the diagonalization of the covariance matrix $1/(N-1)BB^T$, is mathematically equivalent to the so-called *singular value decomposition* (see Appendix B.4) of the $M \times N$ matrix $A = (N-1)^{-1/2} B^T$. The singular value decomposition is the main tool for performing the principal component analysis in practical applications. The squares of the singular values of A are the p eigenvalues of the covariance

matrix $S = AA^T$, and the right singular vectors of the matrix A are the principal components of the data. From a computational point of view, iterative calculation of the SVD of A is faster and more accurate than an eigenvalue decomposition of S (see [155]).

The DYNAMO data which are analyzed via SVD are the velocity or magnetic fields calculated by the simulations. In spatial representation, the information contained in a vector field $\mathbf{V}(\mathbf{r}_i, t_j)$, where $\mathbf{r}_i$ is one of the gridpoints of the considered simulation and t_j is the j-th time step, can be rearranged in a 2D matrix $A(i, j)$ where the row index spans the spatial grid and the three components of the field $\mathbf{V}$ while the column index j spans the temporal dimension. In spectral representation, the information contained in a vector field is represented with a couple of values (the poloidal and toroidal radial profiles) as a function of the radial distance from the center of the sphere and the modes l and m. Here, we will indicate as $\mathbf{r}_i$ this generalized spatial point (r, l, m) and t_j is again the j-th time step. The data can be rearranged in a 2D matrix $A(i, j)$ where the row index spans the generalized spatial grid and the two components of the field while the column index j spans the temporal dimension. This rearranging of the field (see a schematic representation of it in Figure 8.3) can be easily accomplished by "unfolding" the spatial domain into a 1D array with $i = 1, 2, ..., N_{tot}$, where N_{tot} is, in the spatial representation, equal to $3n_r n_\theta n_\phi$ (the prefactor 3 due to the three dimensionality of the original field) or to $2n_r n_{modes}$ (the prefactor 2 due to the presence of a toroidal and a poloidal components, n_{modes} is the maximum number of relevant modes of the simulation, i.e. $(l_{max} + 1)(l_{max} + 2)/2 - 1$, see [87]). Although we could analyze the fields

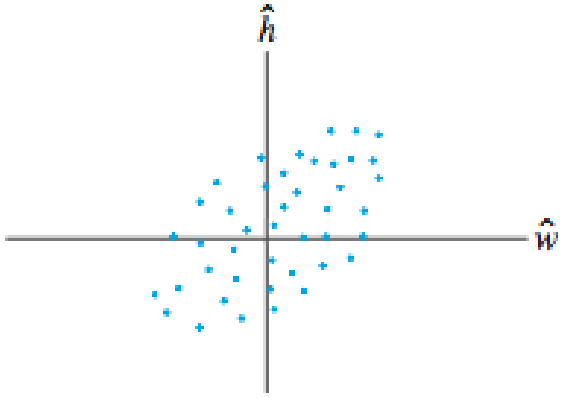

Figure 8.2: The same plot as in Figure 8.1, but with a translation of the origin of the axes to the sample mean point (the data are in the *mean-deviation form*). Picture taken from reference [155].

both in spatial and in spectral representation but we chose the second one, since this representation provides dataset which occupy less disk space and the SVD routines (provided by D. Hatch) are consequently faster.

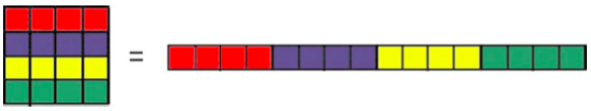

Figure 8.3: This picture shows schematically how the unravelling of a dataset into a 1D array works. In other words, the data are stored in a 1D array as they would be allocated in computer memory. Picture reprinted with permission from reference [151], Copyright 2009, AIP Publishing LLC.

Based on this idea, we represent the spatiotemporal DYNAMO data as the $A \in \mathbb{C}^{N_{tot} \times N_t}$ matrix, where N_t is the number of time steps considered, as also shown in [158] in a fusion plasma context. With this new arrangement of the data in a 2D matrix, it is possible to produce the singular value decomposition (which we accomplish using a parallelized SVD solver [159]), thus decomposing matrix A as

$$A_{ij} = \sum_{k=1}^{N_{SVD}} \sigma_k u_k(\mathbf{r}_i) v_k(t_j), \tag{8.5}$$

where we indicated with N_{SVD} the value $\min(N_{tot}, N_t)$. The N_{SVD} modes satisfy the orthonormality condition[2]

$$\sum_{i=1}^{N_{SVD}} u_m(\mathbf{r}_i) u_n(\mathbf{r}_i) = \sum_{j=1}^{N_{SVD}} v_m(t_j) u_n(t_j) = \delta_{mn}.$$

The singular values σ_k are ordered in descending order of magnitude: $\sigma_1 > \sigma_2 > ... > \sigma_{N_{SVD}}$. The value σ_k quantify the weight of the relative k-mode, i.e., the amount of information contained in the k-mode. Using the jargon of Fourier analysis, the spatial fields $u_k(\mathbf{t}_i)$ are the new generalized basis functions (compare the idea of the change of reference frame explained in Section 8.2.2) and the temporal functions $\sigma_k v_k(t_j)$ can be seen as the spectrum of the data as a function of the time. Both sets $u_k(\mathbf{r}_i)$ and $v_k(t_j)$ are defined as the sets of the SVD modes, or SVD eigenfunctions.

If the singular values σ_k decay fast as a function of k, as it typically happens, most of the information is contained in the first few modes, and the data can be compressed successfully, without a great loss of quality, by truncating the sum in Eq. 8.5 at $k = r$, with $r < N_{SVD}$. In the following,

[2]It should be noted that this orthonormality condition is lost when the data (in spectral representation) are transformed again in vector fields in spatial representation.

we will indicate with $A^{(r)}$ this truncation of the original dataset.

Another interesting statistical properties is the possibility of quantifying the information entropy of the decomposed datasets. In fact, the dimensionless value

$$p_k = \frac{\sigma_k^2}{\sum_{k=1}^{N_{SVD}} \sigma_k^2} \tag{8.6}$$

is comprised between 0 and 1. Moreover

$$\sum_{k=1}^{N_{SVD}} p_k = 1.$$

Thus, it behaves as a probability distribution function, to which it is possible to apply the formula of the normalized information entropy H, in order to quantify the degree of order of the data, i.e.,

$$H = -\frac{\sum_{k=1}^{N_{SVD}} p_k \log p_k}{\log N_{SVD}}. \tag{8.7}$$

When the data are in a very ordered configuration, i.e., only one mode is needed to represent the whole dataset ($A_{ij} = \sigma_1 u_1 v_1$), then $p_k = \delta_{10}$, hence $H = 0$. On the contrary, in the "highly disordered" configuration, when the information is uniformly distributed among all the SVD modes, the entropy value is maximum, i.e., $H = 1$.

At this point, the natural question which can arise is: What is the reason why we apply this decomposition of our DYNAMO dataset based on generalized orthonormal eigenfunctions when we already have at our disposal the standard spherical harmonics decomposition of the fields? The answer is that, from the point of view of the "information content" of the different possible expansions, the SVD analysis is optimal, as can be understood following the arguments explained in Section 8.2.2. In fact, by fitting the eigenfunctions to the data, this analysis has the properties that it minimizes the Euclidean distance $||A - A^{(r)}||$ between the original dataset A and its truncated version $A^{(r)}$, where

$$||A|| = \sqrt{\sum_{ij} A_{ij}^2} \tag{8.8}$$

is the Frobenius norm. In other words, the SVD analysis minimizes the truncation error of the compressed version of the data. This feature is mathematically equivalent to the maximization of the variance of the dataset along the first new generalized reference axes, as explained in Section 8.2.2 in a very general case.

In conclusion, the SVD analysis turns out to be a powerful tool which can capture more precisely the dynamics of our system, giving us the possi-

bility to understand the details of the dynamo process. In the next section, we will describe the results obtained by applying the SVD analysis on a hydrodynamic run.

8.3 SVD analysis of the virtual water experiment

In order to characterize quantitatively the hydrodynamics of the simulated system, as a first step we apply the SVD analysis to the data produced by a hydrodynamical simulation, i.e., setting to zero the conductivity of the medium, at numerical fluid Reynolds numbers $Re_0 = \{600, 1100, 3000\}$. Re_0 is a parameter read by the `DYNAMO` code before a simulation is started; in order to obtain the real fluid Reynolds number Re of a particular numerical simulation, Re_0 is multiplied with the characteristic velocity U of the simulation [87] because the characteristic velocity can only be determined *a posteriori* via the equations $U = \overline{v_{rms}}$ and $v_{rms} = \sqrt{\langle v^2 \rangle}$ (the angle brackets denote averaging in space and the overline denotes averaging in time which is performed during the quasi-stationary phase of the flow after the transient phase). The reason why Re_0 needs to be corrected lies in the fact that Re must depend upon the fluid velocity, as its definition states. In the simulations discussed in this chapter, $U \sim 0.5$. The number of radial grid points in the sphere is $n_r = 512$, whereas the spectral resolution is $l_{max} = \{52, 52, 180\}$ respectively. We then analyze the flow when it has reached a saturated state, considering $N_t = \{1550, 700, 400\}$ snapshots of the velocity field (i.e., the number of time slices which constitute the columns of the matrix A, see Section 8.2). The numbers N_t are chosen according to the available computer resources. With these input parameters, the resulting N_{SVD} turns out to be exactly $\{1550, 700, 400\}$ respectively. We will see that, among these N_{SVD} modes, only a few are necessary in order to reconstruct the field without a great loss of quality. In the following, we will separately analyze in detail the first two modes.

8.3.1 First SVD mode

We expect that the first SVD mode, i.e, $u_1(\mathbf{r})$ broadly captures the essential features of this hydrodynamical experiment. As mentioned above, it turns out that $u_1(\mathbf{r})$ is very similar to the mean field, which in turn resembles the Dudley & James input flow, as the Figures 8.4-8.6 show. These figures display a cross section of the sphere, i.e. the yz plane; whereas their color shows – respectively – the radial, the θ- and the ϕ-components of the first SVD mode. As the color scales suggest, the magnitude of the vector field is high in relation to the location of the impellers, and the typical counter-rotating nature of the motion can be seen thanks to the ϕ-component plot. In other words, the shape of the original *s2t2* flow can be recognized. A caveat is needed: In the original Dudley & James configuration, the flow

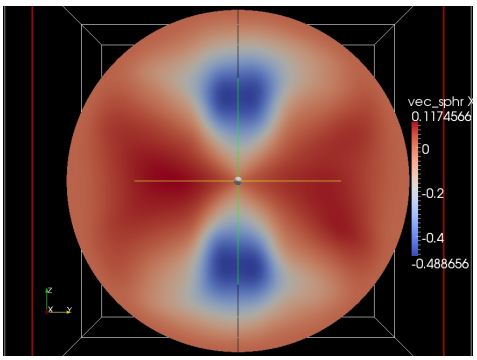

Figure 8.4: First SVD eigenfunction, $Re_0 = 600$: The color represents the magnitude of the r-component of the field. Picture reprinted with permission from [121], Copyright 2012, AIP Publishing LLC.

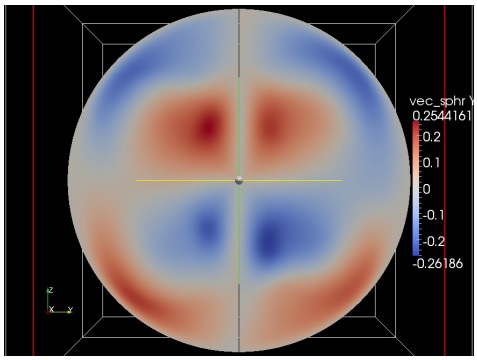

Figure 8.5: First SVD eigenfunction, $Re_0 = 600$: The color represents the magnitude of the θ-component of the field. Picture reprinted with permission from [121], Copyright 2012, AIP Publishing LLC.

is driven outwards to the poles by the impellers and then it streams along the walls to the equatorial plane; on the contrary, Figure 8.4 shows that the first mode behaves oppositely. However, once this mode is multiplied by $\sigma_1 v_1$ in order to reconstruct the field, the original behavior is recovered since $\sigma_1 v_1 < 0$ (as Figure 8.15 shows; note that $\mathfrak{Im}\{\sigma_1 v_1\} \sim 0$). We show the radial profiles of the spectral functions $s_{lm}(r)$ and $t_{lm}(r)$ at $Re_0 = 600$ in Figures 8.7-8.8. These Figures suggest that the most important modes are still those of the *s2t2* flow[3]. The situation is completely analogous at higher Re_0, just noisier, since the flow is more turbulent.

The singular value associated with this mode is $\sigma_1 = 96.9$ at $Re_0 = 600$, which means that the information content of this first mode is $\sigma_1^2 (\sum_{k=1}^{N_{SVD}} \sigma_k^2)^{-1} = 66.6\%$ of the total.

8.3.2 Second SVD mode

The second SVD eigenfunction is still relatively important. For instance, at $Re_0 = 600$ the associated singular value $\sigma_2 = 36.8$ is such that this mode contains alone 9.6% of the total information (see Section 8.3.3). Let us analyze the spectral and spatial behavior of this mode. Figures 8.9-8.10 show the radial profiles of the poloidal and toroidal stream function at $Re_0 = 600$ (as stated above, the situation at higher Re_0 is analogous). As these plots suggest, $u_2(\mathbf{r})$ consists of three main components: (a) a toroidal vortex t_{10}

[3]Poloidal stream functions have different physical dimensions from toroidal ones (see definition, Eq. 4.9), therefore direct comparisons of the scales of the plots in Figures 8.7-8.8 can take place only among stream function of the same kind (i.e., only among poloidal or only among toroidal ones)

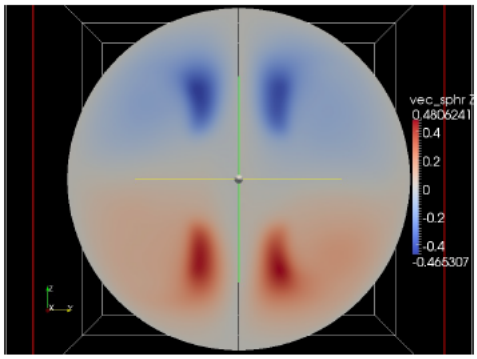

Figure 8.6: First SVD eigenfunction, $Re_0 = 600$: The color represents the magnitude of the ϕ-component of the field. Picture reprinted with permission from [121], Copyright 2012, AIP Publishing LLC.

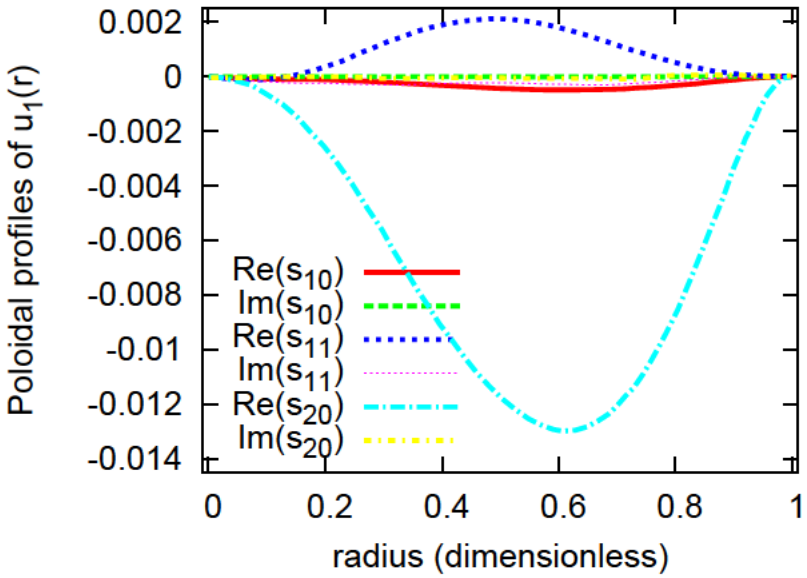

Figure 8.7: Radial profile of the poloidal modes of the first SVD eigenfunction, $Re_0 = 600$. Picture reprinted with permission from [121], Copyright 2012, AIP Publishing LLC.

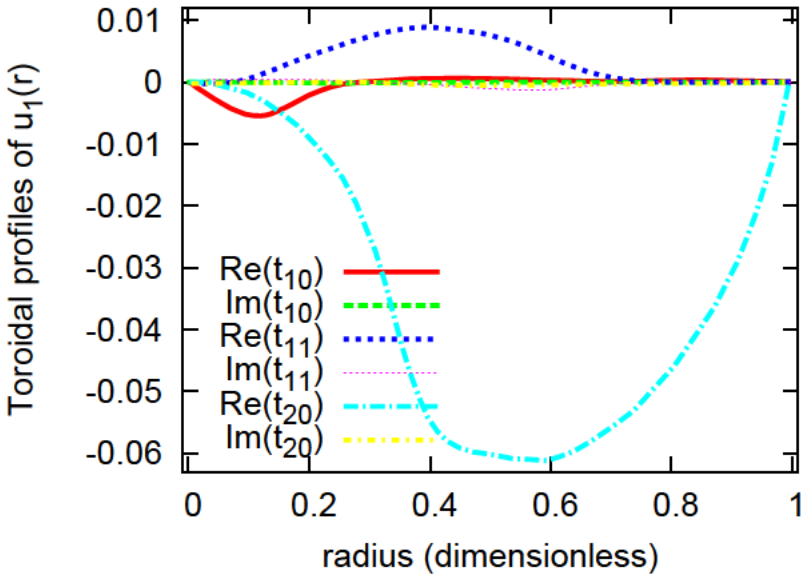

Figure 8.8: Radial profile of the toroidal modes of the first SVD eigenfunction, $Re_0 = 600$. Picture reprinted with permission from [121], Copyright 2012, AIP Publishing LLC.

with a strong activity at $r \sim 0.14$; (b) a poloidal circulation s_{10} which provides the velocity field with a vertical component (i.e., a z-component); this component has a relatively strong amplitude at about the same distance as the toroidal vortex, making $u_2(\mathbf{r})$ helical; (c) noisy toroidal and poloidal components with negligible amplitudes. In other words, the vortex has a smooth and large scale spatial dependence, with an elongated helical shape oriented along the axis of symmetry of the forcing mechanism. It does not show any counter-rotating feature, as the *s2t2* flow; on the contrary, its "winding" configuration is equal in the two hemispheres. Figure 8.11 shows a snapshot of the 3D fieldlines: The helical structure is readily recognized. Figures 8.12-8.13 confirm this description: In the first one the magnitude of the second SVD mode on the yz plane is represented, whereas in the second picture the ϕ-component of the field is shown, proving that $u_2(\mathbf{r})$ has no trace of the counter-rotating behavior of the impellers. An important remark: In some regions of Figure 8.13, the color changes discontinuously from $y < 0$ to $y > 0$: This is due to the fact that the y-component of the unit vector $\hat{e}_\phi$ changes sign form $y > 0$ to $y < 0$.

Note that this flow is characterized, at first glance, by a puzzling breaking of the symmetry expected from the force mechanism; the flow is driven by counter-rotating impellers, and yet $u_2(\mathbf{r})$ is characterized by a uniform rotation orientation on the axis between the impellers. The expected symmetry can only be retrieved – in an average sense – when one follows the

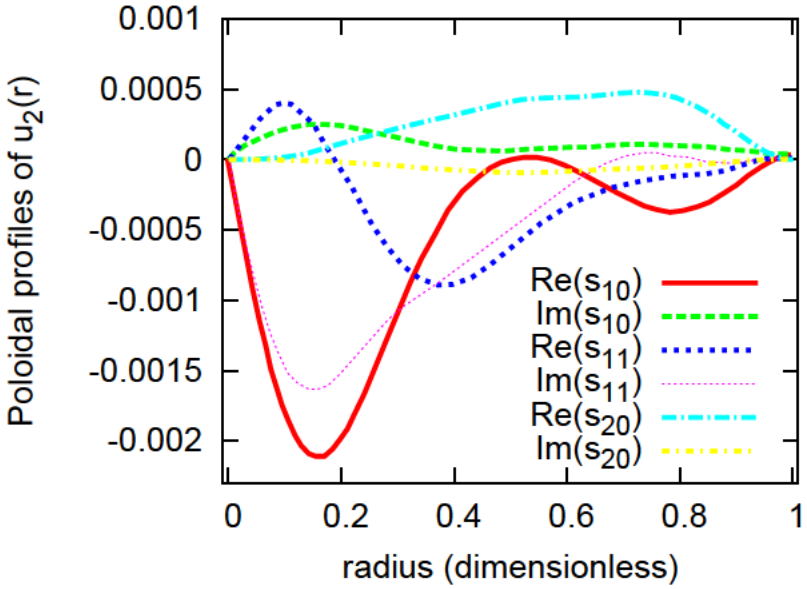

Figure 8.9: Radial profile of the poloidal modes of the second SVD eigenfunction, $Re_0 = 600$. Picture reprinted with permission from [121], Copyright 2012, AIP Publishing LLC.

temporal evolution of the mode, which exhibits alternating phases of opposite rotational orientation (see below).

8.3.3 Singular values

As already stated, every singular value σ_k quantifies the relative importance of the k-th mode. In Figure 8.14, the function $\sigma(k) = \sigma_k$ (with $Re_0 = 600$) is plotted in logarithmic scale. The plot shows that the decay of the singular values is exponential in the medium range of k-modes and it is even steeper at small values of k. This eventuality is particularly favorable, since it has as a consequence that the information of the dynamics is condensed in the first SVD modes, whereas further modes do not significantly improve the understanding of the overall dynamics. Although this result seems to suggest that adding more modes (i.e., using the SVD tools on more time steps) does not add further details to the decomposition, it should be noted that using a larger number of time steps can actually improve the statistics of the first modes too, giving to the SVD tools the possibility to encapsulate the information even better in the first modes. Table 8.1 reports the percentage of information content of the first 6 modes calculated via the definition of p_k, Eq. 8.6 (i.e., the relative amount of information contained in the k-th mode) with different Re_0. As the table shows, at higher Re_0, the flow becomes progressively more turbulent and, comparatively, more energy is

drained from the mean field and stored in the other extraneous modes.

Table 8.1: Information content of the first 6 k modes calculated via p_k.

	$k=1$	$k=2$	$k=3$	$k=4$	$k=5$	$k=6$
$Re_0 = 600$	66.6 %	9.6%	5.4%	2.9%	2.4%	1.8%
$Re_0 = 1100$	56.7 %	16.7%	5.1%	3.6%	2.6%	1.7%
$Re_0 = 3000$	54.9 %	15.2%	5.3%	4.1%	2.5%	1.9%

8.3.4 Temporal evolution

The SVD analysis provides a detailed description of the dynamics of the $u_k(\mathbf{r})$ modes: The temporal eigenfunctions $\sigma_1 v_1(t)$ and $\sigma_2 v_2(t)$ describe the (decoupled) dynamics of the associated spatial modes. For instance, we show the results with $Re_0 = 600$ (at higher Re_0 the outcome does not change). As can be seen in Figures 8.15 and 8.16, the imaginary parts of the two time series are negligible compared to the real parts. With regard to the first SVD mode, we note that the time series of the real part is an oscillation around a stable value (around -2.5, value which will be used in the next sections) which never crosses the $\sigma_1 v_1(t) = 0$ axis. This means that, as we expect from the behavior of the *s2t2* flow, the dynamics of the velocity

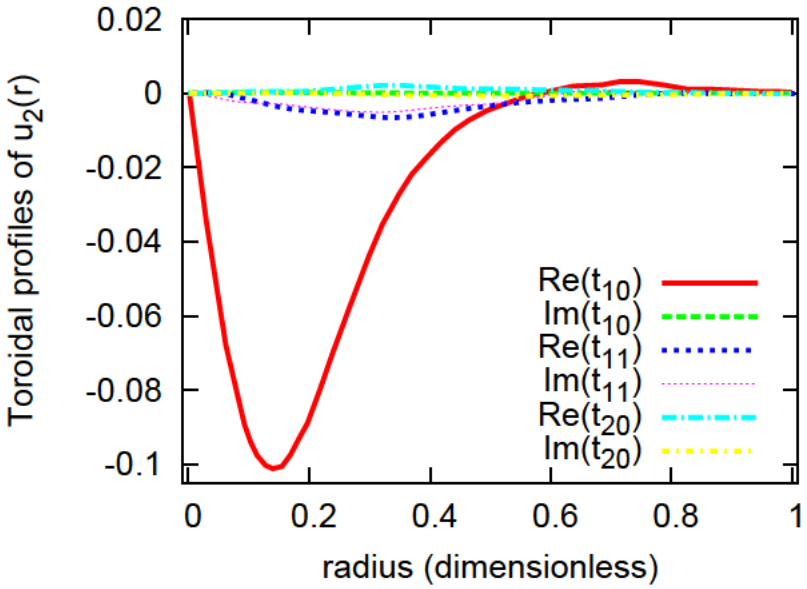

Figure 8.10: Radial profile of the toroidal modes of the second SVD eigenfunction, $Re_0 = 600$. Picture reprinted with permission from [121], Copyright 2012, AIP Publishing LLC.

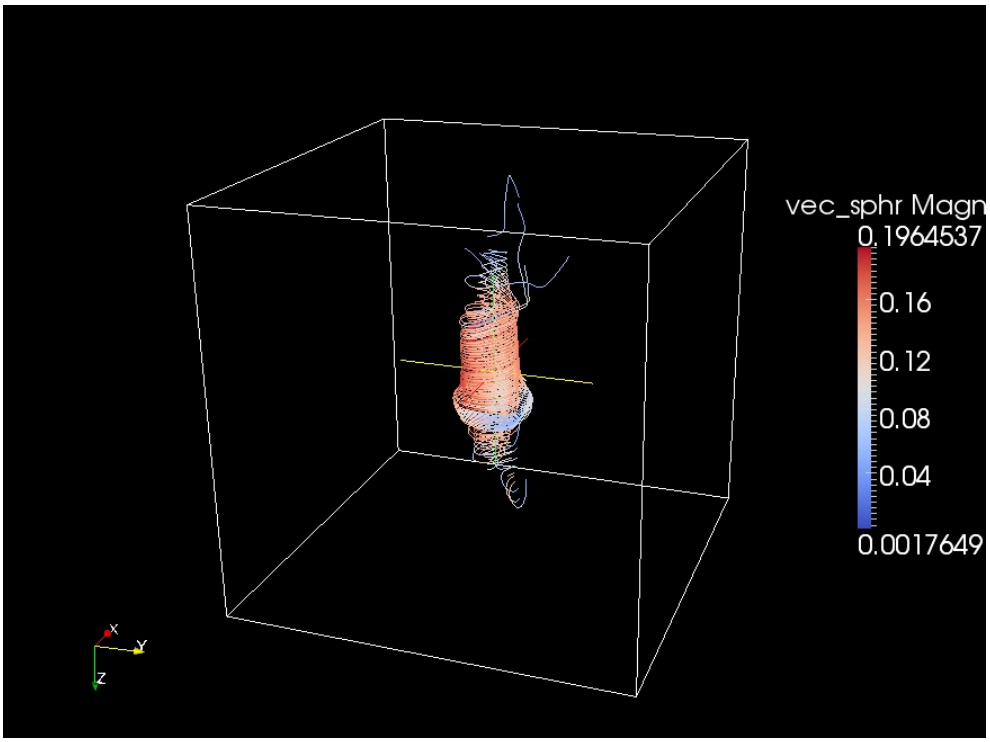

Figure 8.11: Field lines of the second SVD eigenfunction, $Re_0 = 600$. The helical structure described above can be recognized. The color represents the magnitude of the field. Picture reprinted with permission from [121], Copyright 2012, AIP Publishing LLC.

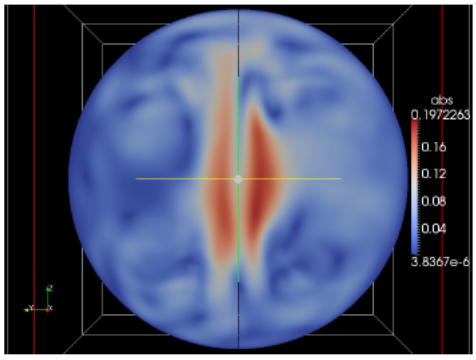

Figure 8.12: Cross section of the sphere, coordinate plane yz. The color represents the magnitude of the velocity field of the second SVD mode, $Re_0 = 600$. The vortex has its strongest activity along the axis of symmetry, at a distance of ~ 0.14. Reprinted figure with permission from [120].

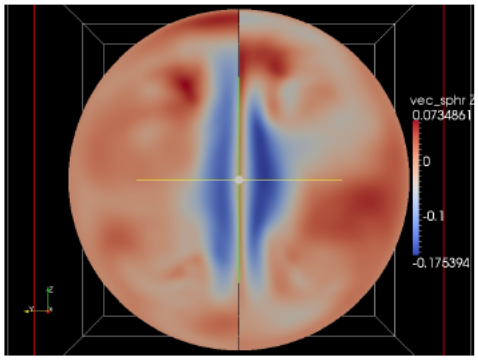

Figure 8.13: Cross section of the sphere, coordinate plane yz. The color represents the ϕ component of the velocity field of the second SVD mode, $Re_0 = 600$. For the discontinuity in the color from the half-space $y > 0$ to the half-space $y < 0$, see text. Reprinted figure with permission from [120].

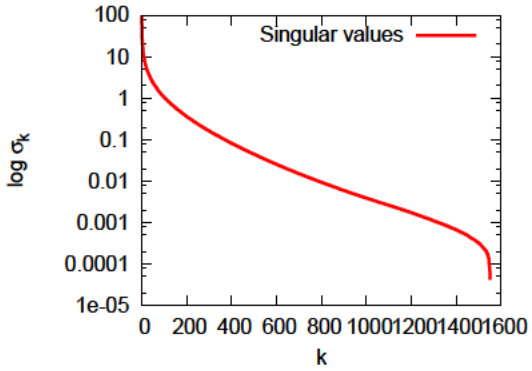

Figure 8.14: *Left*: Singular values σ_k as a function of k in a lin-log-plot, $Re_0 = 600$. For small values of k, the decay of the singular values is steeper than an exponential one. Reprinted figure with permission from [120].

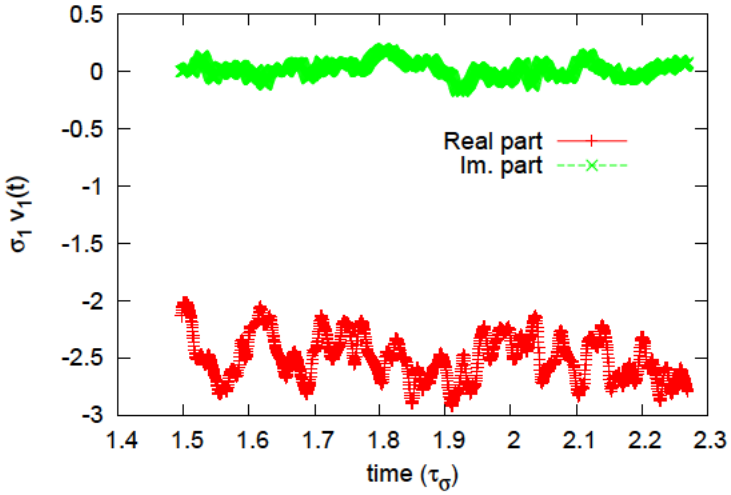

Figure 8.15: Real and imaginary parts of the SVD temporal eigenfunction $\sigma_1 v_1(t)$, $Re_0 = 600$. Reprinted figure with permission from [120].

field is basically an *s2t2* flow with a superimposed oscillating variation of the local magnitude of the vector field, conserving the rotational direction in each hemisphere. The behavior of the $\sigma_2 v_2(t)$ is different: The real part changes sign, being limited roughly between $+1.5$ and -1.5 (values used in the next sections). In other words, the helical vortex alternates phases with opposite rotational directions. This is translated, spatially, in a reversal of the vortex described in Section 8.3.2. These dynamics are difficult to extract without the use of SVD, which constructs basis functions specifically suited to the problem, and also clearly elucidates the temporal dynamics of each basis function.

Summarizing, the dynamics of this hydrodynamic simulation can be described by the following scenario. The usual counterrotating *s2t2* flow is produced by the forcing mechanism and it constitutes the main component of the flow, namely a stationary background flow. This *s2t2* flow is subjected instantaneously to increasing or decreasing activities around the mean configuration, as shown by the time trace in Figure 8.15. Superimposed to this background flow, a vortex-like component is spread over the axis of symmetry, with alternating activity between two opposed configurations, one with the same rotation direction of the *s2t2* flow in the northern hemisphere, the other one in the southern hemisphere. The additivity property of the decomposition states that the field associated with this secondary motion reinforces the magnitude of the velocity in the northern (southern) hemispheres and weakens the other one, when it is in the former (latter) configuration: In addition to the expected Dudley & James background flow, every hemisphere has a pulsating activity near the z axis, and this activity

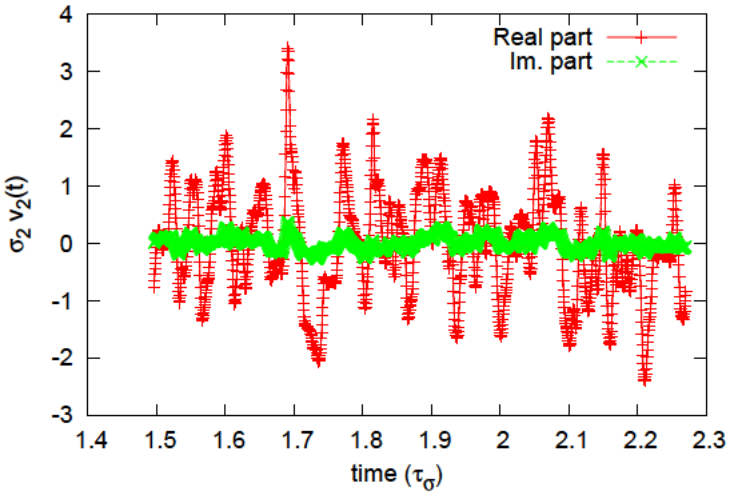

Figure 8.16: Real and imaginary parts of the SVD temporal eigenfunction $\sigma_2 v_2(t)$, $Re_0 = 600$. Reprinted figure with permission from [120].

is in counter-phase with respect to the activity in the other hemisphere.

8.3.5 Comparison with previous results

In this section, we draw a comparison of our results with those obtained experimentally for a turbulent von Kármán swirling flow, where two impellers counterrotate inside a cylindrical cavity [160, 161] and it was possible to reach fluid Reynolds numbers of the order of 10^4. In the experiment, a broken symmetry is observed – also in the exactly counterrotating case – with similar features to what we find: Reversals of the azimuthal velocity of the instantaneous flow are observed on the equatorial plane, and this fact can be interpreted as a phenomenon with characteristics along the same lines of the reversals of the vortex-like component represented by the second SVD mode. The laboratory flow can be divided into two toroidal cells around the two impellers, each one following the corresponding impeller, exactly as the mean flow of our model does. At the same time the fluid is driven towards the impellers and ejected to the cylindrical boundaries and the loop is closed with the return of the fluid along the walls and the equatorial plane. It turns out, however, that the flow presents two main configurations, each one breaking the symmetry around the equator (i.e., a rotation of π around every axis which lies on the equatorial plane). Moreover, the flow configuration alternates between these two states, with spontaneous jumps from one state to the other. Each of these configurations presents a "dominant cell" (alternatively, the north or the south cell) characterized by a higher velocity and a larger spatial extent. In other words, the locus of points where the

azimuthal velocity is zero does not lie on the equatorial plan, but encroaches on the northern (or in the mirror state, the south) half-space.

It is important to underline also the main difference between the experimental and our numerical results: In the experiment, the two configurations are relatively stable, i.e., the system can remain for relatively long periods in one of the two states before it undergoes a reversal. According to our simulations, the alternation between the two states takes place not suddenly as the experiment, but it is better described as an oscillation (compare, e.g., Figure 8.16 with Figure 3a in [160]). This difference probably emerges because of the smaller values of Re in the simulations and because of the presence of an equatorial baffle in the implementation of the `DYNAMO` code (see 8.5.1). In fact, other experiments with the same cylindrical geometry, but with the presence of an inner equatorial ring with a strong impact on the turbulence (e.g., as described in [162]), do *not* observe a broken symmetry of this type [160].

Nevertheless, if we compare the description of the dynamics given in Section 8.3.4 to the experimental picture, we can easily notice that the similarities are strong, although the fluid Reynolds number of our simulation is much smaller.

8.3.6 Role of time-stationary $u_2(\mathbf{r})$ in the dynamo process

In order to identify the impact of $u_2(\mathbf{r})$ on the dynamo mechanism, we performed three kinds of time-stationary kinematic (i.e., the flow does not evolve and is decoupled from the magnetic field) simulations at $Re_0 = 600$ and different Rm. The first one uses as fluid flow only $u_1(\mathbf{r})$ (the dominant mode), weighted with the mean value $\langle \sigma_1 v_1(t) \rangle$ (see Fig. 8.15). The second (third) run uses the superposition of $u_1(\mathbf{r})$ with $u_2(\mathbf{r})$, having weighted $u_2(\mathbf{r})$ with the maximum positive (minimum negative) value of the oscillating time trace $\sigma_2 v_2(t)$. The impact on the dynamo process can be summarized by comparing the growth rates of the magnetic energy and the critical magnetic Reynolds numbers (see Table 8.2 and Fig. 8.17, where the are runs indicated symbolically as "1", "1+2", "1-2", respectively).

As Fig. 8.17 shows, part of the detrimental effect on the dynamo threshold at $Re_0 = 600$ can be ascribed to the presence of a time-stationary $u_2(\mathbf{r})$. At $Re_0 = 1100$, $u_1(\mathbf{r})$ is noisier and less axisymmetric since the temporal sampling is shorter (the resolution is higher and the dataset should be reduced in order to apply the SVD with the same CPU resources): adding and subtracting $u_1(\mathbf{r})$ and $u_2(\mathbf{r})$ produces different values of γ because the noisy toroidal component of $u_1(\mathbf{r})$ tends to cancel out $u_2(\mathbf{r})$ in the "1-2" configuration. On the other hand, in the "1+2" configuration, $u_2(\mathbf{r})$ turns out to be detrimental. This last analysis does not take into consideration the role of the fluctuations in $u_2(\mathbf{r})$, which can also play a detrimental role, as suggested by the three-wave turbulent interaction picture in [81, 163].

Table 8.2: Growth rates of the magnetic energy for the runs "1" and "1+2", $Re_0 = 1100$.

	"1"	"1+2"
Rm_0=100	5.64 ± 0.013	-3.8 ± 0.4
Rm_0=150	27.4 ± 0.4	5.1 ± 0.5

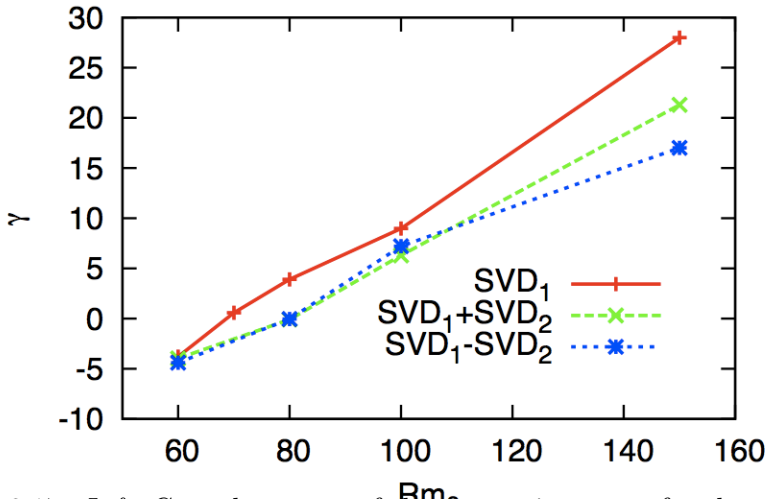

Figure 8.17: *Left*: Growth rates γ of the magnetic energy for the runs "1", "1+2", and "1-2", $Re_0 = 600$. A time-stationary $u_2(\mathbf{r})$ *has a detrimental effect* on the kinematic dynamo threshold. γ is scaled to the magnetic diffusion time, $\tau_\sigma = \mu_0 \sigma L^2$. Reprinted figure with permission from [120].

8.4 An interpretation of the $Rm_c(Re)$ curve

One of the main results of [94] is the study of the stability curve $Rm_c(Re)$ (Fig. 6 in the paper). The curve represents the dependency of the critical magnetic Reynolds number of the dynamo instability on the fluid Reynolds number, i.e., the impact of turbulence on the onset of the dynamo. According to [94], after a plateau in the laminar regime (at very small Re), the curve exhibits a quasi-linear behavior as Re increases, demonstrating that the dynamo threshold becomes more difficult to reach when the system approaches the turbulent regime. Then, the stability curve shows a steep increase after this linear phase. Remarkably, Rm_c reaches an absolute maximum, i.e., there is a value of Re that makes the dynamo particularly difficult to obtain. Starting from $Re \simeq 1800$, the critical magnetic Reynolds number decreases and a saturation of the curve occurs at higher Re. In other words, regardless of the increase of turbulence in the fluid in this regime, the dynamo threshold remains constant and is not affected by a further increase of Re. This results can play an important role during the design phase of an

experiment, especially if the curve stays constant at values of Re that are higher than the ones explored by the simulations described in [94]. An interpretation of this flattening is given in [94] using scaling arguments within the framework of the Kolmogorov-Richardson phenomenology.

Let us formulate another possible interpretation that can be given in the light of the results of SVD analysis. As summarized in Table 8.1, when Re is increased, the relative energy content of the vortexes with a negative effect is enhanced by turbulence, whereas the energy in the mean flow would still depend only on the large scale forcing mechanism (and not on Re). In fact, the presence of $u_2(\mathbf{r})$ at $\mathrm{Re}_0 = 600$ enhances Rm_c by 20%, whereas at $\mathrm{Re}_0 = 1100$ by 37%. The picture suggests that turbulence, increasing the energy of u_2 and not of $u_1(\mathbf{r})$ – which is prescribed by the force – makes the dynamo instability more difficult to reach, because the energy is redirected into velocity modes with a negative impact on the magnetic field growth rate. This effect can hence explain the quasi-linear behavior that the $Rm_c(Re)$ curve shows at low Re, where an increase of Re is converted into an increase of the critical magnetic Reynolds number. This same argumentation naturally leads to an explanation of the saturation of the $Rm_c(Re)$ curve at high Re as well: As Re_0 increases, the detrimental modes that the SVD finds are not allowed to grow indefinitely without a specific force mechanism that drives them (i.e., a mechanism that is not present in the system under study, because the impellers drive an $s2t2$ flow), hence their negative impact on the dynamo is limited although the system becomes more turbulent.

8.5 Strategies for turbulence control for dynamo purposes

In this section, we describe strategies designed in order to control large scale turbulence. The aim is to suggest practical actions to take in the experiments which can have a positive effect on the growth rates of the magnetic energy during dynamo action. We focus our attention on two different strategies. The first one (Section 8.5.1) is the control of shear layer turbulence, i.e., large scale eddies close to the boundaries with a detrimental effect on the dynamo. For this purpose, we model what was already installed in some experiments: a ring-shaped equatorial baffle, attached to the boundaries on the equatorial plane. As a second method (Section 8.5.2), we implement the application of another baffle on the equatorial plane, disc-shaped, which was not used in the experiments and whose positive effects can be interpreted according to the results obtained via SVD. Section 8.5.1 draws on information described in more detail in Chapter 7, and it is summarized here for matter of simplicity.

8.5.1 Role of an equatorial baffle

Hydrodynamic experiments [58, 149] have shown that attaching an equatorial axisymmetric baffle to the inner surface of a cylindrical vessel (in the mid-plane of the cylinder) represents a suitable technique to control the fluctuation amplitudes of large scale flows. This strategy was used also for a dynamo experiment in cylindrical geometry [78]. According to this study, such a baffle also has an effect on the mean flow, making the shear layer sharper around the mid-plane and, at the same time, reducing the turbulence intensity especially at low frequencies, although the flow remains strongly turbulent. The addition of such a baffle to a dynamo experiment was motivated by the results of previous numerical or experimental investigations that explored the influence of turbulence (especially at large scales) on the dynamo threshold and of the transverse motion of the shear layer across the mid-plane; e.g., the addition of large scale noise to the Taylor-Green mean flow increases the dynamo threshold, as shown numerically in [118]; also, fluctuating motion of eddies of the Roberts flow increase the threshold [164]. In [165], it is reported that the magnetic induction (due to an externally applied field) on a gallium flow depends significantly on the large scale flow fluctuations. All the results described so far suggest that the large scale motion and its fluctuations are of crucial importance for the creation of a dynamo in the MDE, although there is no concrete theoretical prediction about this issue. Although the experiments mentioned above have a slightly different geometry from the MDE, fluctuating large scale eddies in the MDE can create a great difference between the instantaneous flow and the mean flow [86], creating a detrimental effect for the magnetic field growth, although the mean flow – if stationary – is optimal (according to [80]). In the MDE, with the application of an external axial magnetic field, it is possible to observe an intermittent behavior of the magnetic field (whose fastest-growing eigenmode can alternate growing and decaying phases, see [86]). This result is seen as an effect of the departure of the instantaneous field from the mean field. In [81], it has been shown that such a baffle can successfully reduce global turbulent resistivity in the MDE.

Implementation of the equatorial baffle

The baffle effect consists of a modification of the computed velocity field by suppressing the vertical component of the flow. This suppression is applied at every time step in the spatial domain and then transferred to the spectral domain by a spatial-to-spectral transform. The flow modification takes place close to the boundaries, acting as a filter on the predicted velocity field. More precisely, the z component of the field was damped according to the following operation

$$\mathbf{u}(r,\theta,\phi) \rightarrow \mathbf{u}(r,\theta,\phi) - v_z f(r,\theta)\hat{\mathbf{z}}, \tag{8.9}$$

where the function f carries the spatial information of the damping mechanism. In order to avoid abrupt damping effects and steep gradients in the simulations, the function f employs Gaussian functions to describe the transition between the region where the damping effect is present and the region where it is not. In fact, it turned out that this Gaussian approach is well suited to avoid numerical instabilities and Gibbs phenomena. The functional form of f was chosen as

$$f(r,\theta) = \begin{cases} \exp\{(r\sin\theta - \rho_{ring})^2)/(2\sigma_r^2)\} & r\sin\theta < \rho_{ring} \\ 1 & r\sin\theta > \rho_{ring} \end{cases} \tag{8.10}$$

The interpretation of the adjustable parameters σ_z, σ_r, and ρ_{ring} is as follows. The first parameter, σ_z, is a measure of the thickness of the baffle; σ_r represents a damping parameter along the radial direction; ρ_{ring} is the inner axial radius of the ring. The results are discussed in section 8.6.

8.5.2 Role of a disc-shaped equatorial baffle between the impellers

Another strategy – used to suppress or manipulate detrimental dynamics – naturally comes from the results of the SVD analysis: We implemented in the code the effect of a discoidal baffle centered on the equatorial plane (i.e., lying between the impellers), in order to separate the dynamics in the two hemispheres, avoiding a strong poloidal circulation near the axis and facilitating the separation of the dynamics of the toroidal circulation in the two hemispheres. In the light of the SVD results, the underlying idea is that the disc can influence $u_2(\mathbf{r})$ and hence facilitate the dynamo.

Implementation of the disc-shaped baffle.

The action of this disc consists of a modification of the computed velocity similar to the one used for the ring-shaped baffle. The field is modified in a flat circular region lying on the equatorial plane where a spatially smooth suppression of the vertical component of the flow is performed at every time step. This suppression acts as a filter on the predicted velocity field. The z component of the field is damped according to Equation 8.9, using another f function in order to apply the damping mechanism in the center of the equator. Again, the function f employs Gaussian functions to describe the spatial behavior of the disc in order to avoid numerical instabilities (for this reason, the disc is approximated by a flat ellipsoid). Thus, the functional form of f for the disc is

$$f(r,\theta) = \exp\Big[-\frac{r^2\cos^2\theta}{2\sigma_z^2} - \frac{r^2\sin^2\theta}{2\rho_d^2}\Big]. \tag{8.11}$$

The interpretation of the adjustable parameters σ_z, and ρ_d is straightforward: σ_z is a measure of the thickness of the disc; ρ_d represents the disc radius, whose value was chosen in order to cover spatially at least the region of the equatorial plane through which $u_2(\mathbf{r})$ flows, as Figures 8.9 and 8.10 suggest.

8.5.3 Results

Kinematic simulations (i.e., neglecting the Lorentz force term in the Navier-Stokes equations) show that the growth rate γ of the magnetic energy is enhanced by both the baffle and the disc. Nevertheless, the baffle effect is not as strong as the disc effect. Table 8.3 shows the effect of the disc on the default growth rate γ. We indicate with γ_r the growth rate of the magnetic energy in presence of the baffle, γ_d in presence of the disc. It should be noted that a larger ρ_d is needed to have a non negligible effect at $Re_0 = 1000$, confirming the necessity of a stricter control of large scale turbulence at higher Re_0. The results are discussed in section 8.6.

Table 8.3: MHD simulations of dynamos with an implemented equatorial disc in the center of the equatorial plane. γ_d is the growth rate (the time is scaled to the resistive diffusion time, $\tau_\sigma = \mu_0\sigma L^2$) of the magnetic energy in the presence of the disk; γ_r in the presence of the ring; γ_0 is the default growth rate, i.e., without any baffle.

Re_0	Rm_0	l_{max}	ρ_d	γ_r	γ_d	γ_0
300	80	30	0.28	7.62	18.8	4
300	100	30	0.28	15.5	30.8	9.8
300	150	30	0.28	31.2	58.6	24
300	250	30	0.28	52	109	39
600	250	52	0.28	28.4	45.4	22.6
600	250	72	0.28	29.9	50.4	22.6
1000	300	52	0.65	10.4	18.4	10.4

8.6 Interpretation of the results

In [80], Dudley and James studied the kinematic dynamo threshold of several flows. It turned out that simple flows (like the *s2t2*, the *s2t1* or *s1t1*) can trigger a dynamo field under specific circumstances. In particular, the flow

s1t1 investigated in [80] is

$$\mathbf{u} = \mathbf{t}_1^0 + \epsilon \mathbf{s}_1^0, \tag{8.12}$$

with Bullard-Gellman stream functions

$$s_1^0(r) = t_1^0(r) = r \sin(r\pi), \tag{8.13}$$

and $r \in [0, 1]$. These modes are similar to the corresponding ones of the second SVD mode, although they are not peaked near the axis as in our case. If $\epsilon = 0.17$ and $Rm > 155$, this flow turns out to sustain a kinematic dynamo.

The fact that the growth rate of the magnetic energy is negative for a whole range of low Rm, where *s2t2* is already a dynamo, can explain the reason why the combinations $\mathbf{u}_1 \pm \mathbf{u}_2$ have lower growth rates than the single $\mathbf{u}_1$. In fact, following the discussion in [166] (where the influence of time dependent flows on the kinematic dynamo threshold in ván Kárman flows was numerically investigated), the magnetic field responds to the instantaneous velocity field, oscillating between instantaneous solutions of the induction equation, and the resulting averaged growth rate is smaller than that produced by the optimal configuration (in our case the *s2t2* flow). A possible three-wave interaction between the velocity modes and magnetic modes plays a crucial role determining into which magnetic modes the kinetic energy flows: One role of the $u_2(\mathbf{r})$ mode should be in fact to extract energy from the magnetic field dipolar dynamo mode and put it into other magnetic modes that do not grow (they do not grow), namely reducing the magnetic energy growth rate of the system. This idea will be tested by future investigations.

The two strategies described in section 8.5 turn out to have a positive effect on the dynamo growth rate. In particular, by comparing the growth rate γ_r in the presence of the ring, the growth rate γ_d in the presence of the disc, and the growth rate γ_0 without any baffle, it turns out that the disc has the strongest impact on γ. This result is totally on the line to the SVD results: most of the turbulent detrimental action takes place along the axis and not only near the boundaries. This last analysis suggests how to put into practice these results: controlling the symmetry of the counter-rotating flow in the equatorial region, avoiding a strong poloidal circulation near the axis and facilitating the separation of the dynamics of the toroidal circulation in the two hemispheres may be the right strategy for facilitating the dynamo instability.

8.7 Summary

In this work, we presented computational results with direct application to the generation of magnetic fields in liquid metal experiments. The key

result was the identification – via application of a powerful mathematical technique to hydrodynamic simulations in spherical geometry – of turbulent dynamics which could constitute an obstacle for the generation of magnetic fields. These results can help to gain new insights into the hydrodynamics of the flows that are important for experimental purposes. In fact, dynamos are often not observed in laboratory at Reynolds numbers where they are theoretically expected and understanding the reasons why this discrepancy is found is fundamental in order to implement new experimental measures designed to overcome this problem. Concerning the physical reason of these difficulties, it has been suggested that turbulence (and in particular large scale fluctuations of the flow) constitutes an obstacle to dynamos. Yet it has been unclear to what extent these large scale fluctuations can have such a detrimental effect and in what way they can work against the generation of magnetic fields.

A detailed analysis of the fluid dynamics is the key issue and the Singular Value Decomposition constitutes a precise tool for determining the eigenmodes that better suit the problem. Furthermore, it identifies the temporal behavior of each of them and quantitatively determines the hierarchy of these modes. In this way, we identified specific features of the turbulent flow that – in combination with the background flow – suppress magnetic field generation. In other words, we proposed an easily classifiable dynamo detrimental mechanism and provided an additional support for large scale turbulence suppressing the dynamos rather than small scale.

In the last part, we showed the effect of two main strategies designed to control large scale fluctuations in our numerical model: The implementation of a ring-shaped and a disc-shaped baffles. The ring has already been used in experimentally, showing itself to be able to reduce turbulent resistivity in laboratory and – moreover – to slightly increase the growth rates in the simulations. In particular, the disc increases the growth rates of the magnetic energy, and this result can be also useful for experiments with similar topologies, since it constitutes a concrete step to take in order to overcome possible suppression mechanisms generated by fluctuations that break the so called π-symmetry of the system (i.e., a rotation of π around every axis which lies on the equatorial plane).

Future works could be focused on the details of the effects on the magnetic field of the secondary dynamics identified in this study. A three-wave interaction (between velocity modes and growing/damped magnetic modes) is playing an important role and the SVD could constitute the right technique in order to determine it, e.g., by applying the SVD to the magnetic field and investigating correlations with the most important $u_i(\mathbf{r})$'s. In fact, we expect that one role of $u_2(\mathbf{r})$ should be to extract energy from the magnetic field dipolar dynamo mode and put it into other damped magnetic modes.

Chapter 9

Conclusions

"The larger the magnetic field,
the stronger our ignorance."

Virginia Trimble (30 years
after Nordwijk)

In the course of this PhD project, two liquid-metal experiments have been studied via numerical simulations. Both experiments are relevant for astrophysics, since they study the possibility of recreating at laboratory scales two important instabilities that pop up from magnetohydrodynamics and that permeate the Universe: The dynamo instability and the magnetorotational instability. In order to support the experimental investigation, simulations can play a crucial role, by unveiling parameter regimes, details, or spatiotemporal data that are unaccessible to the experimentalists. Moreover, both experiments have not reached the unstable regime (or, in the case of the MRI experiment, it is hard to prove that the instability is actually occurring): Therefore, simulations can foresee which measurements have to be taken in order to facilitate (or amplify) the instabilities. In the following, an overview of the main results of this work is given.

9.1 Interplay between turbulence and the dynamo effect in the MDE

Concerning dynamo theory, we presented computational results with direct application to the generation of magnetic fields in liquid metal experiments. In particular, we focused our attention to the Madison Dynamo Experiment, which was built to demonstrate self-excited dynamo action in an impeller-driven flow of liquid sodium. The forcing mechanism is designed to impose the so-called *s2t2* flow to the working liquid, since previous studies have shown that this flow facilitates dynamo action. The apparatus reaches a

magnetic Reynolds number of $Rm \sim 100$, which implies a fluid Reynolds number of $Re \sim 10^7$, since the magnetic Prandtl number $Pm = Rm/Re$ of liquid sodium is of the order $\sim 10^{-5}$. Due to this high fluid Reynolds number, turbulence is easily excited, and the instantaneous flow can be different from the average flow that is supposed to cause dynamo action. These detrimental effects of turbulent fluctuations are probably the main reason why the current experimental setup does not show dynamo action. Those fluctuations, whose spatial and temporal scale have not been explored before but whose presence has been assumed by the experimentalists, enhance the critical magnetic Reynolds number Rm_c of the system, making the dynamo regime more difficult to reach.

The key result of this work was the identification of turbulent dynamics that constitutes an obstacle for dynamo activity, thanks to a fruitful application of the Singular Value Decomposition (SVD) to the data produced by the `DYNAMO` code. These results have produced new insights into the hydrodynamics of the flows that are important for producing the dynamo mechanism in experimental configurations, shedding light onto the temporal and spatial scales of turbulent vortices. A detailed analysis of the fluid dynamics was indeed the key issue, and the SVD constitutes a tool for determining the eigenmodes that best suit the problem. Furthermore, the SVD identifies the temporal behavior of each of these modes, and quantitatively defines their relative importance. With these techniques, we identified specific features of the turbulent flow that – in combination with the background flow – suppress magnetic field generation. In other words, we proposed an easily classifiable flow structure that is detrimental to the dynamo mechanism, and provided an additional support for large-scale turbulence suppressing the dynamos rather than small-scale fluctuations.

We also studied the effect of two strategies designed to control large scale fluctuations in our numerical model: The implementation of ring-shaped and disc-shaped baffles. The ring has already been used in experiments, and was shown to reduce turbulent resistivity in experiments, and to slightly increase the growth rates in the simulations. This study indicates that the disc is more effective at facilitating dynamo activity, as it more strongly increases the growth rates of the magnetic energy. This result can also be useful for experiments with similar topologies, since it constitutes a concrete step to take in order to overcome possible suppression mechanisms generated by fluctuations that break the so called π-symmetry of the system (i.e., a rotation of π around every axis that lies on the equatorial plane).

Future work could be focused on the details of the effects on the magnetic field of the secondary dynamics identified in this study. A three-wave interaction (between velocity modes and growing/damped magnetic modes) is playing an important role, and the SVD could be useful for elucidating these dynamics, e.g., by applying the SVD to the magnetic field and investigating correlations with the most important velocity eigenmodes. In

fact, we expect that one role of the detrimental vortices is to extract energy from the magnetic field dipolar dynamo mode and put it into other damped magnetic modes.

9.2 Basic turbulent properties in bounded geometries

Since turbulence can significantly alter the predictions of linear theory regarding the magnetic field growth rate, a further detailed analysis of the fluid dynamics of the Madison Dynamo Experiment has been carried out. Beside the SVD analysis of the simulated data, another, more general way to face this problem has been pursued. This other strategy consists of searching for possible hidden symmetries of the turbulent flow, as the investigation of the scaling properties of the structure functions can provide, with three main targets: (i) testing existing models in order to understand what kind of turbulent behavior is taking place in the system under study; (ii) testing different techniques used under other sets of hypotheses in order to suggest to the experimentalists how to extract the information from the data; (ii) providing numerically generated data that can be directly compared to the ones obtained by the MDE.

By analyzing the `DYNAMO` simulations, we have found (point (i)) that our system shows features that are best described by models like those proposed by She and Lévêque (for hydrodynamic investigations) or by Grauer, Krug, Marliani, Politano and Pouquet (for MHD intermittency [50, 51]). These models turn out to be good references for the predictions of the departure of the results from the homogeneous and isotropic theory in the MDE simulated system.

However, the main result of our study concerns point (ii). Indeed, we have shown that it is possible to successfully make use of a set of methods that are conceived for homogeneous and isotropic systems (Extended Self-Similarity, analysis of the form function), although we still do not know the physical reasons of this success. Moreover, our simulations show how MHD effects must be taken into account when the magnetic field amplitude is higher, as found in the core of the Madison sphere where a strong magnetic field can be detected.

Another sound finding concerns the investigation of time intermittency as well, which we detected by applying again the ESS technique, by analyzing the temporal behavior of the fields in specific locations. Also in this case, the best way to characterize intermittency is by means of ESS, which turns out to be a crucial tool, without which a robust estimation of the exponent and the detection of time intermittency would be technically difficult. The outcome (i.e., the ESS can be applied to the temporal analysis) can facilitate the comparison with the experiment (point (iii)). Indeed, the reason why

we check whether we can apply ESS to the temporal domain is that in the experiments it is easier to measure a temporal signal with a single probe than with an array of probes registering several signals at the same time at different locations for spatial analyses. In other words, we suggest to the experimentalist to accomplish the same kind of analysis and to see whether the same behavior can be detected. Characterizing which kind of intermittency takes place in the experiment can give further insights in future into the understanding of the system and can represent a new step towards the control of turbulent effects that hinder dynamo action.

9.3 Magnetorotational Instability

The Princeton Plasma Physics Laboratory MRI Experiment was designed to reproduce the magnetorotational instability in a cylindrical liquid gallium apparatus, driven by boundary forces (i.e., viscous coupling with the rotating walls of the cylinder). The forcing mechanism is designed to impose a Taylor-Couette profile to the working liquid. The configuration of the apparatus is relevant to astrophysics, since accretion disks share the same topology.

A two-code approach has been used within the Princeton collaboration, and this dissertation describes what has been carried out using one of the two codes. The simulations that had been done before with the `Heracles` code have kept the rotation rates constant, which modifies the magnetic Prandtl number Pm, although in the experiment Pm is a material constant while the magnetic Reynolds number Rm is modified by changing the rotation rate. Therefore, in order to run simulations that are more easily comparable to the experiments, we kept the Prandtl number constant (as low as our computational power allowed) keeping only the applied magnetic field and the rotation rates as free parameters, although the experimental Prandtl number is larger.

The main question we addressed with this two-code, fixed-Pm approach is based on a recent experimental result: A scaling relation of the azimuthal velocity in the magnetized flow of the experiment has been observed. Since the identification of the MRI is not easy from an experimental point of view, it has been supposed that this scaling behavior can be used as an indicator of the presence of a MRI mode in the experiment. For simulations with larger MRI amplitudes, both codes show a correlation between the strength of the MRI and the deviation from the azimuthal velocity scaling, confirming the hypothesis described above. In other words, data that show the highest departure from the data collapse have been produced by simulations that show also strong MRI amplitudes and this behavior can be qualitatively understood by considering that a strong MRI amplitude can appreciably modify the azimuthal component of the flow. Moreover, although the two codes develop opposite flow orientations, they show a qualitatively similar

azimuthal scaling behavior. With the results of our investigation, we were also able to give an estimate of the upper limit of the MRI amplitude in the current experimental apparatus. Differently from the experiment, we observed that the slopes of the scaled plots of the azimuthal velocities as a function of the applied magnetic field are smaller than the experimental ones.

The experimental investigation can benefit from our work for the following aspects: (i) it is worth keeping working on the data collapse discussed above as a mean of detection of the MRI; (ii) since the numerical result confirm the theoretical expectation of the order of magnitude of the MRI amplitude, measurements have to be taken in order to enhance the MRI strength (e.g., the conductivity of the endcaps can be modified or electrical currents in the flow can be added); (iii) since the extrapolation of simulated results should be carried out carefully, it would be beneficial to understand whether the high fluid Reynolds number regime of the experiment strongly affects the scenario. Concerning the last point, for instance at the experimental Reynolds numbers a turbulent boundary layer can appear (although it is missing in the simulations due to the small Reynolds number).

The investigation carried out so far show similarities and differences with the experiment and further studies are indeed needed. Nevertheless we can conclude that the first key results of our work are encouraging, since it is worth exploring in more detail the possibility of using the azimuthal velocity scaling as a suitable indicator of the MRI.

Appendices

Appendix A

Nondimensionalization of the MHD equations

In computational fluid dynamics, it is common practice to nondimensionalize the governing equations. In their nondimensional form, the equations usually depend on fewer independent control parameters than in the original form. Buckingham's Π-theorem [167] states the number of these independent control parameters. The reason of this transform is not only simplicity (since fewer parameters should be scanned in the simulations) but also in order to better grasp the physics of the problem, since recasting the equations shows the existence of *dynamic similarity*: two flows are dynamically similar if the nondimensional numbers that govern the flows have the same value, even though the parameters contained in the nondimensional numbers have different values [168]. In the following, the MHD equations are nondimensionalized, following appendix C of Reference [87].

A.1 Induction equation

In SI units, the magnetic induction equation reads

$$\frac{\partial \mathbf{B}}{\partial t} = \nabla \times (\mathbf{u} \times \mathbf{B}) + \eta \nabla^2 \mathbf{B}. \tag{A.1}$$

In order to nondimensionalize this equation, a characteristic timescale for the system under consideration has to be chosen. Usually, the eddy turnover time $\tau_v = L/U$ is chosen, where L and U are length and velocity scales characteristic of the system under consideration[1]. Another possible choice is the diffusion time $\tau_\sigma = L^2/\eta$, i.e., the timescale associated with the diffusion term of the induction equation. The equations implemented in the `SFEMaNS` code are rescaled using τ_v, whereas in the `DYNAMO` code τ_σ is chosen. Let

[1] To be more precise, L is the characteristic length of the region where the vorticity of the flow is nonzero.

us review the case with the diffusion time. Introducing the dimensionless (primed) variables

$$t = \tau_\sigma t', \tag{A.2}$$

$$\mathbf{x} = L\mathbf{x}', \quad \mathbf{u} = U\mathbf{u}', \quad \nabla = \frac{1}{L}\nabla', \tag{A.3}$$

we find

$$\frac{\eta}{L^2}\frac{\partial \mathbf{B}}{\partial t'} = \frac{U}{L}\nabla' \times (\mathbf{u}' \times \mathbf{B}) + \frac{\eta}{L^2}\nabla'^2\mathbf{B}, \tag{A.4}$$

which leads to

$$\frac{\partial \mathbf{B}}{\partial t} = Rm\nabla \times (\mathbf{u} \times \mathbf{B}) + \nabla^2\mathbf{B}, \quad Rm = \frac{UL}{\eta}, \tag{A.5}$$

where the primes have been dropped. Here, Rm is the dimensionless magnetic Reynolds number. It quantifies the importance of induction effects when compared to dissipation effects. For a given flow geometry that does not violate any anti-dynamo theorem, the value of Rm discriminates whether dynamo action takes place or not. If the eddy turnover time τ_v is used as the characteristic timescale of the system, the induction equation in nonimensional form becomes

$$\frac{\partial \mathbf{B}}{\partial t} = \nabla \times (\mathbf{u} \times \mathbf{B}) + \frac{1}{Rm}\nabla^2\mathbf{B}. \tag{A.6}$$

A.2 Navier-Stokes equation

The extended Navier-Stokes equation in SI reads

$$\frac{\partial \mathbf{u}}{\partial t} + (\mathbf{u} \cdot \nabla)\mathbf{u} = -\nabla P + \nu\nabla^2\mathbf{u} + \frac{1}{\mu_0\rho}(\nabla \times \mathbf{B}) \times \mathbf{B} + \mathbf{f}. \tag{A.7}$$

In addition to the nondimensional quantities used in the previous section, nondimensional variables for the pressure P', the magnetic field B', and the external body force f' are introduced, i.e.,

$$P = P_0P', \mathbf{B} = B_0\mathbf{B}', \mathbf{f} = f_0\mathbf{f}'. \tag{A.8}$$

Eq. (A.7) hence becomes

$$\frac{UL}{\eta}\frac{\partial \mathbf{u}'}{\partial t} + \frac{U^2}{L}(\mathbf{u}' \cdot \nabla')\mathbf{u}' = -\frac{P_0}{L}\nabla P' + \frac{\nu U}{L^2}\nabla^2\mathbf{u}' + \frac{B_0^2}{\mu_0\rho L}(\nabla' \times \mathbf{B}') \times \mathbf{B}' + f_0\mathbf{f}'. \tag{A.9}$$

By comparison with the coefficients of the advective term, the scaling factors for the pressure, the magnetic field and the body force are found to be

$$B_0^2 = U^2\mu_0\rho, P_0 = U^2, f_0 = \frac{U^2}{L}. \tag{A.10}$$

After dropping the primes and collecting the prefactors, the nondimensional extended Navier-Stokes equation reads

$$\frac{\partial \mathbf{u}}{\partial t} + Rm(\mathbf{u}\cdot\nabla)\mathbf{u} = -Rm\nabla P + Pm\nabla^2\mathbf{u} + Rm(\nabla\times\mathbf{B})\times\mathbf{B} + Rm\mathbf{f}, \quad \text{(A.11)}$$

where the magnetic Prandtl number $Pm = \nu/\eta$ is introduced. The fluid Reynolds number is included via the relation $Re = Rm/Pm$. To translate the nondimensional numbers Re and Rm (which are in fact fixed parameters specified before a run is started) to physically meaningful Reynolds numbers, a particular choice of the characteristic length and velocity scales has to be made. In the `DYNAMO` code, for instance, the characteristic length scale L is equal to the radius of the sphere, whereas for the MRI runs, the cavity width $R_2 - R_1$ is chosen. In the case of a non stationary flow, the velocity field fluctuates in space and time. Following an established convention, the characteristic velocity is chosen for the DNYAMO runs as the time-averaged rms velocity $U = \overline{\sqrt{\langle|\mathbf{u}|^2\rangle}}$, where the overline denotes temporal and the $\langle\cdot\rangle$ operator denotes spatial averaging. The time-averaging is performed during the kinematic phase of a run, i.e., when the backreaction of the magnetic field on the flow is negligible. For the MRI runs, the peak velocity is chosen, instead. This velocity is reached close to the inner cylinder, so $v_{peak} = \Omega_1 r_1$.

Appendix B

Miscellaneous mathematical results used throughout this thesis

B.1 Equation of motion of the displacement $\mathrm{d}\mathbf{x}$ embedded in the fluid

Let us consider a Lagrangian coordinate system $\{\mathbf{X}\}$ at time $t = 0$. At time $\mathrm{d}t$, the parcel that was originally at $\mathbf{X}$ will be (to the first order) at position $\mathbf{x}(\mathbf{X}, \mathrm{d}t) = \mathbf{X} + \mathbf{u}(\mathbf{X}, 0)\mathrm{d}t$, whereas the parcel that was originally at $\mathbf{X} + \mathrm{d}\mathbf{X}$ will be at position $\mathbf{x}(\mathbf{X} + \mathrm{d}\mathbf{X}, \mathrm{d}t) = \mathbf{X} + \mathrm{d}\mathbf{X} + \mathbf{u}(\mathbf{X} + \mathrm{d}\mathbf{X}, 0)\mathrm{d}t$. Therefore, the displacement $\mathrm{d}\mathbf{x}(\mathrm{d}t) = \mathbf{x}(\mathbf{X} + \mathrm{d}\mathbf{X}, \mathrm{d}t) - \mathbf{x}(\mathbf{X}, \mathrm{d}t)$ will be

$$\mathrm{d}\mathbf{x}(\mathrm{d}t) = \mathrm{d}\mathbf{X} + \Big(\mathrm{d}\mathbf{X} \cdot \frac{\partial}{\partial \mathbf{X}}\Big)\mathbf{u}(\mathbf{X}, 0)\mathrm{d}t = \Big(\mathrm{d}\mathbf{X} \cdot \frac{\partial}{\partial \mathbf{X}}\Big)\mathbf{x}(\mathbf{X}, \mathrm{d}t). \tag{B.1}$$

Eq. (2.40) directly follows. Since Eq. (B.1) represents also a solution to Eq. (2.40), analogously the solution to Eq. 2.39 is

$$\frac{B_i}{\rho}(\mathbf{x}, t) = \frac{B_j}{\rho}(\mathbf{X})\frac{\partial x_i}{\partial X_j}, \tag{B.2}$$

with summation over repeated subscripts. This result shows that magnetic field lines behave as they were "frozen" in the fluid: Indeed, if the two vectors $\mathbf{B}/\rho$ and $\mathrm{d}\mathbf{x}$ are proportional at the beginning of the motion, they will remain proportional to each other as time goes by, since they are undergoing the same transformation (via the jacobian matrix $\partial x_i/\partial X_j$). Further reading on this topic can be found in [16, 24], for instance.

B.2 An important property of the pseudoscalar α

As explained in Chapter 2, the α term of the expansion of the turbulent electromotive force $\mathcal{E}$ drives a current parallel to the mean magnetic field and this effect is the heart of dynamo action. The $k-$th component of $\mathcal{E}$ is

$$\overline{\mathbf{u}' \times \mathbf{B}'} = \overline{\mathbf{u}' \times \mathbf{B}} - \overline{\mathbf{u}' \times \overline{\mathbf{B}}} = \overline{\mathbf{u}' \times \mathbf{B}} = \epsilon_{kij} \overline{v_i' B_m \frac{\partial x_j}{\partial X_m}}, \tag{B.3}$$

having used the Lagrangian solution (B.2) and ignored density variations. Correlations between the fluctuating velocity and the Lagrangian jacobian are usually considered stronger with each other that with the magnetic field, i.e.,

$$\epsilon_{kij} \overline{v_i' B_m \frac{\partial x_j}{\partial X_m}} \simeq \epsilon_{kij} \overline{B_m} \overline{v_i' \frac{\partial x_j}{\partial X_m}}, \tag{B.4}$$

therefore the α pseudotensor becomes

$$\alpha_{km} = \epsilon_{ijk} \overline{v_i' \frac{\partial x_j}{\partial X_m}} = \epsilon_{ijk} \int_0^t \overline{v_i' \frac{\partial v_j'}{\partial X_m}} \mathrm{d}t. \tag{B.5}$$

In case of isotropic turbulence,

$$\alpha = \frac{1}{3}\alpha_{kk} = \frac{1}{3} \int_0^t \epsilon_{ijk} \int_0^t \overline{v_i' \frac{\partial v_j'}{\partial X_k}} \mathrm{d}t = -\frac{1}{3} \int_0^t \overline{\mathbf{u}' \cdot (\nabla_{\mathbf{X}} \times \mathbf{v}')} \mathrm{d}t = -\frac{1}{3} \int_0^t H' \mathrm{d}t, \tag{B.6}$$

where $\nabla_{\mathbf{X}}|_i = \frac{\partial}{\partial X_i}$ and H' is the *turbulent helicity*. H' measures how much a fluid motion is helical, where a helical motion is a left- or right-handed screw-type motion and lacks reflectional symmetry. Therefore, the α effect can take place only from turbulent fluid motion which possesses handedness: The presence of a non-zero helicity H' is an essential ingredient.

B.3 Lagrange multipliers

The method of Lagrange multipliers is used to find extrema of a function which is subjected to constraints. Let us suppose that we want to find the maximum (or the minimum) of the function $f(x_1, ..., x_n)$ with the constrain that the n independent variables of the function f satisfy $g(x_1, ..., x_n) = 0$. The necessary condition for a point $\mathbf{x}^{(0)} = (x_1^{(0)}, ..., x_n^{(0)})$ to be an extremum for f is that

$$\mathrm{d}f = \sum_{i=1}^{n} \frac{\partial f}{\partial x_i}\Big|_{\mathbf{x}=\mathbf{x}^{(0)}} \mathrm{d}x_i = 0. \tag{B.7}$$

Since the point the constraint condition is valid for point $\mathbf{x}^{(0)}$ too, we also have that

$$\mathrm{d}g = \sum_{i=1}^{n} \frac{\partial g}{\partial x_i}\Big|_{\mathbf{x}=\mathbf{x}^{(0)}} \mathrm{d}x_i = 0. \tag{B.8}$$

Equation B.8 states that we the n variables $\{x_i\}_{i=1}^{n}$ are not independent, but they are related due to Eq. B.8. In other words, it is possible to express one of the n variables in terms of the other $n-1$. If the n variables were independent, Eq. B.7 would have as result that $\partial f/\partial x_i = 0$, for every i. Instead of solving Eq. B.7 using the dependency of a one of the differential $\mathrm{d}x_j$ in terms of the others, as Eq. B.8 suggests, it is easier to solve the problem in the following, equivalent way proposed by Lagrange. By multiplying both sides of Eq. B.8 by an unknown parameter λ and by adding the result to Eq. B.7, one obtains

$$\sum_{i=1}^{n} \Big(\frac{\partial f}{\partial x_i} + \lambda \frac{\partial g}{\partial x_i}\Big)_{\mathbf{x}=\mathbf{x}^{(0)}} \mathrm{d}x_i = 0. \tag{B.9}$$

The parameter λ is known as *Lagrange multiplier* and is not determined at this stage. For this reason, we chose a suitable value for λ in such a way that one of the n coefficients of the differentials $\mathrm{d}x_i$ in parentheses in Eq. B.9 becomes zero. With this choice, only $n-1$ terms in the left-hand side member of Eq. B.9 remain non-zero. But we have seen that a set of $n-1$ variables of the original n variables is a set of linearly independent variables. Keeping all together, every single coefficient is zero, $n-1$ due to the above mentioned independency and the remaining one due to the smart choice of the adjustable parameter λ. In formulas,

$$\frac{\partial f}{\partial x_i} + \lambda \frac{\partial g}{\partial x_i} = 0,$$

for *each* i.

In practice, one solves this set of equations in terms of the unknown parameter λ and determines *a posteriori* its value by imposing that the solution satisfy the original constrain $g(x_1, ..., x_n) = 0$. This method is easily generalized for cases where m constraint equations are present. The generalization is simply carried out by introducing m Lagrange multipliers and multiplying each constrain equation by one of the λs, finally summing all these conditions together and solving the problem in a way analogous to the method described above.

B.4 Singular Value Decomposition theorem

Let A be an $M \times N$ matrix. Then $A^T A$ is symmetric and can be orthogonally diagonalized. Let $\{\mathbf{v}_1, ..., \mathbf{v}_n\}$ be an orthonormal basis for $\mathbb{R}^n$ consisting of eigenvectors of $A^T A$, and let $\lambda_1, ..., \lambda_n$ be the associated eigenvalues of $A^T A$. Then, for $1 \leq i \leq n$,

$$||A\mathbf{v}_i||^2 = (A\mathbf{v}_i)^T A\mathbf{v}_i = \mathbf{v}_i^T A^T A\mathbf{v}_i. \tag{B.10}$$

Since $\mathbf{v}_i$ is an eigenvector of $A^T A$,

$$||A\mathbf{v}_i||^2 = \mathbf{v}_i^T A^T A\mathbf{v}_i = \mathbf{v}_i^T \lambda_i \mathbf{v}_i = \lambda_i, \tag{B.11}$$

because $\mathbf{v}_i$ is an unit vector. This equation chain proofs that the eigenvalues of $A^T A$ are non-negative. With a suitable reordering of the orthonormal basis, we can assume, without loss of generality, that $\lambda_1 \geq \lambda_2 \geq ... \geq \lambda_n \geq 0$. The square roots of the eigenvalues λ_i of $A^T A$ are called *singular values of the matrix* A. Let us call them σ_i. By equation B.11, we find that they represent the length of the vectors $A\mathbf{v}_1, ..., A\mathbf{v}_n$. It is possible to prove (see Ref. [155]) the following

Theorem. *Suppose* $\{\mathbf{v}_1, ..., \mathbf{v}_n\}$ *is an orthonormal basis of* $\mathbb{R}^n$ *consisting of eigenvectors of* $A^T A$*, arranged in such a way that the corresponding eigenvalues of* $A^T A$ *satisfy* $\lambda_1 \geq \lambda_2 \geq ... \geq \lambda_n$*, and suppose* A *has* r *non-zero singular values. Then* $\{A\mathbf{v}_1, ..., A\mathbf{v}_r\}$ *is an orthogonal basis for* $\mathrm{Col}(A)$ *(i.e., the column space of* A*, the set* $\mathrm{Col}(A)$ *of all linear combinations of the columns of* A*) and* $\mathrm{rank}(A) = r$*.*

Thanks to this result, under the same hypotheses, we prove the

Singular Value Decomposition Theorem. *Let* A *be an* $M \times N$ *matrix with* $\mathrm{rank}(A) = r$*. Then there exists an* $M \times N$ *matrix* Σ *of the form*

$$\Sigma = \begin{pmatrix} D & 0 \\ 0 & 0 \end{pmatrix}$$

where D *is an* $r \times r$ *diagonal matrix and* $r \leq \min(m, n)$*, for which the diagonal entries in* D *are the first* r *singular values of* A*, i.e.,* $\sigma_1 \geq \sigma_2 \geq ... \geq \sigma_r > 0$*, and there exist an* $m \times m$ *orthogonal matrix* U *and an* $n \times n$ *orthogonal matrix* V *such that*

$$A = U\Sigma V^T. \tag{B.12}$$

Proof. The previous Theorem proved that the set $\{A\mathbf{v}_1, ..., A\mathbf{v}_r\}$ is an orthogonal basis of $\mathrm{Col}(A)$. By normalizing these vectors, we obtained a new set $\{\mathbf{u}_1, ..., \mathbf{u}_r\}$ with

$$\mathbf{u}_i = \frac{A\mathbf{v}_i}{||A\mathbf{v}_i||} = \frac{A\mathbf{v}_i}{\sigma_i},$$

or

$$A\mathbf{v}_i = \sigma_i \mathbf{u}_i, \tag{B.13}$$

for $0 \leq i \leq r$. By extending this new set $\{\mathbf{u}_i\}_{i=1}^{r}$ to an orthonormal basis $\{\mathbf{u}_i\}_{i=1}^{m}$ of $\mathbb{R}^m$, we consider the matrices $U = (\mathbf{u}_1\ \mathbf{u}_2\ ...\ \mathbf{u}_m)$ and $V = (\mathbf{v}_1\ \mathbf{v}_2\ ...\ \mathbf{v}_n)$, which are orthogonal by construction. Since only r eigenvalues λ_i are nonzero (as in the previous theorem) and since they represent the length of the vectors $A\mathbf{v}_i$, it follows that $AV = (A\mathbf{v}_1\ ...\ A\mathbf{v}_r\ \mathbf{0}\ ...\ \mathbf{0})$. From Eq. B.13, we have then that $AV = (\sigma_1\mathbf{u}_1\ ...\ \sigma_r\mathbf{u}_r\ \mathbf{0}\ ...\ \mathbf{0})$. It is then trivial to show that $AV = \Sigma U$, and, since $V^{-1} = V^T$, we have that $\boxed{A = U\Sigma V^T}$. Q.E.D.

□

As noticed in [155], the matrices U and V are not uniquely determined by A, but the diagonal entries of σ are necessarily the singular values of A. In Chapter 8, the rows of U and the columns of V^T represent respectively the spatial POD modes and the temporal time traces associated with the POD modes, while N_{POD} has the role of r, N_{tot} the role of M and N_t that of N. It is worth noticing that all this analysis can be carried out in $\mathbb{C}^n$, where the operation of complex conjugation should be taken into account in the scalar products and where the matrices are in this case unitary instead of orthogonal.

B.5 Origin of the Stewartson layer: The Taylor-Proudman Theorem

The Taylor-Proudman theorem states that in a steady rotating flow of an inviscid and homogeneous fluid, if the angular velocity of the rotation is high enough, then the resulting flow is two-dimensional. In the following, the angular velocity vector will be denoted by $\mathbf{\Omega} = (0, 0, \Omega_z)$ (in cartesian coordinates); its modulus Ω must be large enough, so that that the Coriolis force dominates the inertial terms (the so-called small Rossby-number limit).

Proof. Let us consider the inviscid Navier Stokes equations in steady state (i.e., $\partial/\partial t = 0$) in the frame co-rotating with the fluid,

$$\rho(\mathbf{u} \cdot \nabla)\mathbf{u} = -2\rho\mathbf{\Omega} \times \mathbf{u} - \nabla P, \tag{B.14}$$

where the effective pressure P is related to the fluid pressure p via $P = p + \rho\Phi$ (Φ is the gravitational potential). By neglecting the advective term and taking the curl of the last equation in order to get rid of the pressure term, we get

$$(\mathbf{\Omega} \cdot \nabla)\mathbf{u} = 0, \tag{B.15}$$

since Ω_z is constant. This means that

$$\frac{\partial \mathbf{u}}{\partial z} = 0, \tag{B.16}$$

i.e., all three components of the velocity field are independent of z. Moreover, by taking the scalar product of Eq. (B.14), we have

$$(\mathbf{\Omega} \cdot \nabla) P = 0, \tag{B.17}$$

i.e., also the pressure is independent of z. The theorem hence states that motions whose timescale is small compared to the one associated to Ω become independent of z.

□

Appendix C

Tabular overview of the simulated relative exponents

Table C.1: scaling exponents (relative to $\zeta(3)$) of *longitudinal* structure functions. $\boxed{\theta = 90}^{\circ}$.

		$\zeta(1)/\zeta(3)$	$\zeta(2)/\zeta(3)$	$\zeta(4)/\zeta(3)$	$\zeta(5)/\zeta(3)$
Rm_0=40	$B_0 = 0.01$	0.385 ± 0.012	0.709 ± 0.010	1.270 ± 0.014	1.53 ± 0.03
	$B_0 = 0.03$	0.39 ± 0.03	0.705 ± 0.025	1.28 ± 0.04	1.56 ± 0.08
	$B_0 = 0.07$	0.377 ± 0.016	0.702 ± 0.011	1.283 ± 0.012	1.561 ± 0.024
	$B_0 = 0.15$	0.338 ± 0.03	0.671 ± 0.003	1.326 ± 0.005	1.650 ± 0.012
Rm_0=200	$B_0 = 0.01$	0.387 ± 0.014	0.715 ± 0.014	1.253 ± 0.024	1.48 ± 0.05
	$B_0 = 0.07$	0.33395 ± 0.00008	0.6671 ± 0.0007	1.33267 ± 0.00013	1.665 ± 0.003
	$B_0 = 0.15$	0.339 ± 0.012	0.675 ± 0.009	1.311 ± 0.009	1.611 ± 0.017

Table C.2: scaling exponents (relative to $\zeta(3)$) of *transverse* (along $\hat{\mathrm{e}}_\theta$) structure functions. $\boxed{\theta = 90}^{\circ}$.

		$\zeta(1)/\zeta(3)$	$\zeta(2)/\zeta(3)$	$\zeta(4)/\zeta(3)$	$\zeta(5)/\zeta(3)$
Rm_0=40	$B_0 = 0.01$	0.387 ± 0.020	0.720 ± 0.018	1.24 ± 0.03	1.46 ± 0.07
	$B_0 = 0.03$	0.362 ± 0.014	0.688 ± 0.010	1.303 ± 0.01	1.60 ± 0.03
	$B_0 = 0.07$	0.332 ± 0.024	0.663 ± 0.021	1.34 ± 0.03	1.68 ± 0.07
	$B_0 = 0.15$	0.34 ± 0.02	0.680 ± 0.016	1.31 ± 0.02	1.63 ± 0.04
Rm_0=200	$B_0 = 0.01$	0.358 ± 0.006	0.692 ± 0.006	1.286 ± 0.013	1.56 ± 0.03
	$B_0 = 0.07$	0.37 ± 0.05	0.71 ± 0.05	1.25 ± 0.09	1.46 ± 0.22
	$B_0 = 0.15$	0.369 ± 0.024	0.710 ± 0.010	1.241 ± 0.022	1.45 ± 0.05

Table C.3: scaling exponents (relative to $\zeta(3)$) of *transverse* (along $\hat{e}_\phi$) structure functions. $\boxed{\theta = 90}^\circ$.

		$\zeta(1)/\zeta(3)$	$\zeta(2)/\zeta(3)$	$\zeta(4)/\zeta(3)$	$\zeta(5)/\zeta(3)$
Rm_0=40	$B_0 = 0.01$	0.354 ± 0.012	0.686 ± 0.013	1.30 ± 0.03	1.58 ± 0.06
	$B_0 = 0.03$	0.350 ± 0.012	0.682 ± 0.013	1.311 ± 0.024	1.62 ± 0.05
	$B_0 = 0.07$	0.395 ± 0.024	0.724 ± 0.019	1.239 ± 0.0026	1.46 ± 0.05
	$B_0 = 0.15$	0.340 ± 0.012	0.667 ± 0.011	1.339 ± 0.017	1.68 ± 0.03
Rm_0=200	$B_0 = 0.01$	0.424 ± 0.014	0.749 ± 0.013	1.197 ± 0.022	1.36 ± 0.05
	$B_0 = 0.07$	0.382 ± 0.015	0.726 ± 0.020	1.22 ± 0.05	1.43 ± 0.12
	$B_0 = 0.15$	0.431 ± 0.015	0.756 ± 0.015	1.20 ± 0.03	1.37 ± 0.07

Table C.4: scaling exponents (relative to $\zeta(3)$) of *longitudinal* structure functions. $\boxed{\theta = 121}^\circ$.

		$\zeta(1)/\zeta(3)$	$\zeta(2)/\zeta(3)$	$\zeta(4)/\zeta(3)$	$\zeta(5)/\zeta(3)$
Rm_0=40	$B_0 = 0.01$	0.306 ± 0.014	0.642 ± 0.013	1.373 ± 0.023	1.75 ± 0.06
	$B_0 = 0.03$	0.352 ± 0.024	0.681 ± 0.019	1.31 ± 0.03	1.63 ± 0.06
	$B_0 = 0.07$	0.344 ± 0.014	0.676 ± 0.011	1.319 ± 0.016	1.63 ± 0.04
	$B_0 = 0.15$	0.37 ± 0.03	0.70 ± 0.02	1.29 ± 0.03	1.57 ± 0.06
Rm_0=200	$B_0 = 0.01$	0.344 ± 0.010	0.680 ± 0.009	1.297 ± 0.016	1.57 ± 0.04
	$B_0 = 0.07$	0.343 ± 0.024	0.676 ± 0.017	1.317 ± 0.021	1.63 ± 0.04
	$B_0 = 0.15$	0.37 ± 0.05	0.70 ± 0.05	1.286 ± 0.025	1.56 ± 0.06

Table C.5: scaling exponents (relative to $\zeta(3)$) of *transverse* (along $\hat{e}_\theta$) structure functions. $\boxed{\theta = 121}^\circ$.

		$\zeta(1)/\zeta(3)$	$\zeta(2)/\zeta(3)$	$\zeta(4)/\zeta(3)$	$\zeta(5)/\zeta(3)$
Rm_0=40	$B_0 = 0.01$	0.397 ± 0.018	0.723 ± 0.017	1.24 ± 0.03	1.46 ± 0.07
	$B_0 = 0.03$	0.389 ± 0.006	0.706 ± 0.010	1.275 ± 0.011	1.54 ± 0.03
	$B_0 = 0.07$	0.382 ± 0.019	0.703 ± 0.017	1.28 ± 0.03	1.56 ± 0.06
	$B_0 = 0.15$	0.334 ± 0.006	0.667 ± 0.006	1.332 ± 0.010	1.66 ± 0.03
Rm_0=200	$B_0 = 0.01$	0.389 ± 0.018	0.717 ± 0.023	1.24 ± 0.06	1.46 ± 0.14
	$B_0 = 0.07$	0.357 ± 0.005	0.686 ± 0.004	1.305 ± 0.006	1.601 ± 0.015
	$B_0 = 0.15$	0.361 ± 0.008	0.697 ± 0.007	1.275 ± 0.009	1.535 ± 0.022

Table C.6: scaling exponents (relative to $\zeta(3)$) of *transverse* (along $\hat{e}_\phi$) structure functions. $\boxed{\theta = 121}^\circ$.

		$\zeta(1)/\zeta(3)$	$\zeta(2)/\zeta(3)$	$\zeta(4)/\zeta(3)$	$\zeta(5)/\zeta(3)$
Rm_0=40	$B_0 = 0.01$	0.375 ± 0.016	0.698 ± 0.012	1.294 ± 0.017	1.58 ± 0.04
	$B_0 = 0.03$	0.333 ± 0.016	0.669 ± 0.013	1.328 ± 0.020	1.65 ± 0.04
	$B_0 = 0.07$	0.360 ± 0.011	0.688 ± 0.011	1.313 ± 0.024	1.63 ± 0.06
	$B_0 = 0.15$	0.35 ± 0.03	0.683 ± 0.023	1.31 ± 0.03	1.61 ± 0.08
Rm_0=200	$B_0 = 0.01$	0.355 ± 0.019	0.689 ± 0.021	1.28 ± 0.06	1.53 ± 0.14
	$B_0 = 0.07$	0.335 ± 0.004	0.669 ± 0.004	1.329 ± 0.008	1.656 ± 0.021
	$B_0 = 0.15$	0.354 ± 0.015	0.676 ± 0.011	1.333 ± 0.015	1.67 ± 0.03

Table C.7: predicted exponents of She & Leveque model and of Kolmogorov classical analysis.

	She & Leveque	Kolmogorov
$\zeta(1)/\zeta(3)$	0.364	0.333
$\zeta(2)/\zeta(3)$	0.696	0.667
$\zeta(3)/\zeta(3)$	1.000	1.000
$\zeta(4)/\zeta(3)$	1.280	1.333
$\zeta(5)/\zeta(3)$	1.538	1.667

Appendix D

Time intermittency: Calculated exponents

Table D.1: scaling exponents (relative to $\zeta(3)$) of $\langle|u_r(t+\tau) - u_r(t)|^p\rangle$. $\theta = 121°$, $r_i = 250$.

		$\zeta(1)/\zeta(3)$	$\zeta(2)/\zeta(3)$	$\zeta(4)/\zeta(3)$	$\zeta(5)/\zeta(3)$
Rm_0=40	$B_0 = 0.01$	0.347 ± 0.002	0.6819 ± 0.0018	1.293 ± 0.009	1.56 ± 0.028
	$B_0 = 0.03$	0.354 ± 0.005	0.688 ± 0.005	1.29 ± 0.01	1.58 ± 0.02
	$B_0 = 0.07$	0.351 ± 0.005	0.685 ± 0.006	1.29 ± 0.014	1.57 ± 0.03
	$B_0 = 0.15$	0.350 ± 0.003	0.654 ± 0.005	1.349 ± 0.006	1.699 ± 0.013
Rm_0=200	$B_0 = 0.01$	0.408 ± 0.009	0.750 ± 0.010	1.160 ± 0.022	1.26 ± 0.05
	$B_0 = 0.07$	0.3338 ± 0.0018	0.669 ± 0.0024	1.311 ± 0.015	1.59 ± 0.23
	$B_0 = 0.15$	0.389 ± 0.006	0.694 ± 0.004	1.313 ± 0.011	1.63 ± 0.10

Table D.2: scaling exponents (relative to $\zeta(3)$) of $\langle|u_\theta(t+\tau) - u_\theta(t)|^p\rangle$. $\theta = 121°$, $r_i = 250$.

		$\zeta(1)/\zeta(3)$	$\zeta(2)/\zeta(3)$	$\zeta(4)/\zeta(3)$	$\zeta(5)/\zeta(3)$
Rm_0=40	$B_0 = 0.01$	0.378 ± 0.008	0.726 ± 0.015	1.19 ± 0.03	1.37 ± 0.07
	$B_0 = 0.03$	0.371 ± 0.013	0.700 ± 0.011	1.288 ± 0.014	1.57 ± 0.03
	$B_0 = 0.07$	0.355 ± 0.007	0.688 ± 0.007	1.296 ± 0.010	1.582 ± 0.023
	$B_0 = 0.15$	0.345 ± 0.003	0.675 ± 0.002	1.323 ± 0.003	1.646 ± 0.006
Rm_0=200	$B_0 = 0.01$	0.386 ± 0.011	0.717 ± 0.011	1.24 ± 0.03	1.461 ± 0.006
	$B_0 = 0.07$	0.347 ± 0.004	0.681 ± 0.005	1.298 ± 0.013	1.58 ± 0.03
	$B_0 = 0.15$	0.437 ± 0.017	0.734 ± 0.011	1.262 ± 0.012	1.52 ± 0.03

Table D.3: scaling exponents (relative to $\zeta(3)$) of $\langle|u_\phi(t+\tau)-u_\phi(t)|^p\rangle$. $\theta = 121°$, $r_i = 250$.

		$\zeta(1)/\zeta(3)$	$\zeta(2)/\zeta(3)$	$\zeta(4)/\zeta(3)$	$\zeta(5)/\zeta(3)$
Rm_0=40	$B_0 = 01$	0.350 ± 0.003	0.6860 ± 0.0028	1.284 ± 0.011	1.54 ± 0.03
	$B_0 = 0.03$	0.351 ± 0.004	0.688 ± 0.004	1.28 ± 0.01	1.525 ± 0.025
	$B_0 = 0.07$	0.350 ± 0.004	0.685 ± 0.004	1.298 ± 0.0084	1.585 ± 0.019
	$B_0 = 0.15$	0.343 ± 0.007	0.675 ± 0.005	1.323 ± 0.006	1.643 ± 0.012
Rm_0=200	$B_0 = 0.01$	0.400 ± 0.005	0.735 ± 0.005	1.194 ± 0.011	1.34 ± 0.03
	$B_0 = 0.07$	0.333 ± 0.002	0.667 ± 0.003	1.316 ± 0.015	1.61 ± 0.04
	$B_0 = 0.15$	0.44 ± 0.02	0.73 ± 0.016	1.273 ± 0.016	1.55 ± 0.03

Table D.4: scaling exponents (relative to $\zeta(3)$) of $\langle|u_r(t+\tau)-u_r(t)|^p\rangle$. $\theta = 121°$, $r_i = 400$.

		$\zeta(1)/\zeta(3)$	$\zeta(2)/\zeta(3)$	$\zeta(4)/\zeta(3)$	$\zeta(5)/\zeta(3)$
Rm_0=40	$B_0 = 0.01$	0.392 ± 0.009	0.738 ± 0.0017	1.18 ± 0.03	1.33 ± 0.07
	$B_0 = 0.03$	0.346 ± 0.004	0.682 ± 0.004	1.30 ± 0.08	1.59 ± 0.02
	$B_0 = 0.07$	0.356 ± 0.004	0.690 ± 0.004	1.28 ± 0.007	1.56 ± 0.02
	$B_0 = 0.15$	0.364 ± 0.010	0.694 ± 0.010	1.288 ± 0.016	1.57 ± 0.004
Rm_0=200	$B_0 = 0.01$	0.432 ± 0.018	0.762 ± 0.018	1.17 ± 0.03	1.31 ± 0.07
	$B_0 = 0.07$	0.3348 ± 0.0003	0.66778 ± 0.00013	1.33378 ± 0.00005	1.6703 ± 0.0003
	$B_0 = 0.15$	0.464 ± 0.025	0.752 ± 0.013	1.240 ± 0.012	1.472 ± 0.10

Table D.5: scaling exponents (relative to $\zeta(3)$) of $\langle|u_\theta(t+\tau)-u_\theta(t)|^p\rangle$. $\theta = 121°$, $r_i = 400$.

		$\zeta(1)/\zeta(3)$	$\zeta(2)/\zeta(3)$	$\zeta(4)/\zeta(3)$	$\zeta(5)/\zeta(3)$
Rm_0=40	$B_0 = 0.15$	0.382 ± 0.012	0.718 ± 0.012	1.23 ± 0.02	1.43 ± 0.04
	$B_0 = 0.03$	0.361 ± 0.007	0.699 ± 0.008	1.273 ± 0.016	1.54 ± 0.04
	$B_0 = 0.07$	0.356 ± 0.006	0.694 ± 0.007	1.273 ± 0.016	1.53 ± 0.04
	$B_0 = 0.15$	0.359 ± 0.005	0.687 ± 0.004	1.302 ± 0.006	1.596 ± 0.005
Rm_0=200	$B_0 = 0.01$	0.44 ± 0.03	0.77 ± 0.03	1.18 ± 0.05	1.36 ± 0.10
	$B_0 = 0.07$	0.3336 ± 0.0024	0.668 ± 0.003	1.313 ± 0.016	1.60 ± 0.04
	$B_0 = 0.15$	0.55 ± 0.07	0.81 ± 0.05	1.17 ± 0.06	1.34 ± 0.12

Table D.6: scaling exponents (relative to $\zeta(3)$) of $\langle|u_\phi(t+\tau)-u_\phi(t)|^p\rangle$. $\theta = 121°$, $r_i = 400$.

		$\zeta(1)/\zeta(3)$	$\zeta(2)/\zeta(3)$	$\zeta(4)/\zeta(3)$	$\zeta(5)/\zeta(3)$
Rm_0=40	$B_0 = 0.15$	0.416 ± 0.011	0.759 ± 0.012	1.159 ± 0.025	1.29 ± 0.05
	$B_0 = 0.03$	0.366 ± 0.009	0.700 ± 0.010	1.27 ± 0.02	1.53 ± 0.04
	$B_0 = 0.07$	0.3365 ± 0.0009	0.6697 ± 0.0007	1.3297 ± 0.0010	1.659 ± 0.003
	$B_0 = 0.15$	0.323 ± 0.006	0.650 ± 0.008	1.380 ± 0.019	1.78 ± 0.04
Rm_0=200	$B_0 = 0.01$	0.405 ± 0.014	0.731 ± 0.011	1.228 ± 0.019	1.43 ± 0.04
	$B_0 = 0.07$	0.3301 ± 0.0011	0.6650 ± 0.0006	1.33414 ± 0.00028	1.6682 ± 0.0005
	$B_0 = 0.15$	0.55 ± 0.07	0.81 ± 0.05	1.17 ± 0.06	1.33 ± 0.12

Bibliography

[1] J. Larmor, Rep. Brit. Assoc. Adv. Sci. **87**, 159 (1919).

[2] T. G. Cowling, Mon. Not. R. Astron. Soc. **94**, 39 (1933).

[3] G. Backus, Ann. Phys. **4**, 372 (1958).

[4] A. Herzenberg, Philos. Tr. Roy. Soc. S. A **250**, 543 (1958).

[5] C. F. V. Weizsäcker, Zeitschrift Naturforschung Teil A **3**, 524 (1948).

[6] H. Ji, M. Burin, E. Schartman, and J. Goodman, Nature **444**, 281 (2006).

[7] E. Velikhov, Sov. Phys. JETP **36**, 995 (1959).

[8] S. Chandrasekhar, Proceedings of the National Academy of Science **46**, 253 (1960).

[9] K. Fricke, Astronomy and Astrophysics **1**, 388 (1969).

[10] D. J. Acheson and R. Hide, Reports on Progress in Physics **36**, 159 (1973).

[11] D. J. Acheson and M. P. Gibbons, Royal Society of London Philosophical Transactions Series A **289**, 249 (1978).

[12] S. A. Balbus and J. F. Hawley, Astrophysical Journal **376**, 214 (1991).

[13] H. K. Moffatt, *Magnetic field generation in electrically conducting fluids* (Cambridge University Press, Cambridge, 1978).

[14] S. A. Balbus and J. F. Hawley, Rev. Mod. Phys. **70**, 1 (1998).

[15] J. D. Jackson, *Classical Electrodynamics*, 3 ed. (Wiley, 1998).

[16] P. Sturrock, *Plasma Physics: An Introduction to the Theory of Astrophysical, Geophysical and Laboratory Plasmas,* Stanford-Cambridge Program (Cambridge University Press, 1994).

[17] P. Kundu and I. Cohen, *Fluid Mechanics* (Elsevier Science, 2010).

[18] G. K. Batchelor, *An Introduction to Fluid Dynamics* (Cambridge University Press, 1967).

[19] L. D. Landau and E. M. Lifshitz, *Fluid Mechanics*volume 6 of *Course of Theoretical Physics*, 2 ed. (Pergamon Press, 1987).

[20] C. Fletcher, *Computational Techniques for Fluid Dynamics*, Computational Techniques for Fluid Dynamics No. v. 1 (Springer-Verlag, 1991).

[21] H. Lamb and R. Caflisch, *Hydrodynamics*Cambridge Mathematical Library (Cambridge University Press, 1993).

[22] D. Biskamp, *Nonlinear Magnetohydrodynamics*Cambridge Monographs on Plasma Physics (Cambridge University Press, 1997).

[23] R. P. Feynman, R. B. Leighton, and M. Sands, *The Feynman Lectures on Physics*volume 2 (Addison-Wesley, 1964).

[24] E. Parker, *Cosmical magnetic fields: their origin and their activity*International series of monographs on physics (Clarendon Press, 1979).

[25] C. Gissinger, H. Ji, and J. Goodman, Phys. Rev. E **84**, 026308 (2011).

[26] S. Anzellini, Science **340**, 464 (2013).

[27] R. Boehler, Nature **363**, 534 (1993).

[28] M. Steenbeck, F. Krause, and K.-H. Rädler, Z. Nat. **21**, 369 (1966).

[29] C. A. Jones, Dynamo Theory, in *Dynamos*, edited by P. Cardin and L. F. Cugliandolo, volume 88 of *Les Houches Summer School Proceedings*, p. 45, Elsevier, 2008.

[30] K. Krause and R. Rädler, *Mean field magnetohydrodynamics and dynamo theory* (Pergamon Press, Oxford, 1980).

[31] Y. B. Zeldovich, Sov. Phys. JETP **4**, 460 (1957).

[32] E. Bullard and H. Gellman, Proc. R. Soc. Lond. A **247**, 213 (1954).

[33] P. A. Davidson, *Turbulence - An introduction for scientists and engineers* (Oxford University Press, 2004).

[34] A. N. Kolmogorov, Dokl. Akad. Nauk SSSR **30**, 9 (1941), reprinted in Proc. R. Soc. Lond. A, 434, 9, 1991.

[35] A. N. Kolmogorov, Dokl. Akad. Nauk SSSR **32**, 16 (1941), reprinted in Proc. R. Soc. Lond. A, 434, 15, 1991.

[36] L. F. Richardson, *Weather Prediction by Numerical Process* (Cambridge University Press, Cambridge, 1922).

[37] A. S. Monin and A. M. Yaglom, *Statistical Fluid Mechanics* (Cambridge, MA: The MIT Press, 1975).

[38] U. Frisch, *Turbulence. The Legacy of A. N. Kolmogorov.* (Cambridge University Press, 1995).

[39] R. H. Kraichnan, Phys. Fluids **8**, 1385 (1965).

[40] P. S. Iroshnikov, Astron. Zh. **40**, 742 (1963).

[41] F. Anselmet, Y. Gagne, E. J. Hopfinger, and R. A. Antonia, Journal of Fluid Mechanics **140**, 63 (1984).

[42] R. Benzi, G. Paladin, G. Parisi, and A. Vulpiani, Journal of Physics A: Mathematical and General **17**, 3521 (1984).

[43] G. P. Romano and R. A. Antonia, Journal of Fluid Mechanics **436**, 231 (2001).

[44] C. Meneveau and K. R. Sreenivasan, Nuclear Physics B Proceedings Supplements **2**, 49 (1987).

[45] T. S. Horbury and A. Balogh, Nonlinear Processes in Geophysics **4**, 185 (1997).

[46] R. Grauer and C. Marliani, Physica Scripta Volume T **67**, 38 (1996).

[47] L. F. Burlaga, Journal of Geophys. Res. **96**, 5847 (1991).

[48] L. F. Burlaga, Journal of Geophys. Res. **97**, 4283 (1992).

[49] E. Marsch and S. Liu, Annales Geophysicae **11**, 227 (1993).

[50] R. Grauer, J. Krug, and C. Marliani, Physics Letters A **195**, 335 (1994).

[51] H. Politano and A. Pouquet, Phys. Rev. E **52**, 636 (1995).

[52] Z.-S. She and E. Leveque, Physical Review Letters **72**, 336 (1994).

[53] U. Frisch, P.-L. Sulem, and M. Nelkin, Journal of Fluid Mechanics **87**, 719 (1978).

[54] S. Sridhar and P. Goldreich, Astrophys. J. **432**, 612 (1994).

[55] P. Goldreich and S. Sridhar, Astrophys. J. **438**, 763 (1995).

[56] W.-C. Müller, Magnetohydrodynamic turbulence, in *Lect. Notes Phys.*, edited by W. Hillebrandt and F. Kupka, volume 756 of *Lecture Notes in Physics*, pp. 223–254, Springer Berlin, 1995.

[57] D. Biskamp, *Magnetohydrodynamical Turbulence* (Cambridge University Press, Cambridge, 2003).

[58] P. Cortet *et al.*, Phys. Fluids **21**, 025104 (2009).

[59] W. Liu, Ph.D. Thesis, Princeton University (2007).

[60] D. Richard, *Instabilités Hydrodynamiques dans les Ecoulements en Rotation Différentielle*, PhD thesis, Univ. Paris 7, 2001.

[61] G. I. Taylor, Proceedings of the Royal Society of London. Series A, Mathematical and Physical Sciences **157**, pp. 546 (1936).

[62] M. Couette, *Étude sur le frottement des liquides* (, 1890).

[63] G. Taylor, Phil. Trans. A **223** (1923).

[64] C. D. Andereck, S. S. Liu, and H. L. Swinney, Journal of Fluid Mechanics **164**, 155.

[65] D. Coles and C. van Atta, Journal of Fluid Mechanics **25**, 513 (1966).

[66] A. Kageyama, H. Ji, J. Goodman, F. Chen, and E. Shoshan, Journal of the Physical Society of Japan **73**, 2424 (2004), arXiv:physics/0405123.

[67] J. Abshagen *et al.*, Theoretical and Computational Fluid Dynamics **18**, 129 (2004).

[68] F. Wendt, *Turbulente Strömungen zwischen zwei rotierenden konaxialen Zylindern* (Pöppinghaus, 1933).

[69] L. Rayleigh, Proceedings of the Royal Society of London. Series A **93**, 148 (1917).

[70] M. J. Burin *et al.*, Experiments in Fluids **40**, 962 (2006).

[71] K. Stewartson, Journal of Fluid Mechanics **3**, 17 (1957).

[72] R. Hollerbach, Journal of Fluid Mechanics **492** (2003).

[73] R. Hollerbach and A. Fournier, AIP Conf.Proc. 733: 114-121 (2004), arXiv:astro-ph/0506081.

[74] S. Fromang, P. Hennebelle, and R. Teyssier, Astronomy and Astrophysics **457**, 371 (2006), arXiv:astro-ph/0607230.

[75] A. Roach, Ph.D. Thesis, Princeton University (2013).

[76] E. J. Spence, M. D. Nornberg, C. M. Jacobson, R. D. Kendrick, and C. B. Forest, Phys. Rev. Lett. **96**, 055002 (2006).

[77] M. Berhanu *et al.*, Europhys. Lett. **77**, 59001 (2007).

[78] R. Monchaux *et al.*, Phys. Rev. Lett. **98**, 044502 (2007).

[79] F. Ravelet *et al.*, Phys. Rev. Lett. **101**, 074502 (2008).

[80] M. L. Dudley and R. W. James, Proc. R. Soc. Lond. A **425**, 407 (1989).

[81] E. J. Kaplan *et al.*, Phys. Rev. Lett. **106**, 254502 (2011).

[82] C. B. Forest *et al.*, Magnetohydrodynamics **38** (2002).

[83] M. D. Nornberg, E. J. Spence, R. D. Kendrick, C. M. Jacobson, and C. B. Forest, Phys. Plasmas **13**, 055901 (2006).

[84] K. Rahbarnia *et al.*, The Astrophysical Journal **759**, 80 (2012).

[85] E. J. Spence *et al.*, Phys. Rev. Lett. **98**, 164503 (2007).

[86] M. D. Nornberg, E. J. Spence, R. D. Kendrick, C. M. Jacobson, and C. B. Forest, Phys. Rev. Lett. **97**, 044503 (2006).

[87] K. Reuter, *Numerical investigations of turbulent dynamo excitation in a spherical MHD system*, PhD thesis, Westfälischen Wilhelms-Universität Münster, 2010.

[88] M. D. Nornberg, *The role of MHD turbulence in magnetic self-excitation: a study of the Madison Dynamo Experiment*, PhD thesis, University of Wisconsin-Madison, 2006.

[89] E. J. Spence, *Experimental observation of fluctuation-driven mean magnetic fields in the Madison Dynamo Experiment*, PhD thesis, University of Wisconsin-Madison, 2006.

[90] C. Gissinger, J. Goodman, and H. Ji, Physics of Fluids **24**, 074109 (2012), 1201.1853.

[91] J. Weissmann *et al.*, (2013), *to be submitted*.

[92] G. Karypis and V. Kumar, MeTis: Unstructured Graph Partitioning and Sparse Matrix Ordering System, Version 4.0, `http://www.cs.umn.edu/~metis`, 2009.

[93] J.-L. Guermond, R. Laguerre, J. Léorat, and C. Nore, Journal of Computational Physics **228**, 2739 (2009).

[94] K. Reuter, F. Jenko, C. B. Forest, and A. R. Bayliss, Comput. Phys. Commun. **179**, 245 (2008).

[95] K. Reuter, F. Jenko, A. Tilgner, and C. B. Forest, Phys. Rev. E **80**, 056304 (2009).

[96] K. Reuter, F. Jenko, and C. B. Forest, New Journal of Physics **13**, 073019 (2011).

[97] K. Reuter, F. Jenko, and C. B. Forest, New J. Phys. **11**, 013027 (2009).

[98] R. A. Bayliss, C. B. Forest, M. D. Nornberg, E. J. Spence, and P. W. Terry, Phys. Rev. E **75**, 026303 (2007).

[99] A. B. Bayliss, *Numerical simulations of current generation and dynamo excitation in a mechanically-forced, turbulent flow*, PhD thesis, University of Wisconsin-Madison, 2006.

[100] A. Tilgner, Phys. Rev. Lett. **100**, 128501 (2008).

[101] C. G. Canuto, M. Y. Hussaini, A. Quarteroni, and T. A. Zang, *Spectral Methods in Fluid Dynamics* (Springer, New York, 1988).

[102] A. Ribeiro, *Approche spectrale/éléments finis pour des problèmes de magnétohydrodynamique non linéaires 2010*, PhD thesis, Université Paris-Sud, LIMSI, Orsay, 2010.

[103] J. Weissmann, Magnetohydrodynamic Simulations for the Princeton MRI Experiment, Master's thesis, Technische Universität München, 2013.

[104] R. Benzi *et al.*, Phys. Rev. E **48**, R29 (1993).

[105] R. Benzi, S. Ciliberto, C. Baudet, and G. R. Chavarria, Physica D: Nonlinear Phenomena **80**, 385 (1995).

[106] M. Briscolini, P. Santangelo, S. Succi, and R. Benzi, Phys. Rev. E **50**, R1745 (1994).

[107] E. Ringuet, C. Rozé, and G. Gouesbet, Phys. Rev. E **47**, 1405 (1993).

[108] V. Carbone, R. Bruno, and P. Veltri, Geophys. Res. Lett. **23**, 121 (1996).

[109] C. Salem, A. Mangeney, S. D. Bale, and P. Veltri, The Astrophysical Journal **702**, 537 (2009).

[110] M. Wilczek, F. Jenko, and R. Friedrich, Phys. Rev. E **77**, 056301 (2008).

[111] P. W. Terry and K. W. Smith, apj **665**, 402 (2007), arXiv:astro-ph/0702177.

[112] E. Falgarone, Small-scale Structures in Fluids and MHD, volume 462 of *Lecture Notes in Physics*, p. 337, Springer Berlin, 2009.

[113] S. Douady, Y. Couder, and M. E. Brachet, Phys. Rev. Lett. **67**, 983 (1991).

[114] E. Siggia and G. S. Patterson, Journal of Fluid Mechanics **86**, 567 (1978).

[115] J. R. Herring and J. C. McWilliams, Journal of Fluid Mechanics **153**, 229 (1985).

[116] J. Maron and P. Goldreich, The Astrophysical Journal **554**, 1175 (2001).

[117] Z.-S. She, E. Jackson, and S. A. Orszag, Nature **344**, 226 (1990).

[118] J.-P. Laval, P. Blaineau, N. Leprovost, B. Dubrulle, and F. Daviaud, Phys. Rev. Lett. **96**, 204503 (2006).

[119] Y. Ponty, P. D. Mininni, J.-F. Pinton, H. Politano, and A. Pouquet, New J. Phys. **9**, 296 (2007).

[120] A. Limone, D. R. Hatch, C. B. Forest, and F. Jenko, Phys. Rev. E **86**, 066315 (2012).

[121] A. Limone, D. R. Hatch, C. B. Forest, and F. Jenko, Physics of Fluids **25**, 066603 (2013).

[122] S. Pope, *Turbulent Flows* (Cambridge University Press, 2000).

[123] R. Benzi, S. Ciliberto, C. Baudet, G. R. Chavarria, and R. Tripiccione, EPL (Europhysics Letters) **24**, 275 (1993).

[124] D. Segel, V. L'vov, and I. Procaccia, Phys. Rev. Lett. **76**, 1828 (1996).

[125] S. Chakraborty, U. Frisch, and S. S. Ray, Journal of Fluid Mechanics **649**.

[126] G. Stolovitzky and K. R. Sreenivasan, Phys. Rev. E **48**, R33 (1993).

[127] J. K. Bhattacharjee and A. Sain, Physica A: Statistical Mechanics and its Applications **270**, 165 (1999).

[128] A. Sain and J. K. Bhattacharjee, Phys. Rev. E **60**, 571 (1999).

[129] H. Fujisaka and S. Grossmann, Phys. Rev. E **63**, 026305 (2001).

[130] V. Yakhot, Phys. Rev. E **63**, 026307 (2001).

[131] Y.-H. Pao, Phys. Fluids **8**, 1063 (1965).

[132] S. Grossmann, D. Lohse, and A. Reeh, Physical review E: Statistical physics, plasmas, fluids, and related interdisciplinary topics **56**, 5473 (1997).

[133] R. Camussi and G. Guj, Meccanica **30**, 719 (1995), 10.1007/BF00986576.

[134] G. Stolovitzky, K. R. Sreenivasan, and A. Juneja, Phys. Rev. E **48**, 3217 (1993).

[135] A. Babiano, B. Dubrulle, and P. Frick, Phys. Rev. E **55**, 2693 (1997).

[136] T. Williams and C. Kelley, *gnuplot. An Interactive Plotting Program. Version 4 2.*, 2007.

[137] V. Budaev *et al.*, Nuclear Fusion **48**, 024014 (2008).

[138] D. Biskamp and H. Welter, Physics of Fluids B **1**, 1964 (1989).

[139] D. Biskamp, E. Schwarz, and A. Celani, Physical Review Letters **81**, 4855 (1998).

[140] A. Pouquet, U. Frisch, and M. Meneguzzi, Phys. Rev. A **33**, 4266 (1986).

[141] W.-C. Müller and D. Biskamp, Phys. Rev. Lett. **84**, 475 (2000).

[142] C. Meneveau, Phys. Rev. E **54**, 3657 (1996).

[143] B. Dubrulle, Physical Review Letters **73**, 959 (1994).

[144] R. Sánchez, B. P. van Milligen, D. E. Newman, and B. A. Carreras, Phys. Rev. Lett. **90**, 185005 (2003).

[145] V. Carbone, L. Sorriso-Valvo, E. Martines, V. Antoni, and P. Veltri, Phys. Rev. E **62**, R49 (2000).

[146] E. Covas *et al.*, Astronomy and Astrophysics **345**, 669 (1999).

[147] H. Moffatt, North Atlantic Treaty Organization. Scientific Affairs Division, and University of California, Santa Barbara. Institute for Theoretical Physics, *Topological aspects of the dynamics of fluids and plasmas,* NATO Advanced Study Institutes series. Series E, Applied sciences (Kluwer Academic Publishers, 1992).

[148] I. V. Khalzov *et al.*, Physics of Plasmas **19**, 104501 (2012).

[149] F. Ravelet, L. Marié, A. Chiffaudel, and F. Daviaud, Phys. Rev. Lett. **93**, 164501 (2004).

[150] G. Berkooz, P. Holmes, and J. L. Lumley, Annu. Rev. Fluid Mech. **25**, 539 (1993).

[151] S. Futatani, S. Benkadda, and D. del Castillo-Negrete, Physics of Plasmas **16**, 042506 (2009).

[152] D. R. Hatch *et al.*, Phys. Rev. Lett. **108**, 235002 (2012).

[153] P. Beyer, S. Benkadda, and X. Garbet, Phys. Rev. E **61**, 813 (2000).

[154] D. R. Hatch, P. W. Terry, F. Jenko, F. Merz, and W. M. Nevins, Phys. Rev. Lett. **106**, 115003 (2011).

[155] D. C. Lay, *Linear Algebra and its applications*, 4 ed. (Addison-Wesley, 2012).

[156] M. E. Wall, A. Rechtsteiner, and L. M. Rocha, Singular value decomposition and principal component analysis, in *A Practical Approach to Microarray Data Analysis*, edited by D. Berrar, W. Dubitzky, and M. Granzow, Kluwer: Norwell, MA, 2003, arXiv:physics/0208101.

[157] W. Press, *Numerical Recipes 3rd Edition: The Art of Scientific Computing* (Cambridge University Press, 2007).

[158] S. Benkadda *et al.*, Phys. Rev. Lett. **73**, 3403 (1994).

[159] L. S. Blackford *et al.*, Scalapack user's guide, in *ScaLAPACK user's guide*, edited by J. J. Dongarra, Society for Industrial and Applied Mathematics, Philadelphia, PA, USA, 1997.

[160] A. de la Torre and J. Burguete, Phys. Rev. Lett. **99**, 054101 (2007).

[161] E. Crespo Del Arco, J. J. Sànchez-Àlvarez, E. Serre, A. De La Torre, and J. Burguete, Geophysical & Astrophysical Fluid Dynamics **103**, 163 (2009).

[162] F. Ravelet, A. Chiffaudel, F. Daviaud, and J. Léorat, Physics of Fluids **17**, 117104 (2005), arXiv:physics/0411213.

[163] E. J. Kaplan, B. P. Brown, K. Rahbarnia, and C. B. Forest, Phys. Rev. E **85**, 066315 (2012).

[164] F. Pétrélis and S. Fauve, Europhys. Lett. **76**, 602 (2006).

[165] R. Volk, P. Odier, and J.-F. Pinton, Physics of Fluids **18**, 085105 (2006), arXiv:physics/0511204.

[166] A. de la Torre, J. Burguete, and C. Pèrez-Garcìa, The European Physical Journal - Special Topics **146**, 313 (2007), 10.1140/epjst/e2007-00189-4.

[167] E. Buckingham, Phys. Rev. **4**, 345 (1914).

[168] C. Fletcher, *Computational techniques for fluid dynamics: Specific techniques for different flow categories,* Springer series in computational physics (Springer, 1988).

Acknowledgements

I would like to thank my supervisor Prof. Dr. Frank Jenko for giving me the opportunity to work on this project. Thanks to his widespread net of scientific contacts, I could meet experts in various fields, attend numerous conferences, visit foreign institutes, have visibility. However, my thanks to him go beyond our scientific collaboration, as he already knows.

I am grateful to the Institute for Plasma Physics and the Max-Planck-Society, of which I was proud to be part. In particular, I am grateful to Prof. Dr. Sybille Günter and Prof. Dr. Karl Lackner for hosting this PhD project at the tokamak theory department at IPP Garching.

I thank the professional support of: Dr. Klaus Reuter, Dr. David Hatch, Prof. Dr. Cary B. Forest, Dr. Kian Rahbarnia, Dr. Michael Wilczek, Prof. Dr. Andreas Tilgner, Prof. Dr. Hantao Ji, Prof. Dr. Jeremy Goodman, Dr. Christophe Gissinger. Moreover, I profoundly thank the professional *and* human support of: Prof. Dr. J.-L. Guermond, Dr. Francky Luddens, Loïc Cappanera, Dr. Adolfo Ribeiro, Prof. Dr. Caroline Nore, Prof. Dr. Francesco Califano, Dr. Nicolas Plihon.

Further acknowledgements go to those colleagues who made my working environment more enjoyable (in particular, Alejandro Bañón Navarro and Silvio Sergio Cerri). I am grateful to Johannes Weissmann, with whom I had a fruitful (and daily) brainstorming and a friendly interaction during the last part of my PhD project. He probably did not realize how much I learnt by acting as his unofficial second supervisor.

My deepest thanks go to the members of my family.